

T-3957

**ON THE BEHAVIOR OF INFILTRATING ALUMINUM INTO COMPACTS
COMPRISED OF SILICON CARBIDE AND ALUMINUM
POWDER MIXED WITH SILICON CARBIDE**

by

Paul Q. Campbell

ProQuest Number: 10783650

All rights reserved

INFORMATION TO ALL USERS

The quality of this reproduction is dependent upon the quality of the copy submitted.

In the unlikely event that the author did not send a complete manuscript and there are missing pages, these will be noted. Also, if material had to be removed, a note will indicate the deletion.



ProQuest 10783650

Published by ProQuest LLC (2018). Copyright of the Dissertation is held by the Author.

All rights reserved.

This work is protected against unauthorized copying under Title 17, United States Code
Microform Edition © ProQuest LLC.

ProQuest LLC.
789 East Eisenhower Parkway
P.O. Box 1346
Ann Arbor, MI 48106 – 1346

T-3957

A thesis submitted to the Faculty and the Board of Trustees of the Colorado School of Mines in partial fulfillment of the requirements for the degree of Master of Science (Metallurgical Engineering).

Golden, Colorado

Date: 11/13/90

Signed: Paul Q. Campbell
Paul Q. Campbell

Approved: Glen R. Edwards
Glen R. Edwards
Thesis Advisor

Golden, Colorado

Date: 11/13/90

John J. Moore
John J. Moore
Department Head
Department of Metallurgical
and Materials Engineering

ABSTRACT

The emphasis of this work was to characterize some of the variables that affect the kinetics of aluminum infiltration into silicon carbide compacts. To visually observe the infiltration process, a simulation was conducted by infiltrating mercury into glass beads so that the process could be videotaped for analysis. The results of the simulation showed that for long times the square of the infiltration distance varies linearly with the infiltration time. Compacts of silicon carbide prepared by a vibration technique were found to have reproducible permeabilities when compacts of a given type were tested with argon gas. The threshold pressure, the minimum pressure required for infiltration of aluminum into silicon carbide, was found to decrease from 106 kPa at 670°C to 95 kPa at 750°C using results from permeability tests. When measurements from a scanning electron microscope analysis were used, the threshold pressure was found to decline from 94 kPa at 670°C to 84 kPa at 750°C. A previously developed model was used to correlate the temperature dependence of the infiltration rate with the activation energy for the viscous flow of aluminum (found to be 13.9 kJ/mole in this system). A

T-3957

phenomenological equation has been obtained that relates the rate of infiltration to the applied pressure, the threshold pressure, a reference height, the activation energy for viscous flow of aluminum, and the absolute temperature. It has also been determined that addition of aluminum powder to the compact prior to infiltration can alleviate porosity and also provides a method for changing the volume fraction of particulate reinforcement.

TABLE OF CONTENTS

| | <u>Page</u> |
|---|-------------|
| ABSTRACT..... | iii |
| LIST OF FIGURES..... | vii |
| LIST OF TABLES..... | xi |
| ACKNOWLEDGEMENTS..... | xii |
| 1.0 INTRODUCTION..... | 1 |
| 1.1 Overview of Metal Matrix Composites..... | 2 |
| 1.2 Scope of Research..... | 21 |
| 1.3 Objective of the Present Research..... | 33 |
| 2.0 LITERATURE REVIEW..... | 35 |
| 2.1 Physical Properties of Aluminum..... | 35 |
| 2.1.1 Density of Liquid Aluminum..... | 35 |
| 2.1.2 Surface Tension of Liquid Aluminum.. | 38 |
| 2.1.3 Viscosity of Liquid Aluminum..... | 41 |
| 2.2 Silicon Carbide/Aluminum Interface..... | 45 |
| 2.3 Wetting of Silicon Carbide by Liquid Aluminum..... | 49 |
| 2.4 Vibratory Packing of Particulate Beds..... | 52 |
| 2.5 Infiltration..... | 56 |
| 2.5.1 Thermodynamics of Infiltration..... | 56 |
| 2.5.2 Kinetics of Infiltration..... | 61 |

| | |
|---|-----|
| 3.0 EXPERIMENTAL PROCEDURE..... | 71 |
| 3.1 Infiltration Parameters..... | 71 |
| 3.2 Materials..... | 77 |
| 3.3 Sample Preparation..... | 84 |
| 3.4 Reaction Tube Atmosphere..... | 86 |
| 3.5 Infiltration Tests..... | 86 |
| 4.0 RESULTS AND DISCUSSION..... | 92 |
| 4.1 Infiltration Simulation..... | 92 |
| 4.2 Body Characterization..... | 95 |
| 4.3 Infiltration Experiments..... | 109 |
| 4.3.1 Temperature Dependence..... | 111 |
| 4.3.2 Pressure Dependence..... | 119 |
| 4.3.3 Overall Dependence..... | 123 |
| 4.4 Microstructural Examination of Composites.. | 125 |
| 5.0 CONCLUSIONS..... | 131 |
| 6.0 FUTURE RECOMMENDATIONS..... | 133 |
| REFERENCES..... | 134 |

LIST OF FIGURES

| | <u>Page</u> |
|--|-------------|
| 1.1. Influence of loading angle on the properties of an aluminum-boron composite..... | 12 |
| 1.2. Elastic properties of aluminum-silicon carbide composites..... | 15 |
| 1.3. Tensile properties of aluminum-silicon carbide composites..... | 16 |
| 1.4. Influence of temperature on the strength of 6061 aluminum/ 15 volume percent silicon carbide whisker reinforced composite and AA6061-T6 unreinforced alloy..... | 18 |
| 1.5. Influence of particulate silicon carbide on the coefficient of thermal expansion (CTE) of alloy 6061..... | 19 |
| 1.6. Performance map of various high temperature engine materials in terms of operating temperature and strength/weight ratio..... | 22 |
| 1.7. A schematic diagram of the squeeze casting processing cycle..... | 26 |
| 1.8. A schematic diagram of the diffusion bonding process..... | 28 |
| 1.9. Sketch of a pressure chamber used for infiltration..... | 31 |
| 2.1. The recommended values for the thermal linear expansion coefficient for aluminum..... | 36 |
| 2.2. The density of liquid aluminum as a function of temperature..... | 39 |
| 2.3. Surface tension of liquid aluminum as a function of temperature..... | 42 |

| | |
|--|----|
| 2.4. The viscosity of liquid metals and their dependence on temperature..... | 44 |
| 2.5. Schematic diagram of a sessile drop used to measure wettability..... | 50 |
| 2.6. The contact angle for aluminum on silicon carbide as a function of temperature and alloy composition..... | 53 |
| 2.7. The wettability of aluminum on silicon carbide as a function of temperature and composition.... | 54 |
| 2.8. The possible stages of infiltration of a porous plate..... | 58 |
| 2.9. Schematic diagram showing the forces acting within a capillary..... | 62 |
| 2.10. Schematic diagram describing the infiltration of a powder compact..... | 65 |
| 3.1. SEM photomicrographs of 177 μm silicon carbide particles..... | 78 |
| 3.2. SEM photomicrographs of 106 μm silicon carbide particles..... | 79 |
| 3.3. SEM photomicrographs of aluminum powder used in tests..... | 80 |
| 3.4. Schematic diagram of the infiltration fixture... | 85 |
| 3.5. Schematic diagram of the re-circulation circuit for cleaning the reaction chamber atmosphere..... | 87 |
| 3.6. Schematic diagram of the infiltration apparatus. | 88 |
| 3.7. Schematic diagram of the changes in flow rate during infiltration..... | 90 |
| 4.1. Photographs of the various stages of the infiltration of mercury into glass beads..... | 93 |

| | |
|--|-----|
| 4.2. Infiltration distance squared as a function of time for the infiltration of mercury into glass beads..... | 94 |
| 4.3. Pressure drops across the filters used for the infiltration of aluminum into silicon carbide at known flow rates..... | 96 |
| 4.4. Pressure drops across silicon carbide compacts at known flow rates..... | 98 |
| 4.5. Photograph showing the typical channeling pattern of aluminum going down sides instead of uniformly through compact..... | 103 |
| 4.6. Photograph of sample showing successful infiltration of a compact (diameter of 12.7 millimeters or 0.5 inches) when the length of the cylindrical compact is about the same as the diameter..... | 105 |
| 4.7. Photograph of larger compacts (diameter of 22.2 millimeters or 0.875 inch) illustrating that infiltration becomes uniform at approximately the point where the length left to infiltrate is about the same as the diameter..... | 106 |
| 4.8. Successful infiltration after silicon carbide compact has been packed using vibration method.. | 108 |
| 4.9. The temperature dependence of infiltrating aluminum into 106 μm silicon carbide compacts... | 114 |
| 4.10. The temperature dependence of infiltrating aluminum into 177 μm silicon carbide compacts.. | 115 |
| 4.11. Comparison between the temperature dependencies of infiltrating aluminum into 106 and 177 μm silicon carbide compacts..... | 116 |

| | | |
|-------|---|-----|
| 4.12. | A comparison of the temperature dependencies of infiltrating aluminum into 106 μm silicon carbide compacts and 106 μm silicon carbide mixed with aluminum powder..... | 118 |
| 4.13. | A comparison of the pressure dependencies between the infiltration of aluminum into 106 and 177 μm silicon carbide compacts..... | 121 |
| 4.14. | A comparison of the pressure dependencies between the infiltration of aluminum into a 106 μm silicon carbide compact and a bed consisting of 106 μm silicon carbide mixed with aluminum powder..... | 124 |
| 4.15. | SEM photomicrograph showing 106 μm silicon carbide dispersed in an aluminum matrix..... | 126 |
| 4.16. | SEM photomicrograph showing 177 μm silicon carbide dispersed in an aluminum matrix..... | 128 |
| 4.17. | SEM photomicrograph showing 106 μm silicon carbide dispersed in an aluminum matrix..... | 129 |
| 4.18. | SEM photomicrograph showing 106 μm silicon carbide dispersed in an aluminum matrix..... | 130 |

LIST OF TABLES

| | <u>Page</u> |
|--|-------------|
| 1.1. Typical Properties of Continuous Fibers..... | 5 |
| 1.2. Typical Properties of Whiskers..... | 7 |
| 1.3. Mechanical Properties of Silicon Carbide/Aluminum Composites..... | 14 |
| 2.1 Mechanical Properties of Pure Aluminum at Room Temperature..... | 37 |
| 3.1 Characterization of 177 μm Silicon Carbide..... | 81 |
| 3.2 Characterization of 106 μm Silicon Carbide..... | 82 |
| 3.3 Characterization of Aluminum Powder..... | 83 |
| 4.1 Slopes and correlation coefficients of Figure 4.4..... | 99 |
| 4.2 Threshold Pressures for Infiltrating Aluminum through 106 μm Silicon Carbide at Various Temperatures..... | 102 |
| 4.3 Slopes and Intercepts of the Lines Showing the Pressure Dependencies of Infiltrating Aluminum into 106 and 177 μm Silicon Carbide Compacts..... | 122 |

ACKNOWLEDGEMENTS

This research was supported by the Strategic Defense Initiative Office/Innovative Science Technology, contract number N00014-88-K-0500. The encouragement and support of Dr. Steven Fishman is gratefully acknowledged. A special thanks goes to Dr. G.R. Edwards, Dr. G.P. Martins, and Dr. D.L. Olson for their help in overseeing the project. The author would also like to thank Herb Bird, Bob McGrew, Dr. Bruce Lanning, Carlos Silva, and P. Chidambaram for their suggestions and assistance with the project. The author is also grateful to Monique Joyce for her emotional support.

1.0 INTRODUCTION

Composite materials can be broadly defined as a combination of two or more materials each of which has its own distinctive properties. The stimulus for using composites is derived from the possibility of procuring property combinations that can result in a number of service benefits. Some of these advantages include increased strength, decreased weight, higher service temperature, improved wear resistance, higher elastic modulus, improved fatigue properties, and better dimensional stability.

Metal matrix composites have been undergoing developments for over 20 years. Initially, most of the effort in this area was concentrated on continuous fiber metal matrix composites. These materials were first used in aerospace applications, but their usefulness in other areas is expanding. One reason for this expansion is the lowering of the cost of metal matrix composites, which has partially been brought about by the development of discontinuously reinforced metal matrix composites (1, 2).

Discontinuously reinforced metal matrix composites represent a group of materials that combine the strength and hardness of the reinforcing phase with the ductility and

toughness of the metal matrix. This study involves the fabrication of aluminum/silicon carbide composites, and the interest in these particular materials is associated with: their high elastic modulus, high strength, and light weight; the ability to economically produce silicon carbide whiskers, platelets and particulates; the ability to use standard shaping methods such as forging, rolling, and extrusion; and much less dependence of the engineering properties on directions than with continuous composites (3).

It has been implied that one of the main reasons for employing discontinuously reinforced metal matrix composites is their lower cost, as compared with fiber-reinforced composites. One of the most economical means of fabricating these materials is by infiltrating molten metal into a preform of the reinforcing material and then allowing the metal to solidify, forming a composite. This work aims to study some of the aspects of infiltrating molten aluminum into silicon carbide.

1.1 Overview of Metal Matrix Composites

Metal matrix composites are comprised of a metal as a base material (matrix) and a reinforcement, such as a ceramic, to modify the properties of the metal. There are

three general types of metal matrix composites: 1) dispersion-strengthened, 2) particle-reinforced, and 3) fiber-reinforced.

Dispersion-strengthened metal matrix composites consist of particles with diameters less than 0.1 micrometer, and the volume fraction of particles varies from 1 to 15 percent. It can be shown that a fine dispersion of particles of this size can effectively block dislocation movement, strengthening the metal matrix. In this case, the strengthened matrix becomes the major load-bearing constituent.

Particle-reinforced metal matrix composites comprise of particles with diameters greater than 1.0 micrometer, and the volume fraction of particles ranges from 5 to 40 percent. In this case, the load is shared by the matrix and particles.

Fiber-reinforced metal matrix composites can be divided into two major classes: 1) composites in which the fibers of the strengthener are continuous and 2) composites in which the fibers of the strengthener are discontinuous (whiskers) and may be of lengths from 0.1 to 250 micrometers. The distinguishing feature between fibers and the other types of reinforcements is that the fibers have one long dimension, whereas the reinforcing particles of the

other two types do not. In this case, the fiber is the major load-bearing component.

Continuous fiber-reinforced materials are anisotropic, that is, they are stronger in the direction parallel to the fiber (longitudinal direction) than in the direction perpendicular to the fiber (transverse direction). The fibers can be woven into cross-ply orientations to increase transverse properties. The primary function of the fibers is to carry the load, whereas the matrix transfers and distributes the load to the fibers. The effectiveness of the transfer of the load from the matrix to the fibers relies on the bonding interface between them. If the bonding interface is efficient, then the mechanical properties of the composite are more contingent on the properties of the fiber rather than those of the matrix. The significance of this is that the matrix can be selected on the basis of other required properties, such as density, oxidation resistance, and corrosion resistance. Some typical properties of common continuous fibers are given in Table 1.1.

Metal matrix composites that are reinforced by discontinuous fibers, or whiskers, have another set of critical factors. These items include the length-to-diameter ratio of the fiber, the shear strength of the bond

Table 1.1
Typical Properties of Continuous Fibers

| Fiber type | Diameter μm | Density g/cm^3 | Specific Modulus | Specific Strength |
|-----------------------------------|---------------------------|----------------------------|---------------------|----------------------|
| B(SiC) fil. | 240 | 2.4 | 162 | 1660 |
| SiC(C) fil. | 140 | 2.0 | 140 | 1330 |
| Nicalon tow | 15 | 2.6 | 71 | 1040 |
| $\alpha\text{Al}_2\text{O}_3$ tow | 20 | 3.9 | 97 | >360 |
| C, HM tow | 8.4 | 1.96 | 265 | 950 |
| C, HT tow | 7.0 | 1.75 | 130 | 2030 |

Note: Continuous fibers are either in the form of monofilaments, or monofilament yarns or tows. B(SiC), which is a boron filament on a tungsten core with an outer coating of SiC, was one of the first fibers to be produced for metal matrix composites, and was produced by Avco corporation as BORSIC. While this fiber is still available, Avco have now developed a monofilament SiC(C) with a higher carbon content on the outside, which is more stable in contact with molten metal. Continuous fibers are available as individual reels of monofilament and tows, or as weaves.

Source: Lloyd, D.J., "Metal Matrix Composites - An Overview", Proceedings of the International Symposium on Advanced Structural Materials, Pergamon Press, New York, August 28-31, pp.1-21 (1988).

between the fiber and the matrix, and the amount of fiber. All of these variables affect the strength of the composite. One advantage of these whiskers is that they can often be more economical to manufacture than continuous fibers. Also, discontinuous fiber-reinforced composites can be formed into various shapes using standard metallurgical processes. Some typical properties of common whiskers are shown in Table 1.2.

The application for a material is an important factor in determining the matrix to be used, but in many cases property gains are obtained by low density alloys of aluminum, magnesium, and titanium because most reinforcements (with the exception of carbon fibers) have densities above 3 g/cm^3 and a large weight penalty results if they are incorporated into the higher density metals. The majority of work on composites up to the present has included aluminum and titanium, but there is an increased involvement in reinforced magnesium and aluminides.

When choosing the reinforcement, there are three general considerations: 1) the application, which dictates the reinforcement form and cost level, 2) the compatibility between the reinforcement and matrix, and 3) the interfacial strength between the fiber and matrix.

Table 1.2

Typical Properties of Whiskers

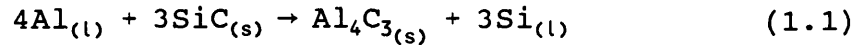
| Whisker Type | Diameter μm | Density g/cm^3 | Specific Modulus | Specific Strength |
|--------------------------------|---------------------------|----------------------------|---------------------|----------------------|
| SiC (Silar) | 0.6 | 3.2 | 220 | 2200 |
| SiC (Tokamax) | 0.1-0.5 | 3.19 | 170 | 4000 |
| Si ₃ N ₄ | 0.5-2.0 | 3.18 | 120 | 4000 |

Source: Lloyd, D.J., "Metal Matrix Composites - An Overview", Proceedings of the International Symposium on Advanced Structural Materials, Pergamon Press, New York, August 28-31, pp. 1-21 (1988).

Applications which require the highest strengths will employ continuous fibers or whiskers, and this will entail substantial costs. Any part that has to be shaped by the standard shaping methods mentioned earlier will most likely use particulates or whiskers since they receive less damage during this type of processing. When economics requires the cheapest forms, particulates are the most likely candidates.

The most difficult condition to accomplish is compatibility between the reinforcement and the matrix. In the beginning stages of composite fabrication, compatibility of the composite is required so that the matrix can wet and spread easily over the surface of the reinforcement, resulting in more of a void-free composite. Generally, ceramics are not easily wetted by metals (see section 2.3 on wetting). Reinforcements are often surface treated to achieve wetting before being incorporated into the matrix. Another aspect of compatibility is a reaction occurring with the matrix and reinforcement. Such reactions can lead to the degradation of the reinforcement, and protective coatings are sometimes put on the reinforcement to prevent this deterioration. Aluminum matrices react with many reinforcements, making it difficult to achieve good compatibility. It is also arduous to achieve good wetting with aluminum matrices. Silicon carbide is fairly stable

below the melting point of aluminum, but reacts with most aluminum alloys above the liquidus. The reaction is:



The products of the reaction are aluminum carbide, which degrades the reinforcement, and silicon, which changes the composition of the matrix (4).

The third important consideration is the attainment of high interfacial strength, since the strength of the composite is acquired by transferring loads from the matrix to the fiber via the interface. Maximum loading of the fiber, according to shear lag theory, is procured by making the fiber longer than a critical length, l_c , which is dependent on the interfacial strength, γ :

$$l_c = \frac{\sigma_f d}{2 \tau} \quad (1.2)$$

where σ_f is the fiber strength, τ is the shear stress, and "d" is the fiber diameter. For particle reinforcement, the critical length is twice that given by equation (1.2). Even though continuous fibers will be long enough, a high interfacial strength is still essential to yield good transverse properties (4).

As was mentioned above, composites offer a combination of properties that make them very useful. Some of the

advantages that metal matrix composites offer are:

- High strength
- High elastic modulus
- High toughness and impact properties
- Low sensitivity to temperature changes or thermal shock
- High surface durability and low sensitivity to surface flaws
- High electrical and thermal conductivity
- High vacuum environment resistance

Another benefit of metal matrix composites is that they can be tailored to give various combinations of these properties, and this flexibility is useful for special applications.

Continuously reinforced composites are presumed to follow the Rule of Mixtures for both strength and modulus:

$$E_c = E_f V_f + E_m V_m \quad (1.3)$$

and

$$E_c = \sigma_f V_f + \sigma_m V_m \quad (1.4)$$

where E is the modulus, σ is the strength, and V is the volume fraction, and the subscripts "c", "f", and "m" refer to the composite, fiber, and matrix respectively. The properties generally increase with the volume fraction of

reinforcement as indicated by the Rule of Mixtures, but even in continuously reinforced composites they fall below the theoretically expected values because of misalignment of the fibers and inhomogeneity in the fiber distribution. The influence of loading a composite at an angle to the fiber direction on the strength and Young's modulus of the composite are shown for aluminum-boron continuously reinforced composites in Figure 1.1. The effect is that the properties fall off significantly with loading direction, and loading at an angle of 90 degrees to the fiber axis produces little comparative strengthening if any at all. This directionality is exhibited in the character of the fracture. The fracture surface of a fiber composite which has been loaded perpendicular to the fibers often displays fiber fracture and fiber pull-out. When the same composite is loaded perpendicular to the fibers, the fracture surface discloses almost complete interfacial failure, leaving the fibers intact. The significance of these observations is that the composites should be loaded parallel to the fiber direction, and if necessary, different fiber ply orientations should be employed in cases of multi-directional loading.

The strengthening mechanisms in whisker and particulate

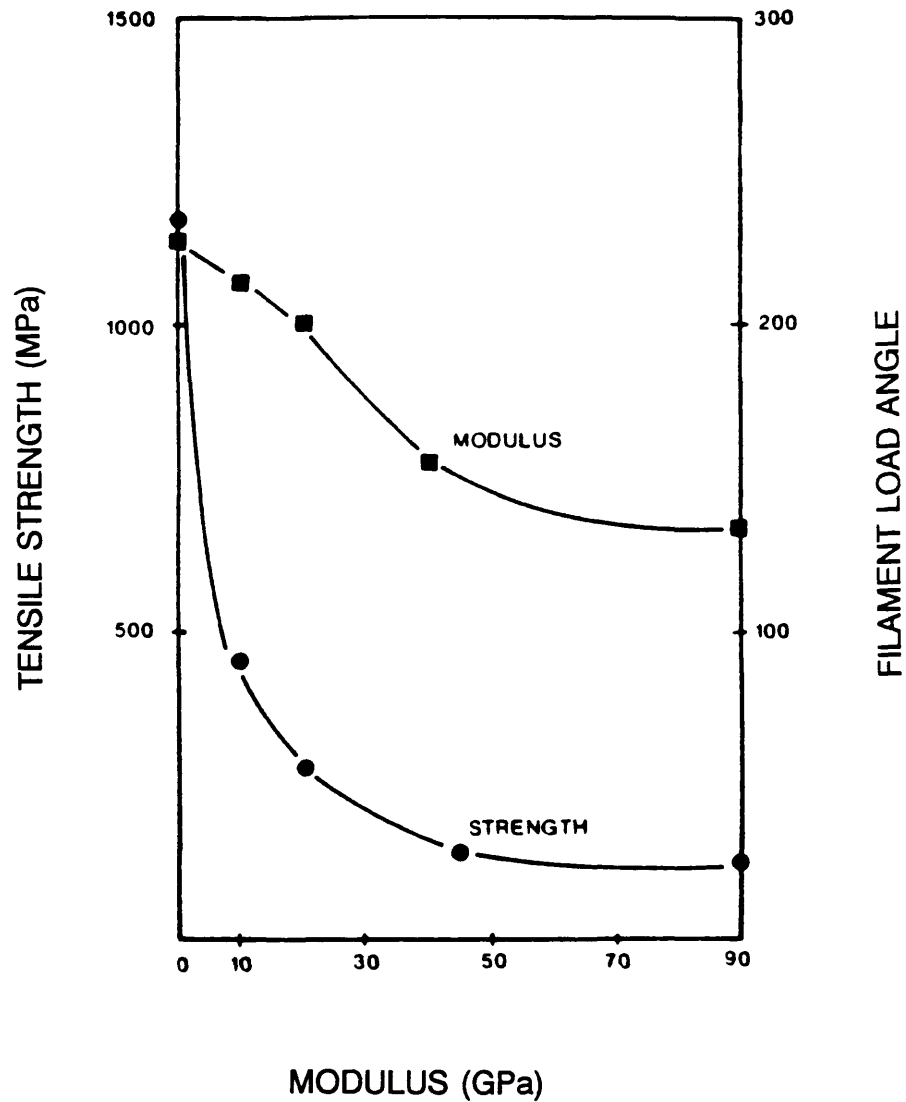


Figure 1.1: Influence of loading angle on the mechanical properties of an aluminum-boron composite (4).

composites are not yet fully comprehended, and these materials frequently exhibit higher strengths than anticipated when applying the Rule of Mixtures to the aspect ratios involved. The higher strengths have been ascribed to edge loading effects (6), enhanced dislocation densities, and internal misfit strain effects resulting from the different moduli of the matrix and the particles and differences in coefficients of expansion between the reinforcement and matrix (7). Whisker reinforced composites exhibit strengths in between those of particulate- and continuous fiber-reinforced composites. Table 1.3 compares some of the properties of some silicon carbide/aluminum composites.

To show the general mechanical property trends with different reinforcements, an aluminum alloy 6061, in the T6 temper condition, reinforced with various forms of silicon carbide is analyzed. Figure 1.2 illustrates the effect of different reinforcements on the tensile modulus, and Figure 1.3 portrays the influence on the tensile strength. These figures support the statement made earlier that fiber-reinforced materials are stronger than whisker-reinforced composites, which in turn are stronger than particulate-reinforced materials. All of the composites, above 10 volume percent of reinforcement, have a higher modulus than

Table 1.3
Mechanical Properties of Silicon Carbide/Aluminum
Composites

| Composite and Heat Treatment | Volume Fraction of SiC, % | Ultimate | | |
|--|---------------------------------|----------------------------|---------------------------|----------------------------|
| | | Tensile Strength MPa | Elastic Modulus GPa | Percent Elongation % |
| SiC _P /6061 T ₆ | 20 | 434-428 | 108 | 1.5 |
| SiC _W /6061 T ₆ | 20 | 607-423 | 106-103 | 3-2.2 |
| SiC _P /2024 T ₆ | 30 | 456 | 118 | |
| SiC _W /2024 T ₄ | 20 | 524-455 | 117-97 | 1-2 |
| SiC _P /7075 T ₆ | 30 | 439 | 119 | |
| SiC _W /7075 T ₆ | 20 | 549 | 101 | |

Source: Arsenault, R.J. and Taya, M., "Thermal Residual Stress in Metal Matrix Composite", Acta Metallurgica; 35 (3), pp.651-659 (1987).

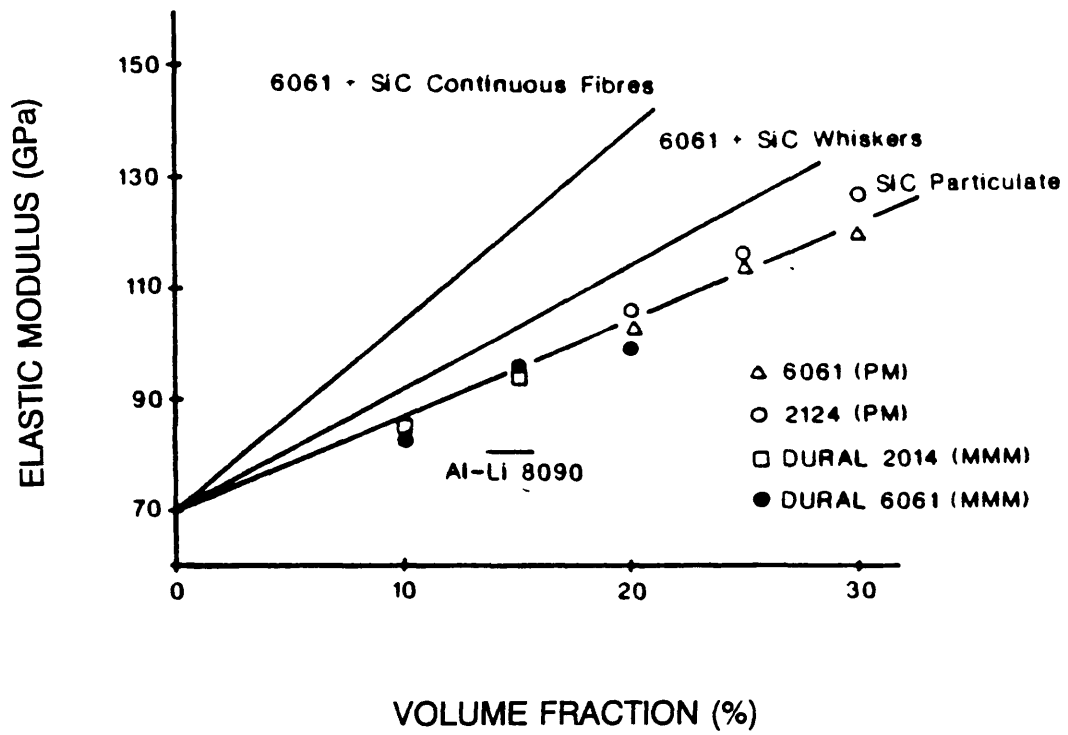


Figure 1.2: Elastic properties of aluminum-silicon carbide composites (4). The PM in the figure denotes powder metallurgy processing and the MMM signifies molten metal mixing.

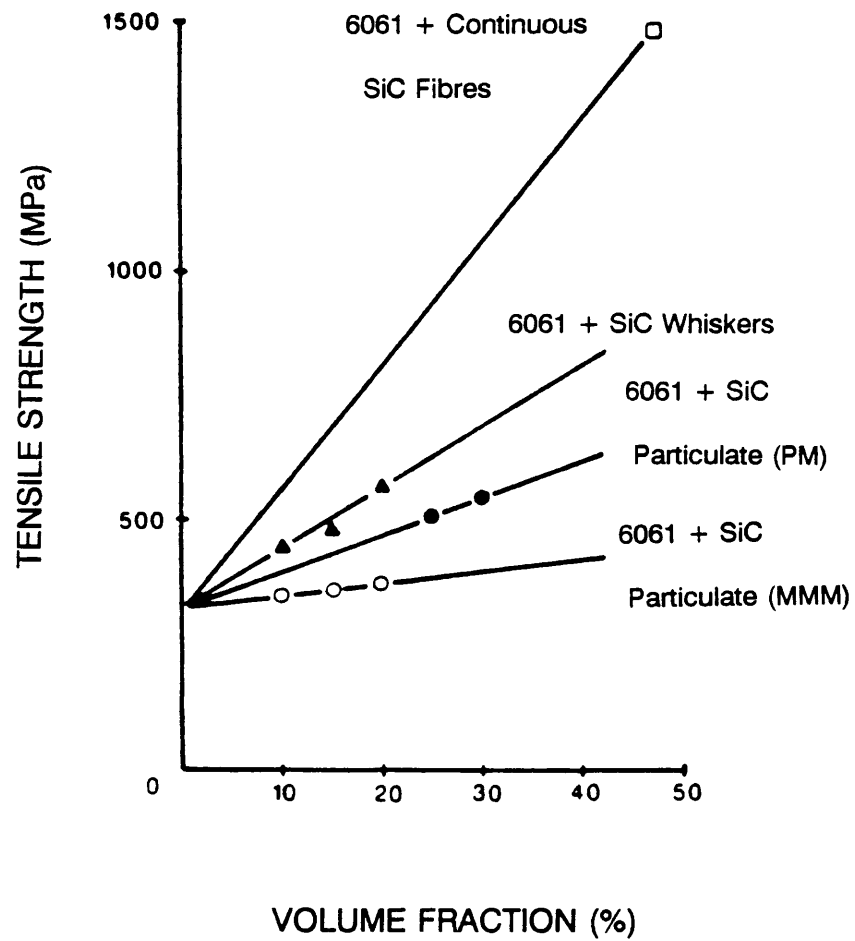


Figure 1.3: Tensile properties of aluminum-silicon carbide composites(4). The PM in the figure denotes powder metallurgy processing and the MMM signifies molten metal mixing.

the highest modulus of commercially available unreinforced aluminum alloys, which are the aluminum-lithium based alloys. The microstructures and to some extent the particle sizes are different in these materials. For particle sizes ranging from 10 to 20 micrometers, the tensile modulus is relatively insensitive to particulate scale, distribution, and microstructure as shown in Figure 1.2. The powder metallurgy process has a more uniform particle distribution, but there are some particle size and microstructural variations, and these effects influence strength as portrayed in Figure 1.3.

Figure 1.4 shows the effect of temperature on aluminum alloy 6061, with a T6 temper, and containing 15 volume percent silicon carbide whiskers. The strength in the composite is retained fairly well relative to the base alloy. The decrease in the composite strength is due to a decrease in the matrix strength because the strength of the silicon carbide does not decrease significantly with temperature. Also, silicon carbide can reduce the coefficient of thermal expansion of aluminum alloy 6061 as depicted in Figure 1.5. The lower the coefficient of thermal expansion of the reinforcement, the greater will be the resulting reduction. Carbon fibers, which have a negative coefficient of thermal expansion, can be employed

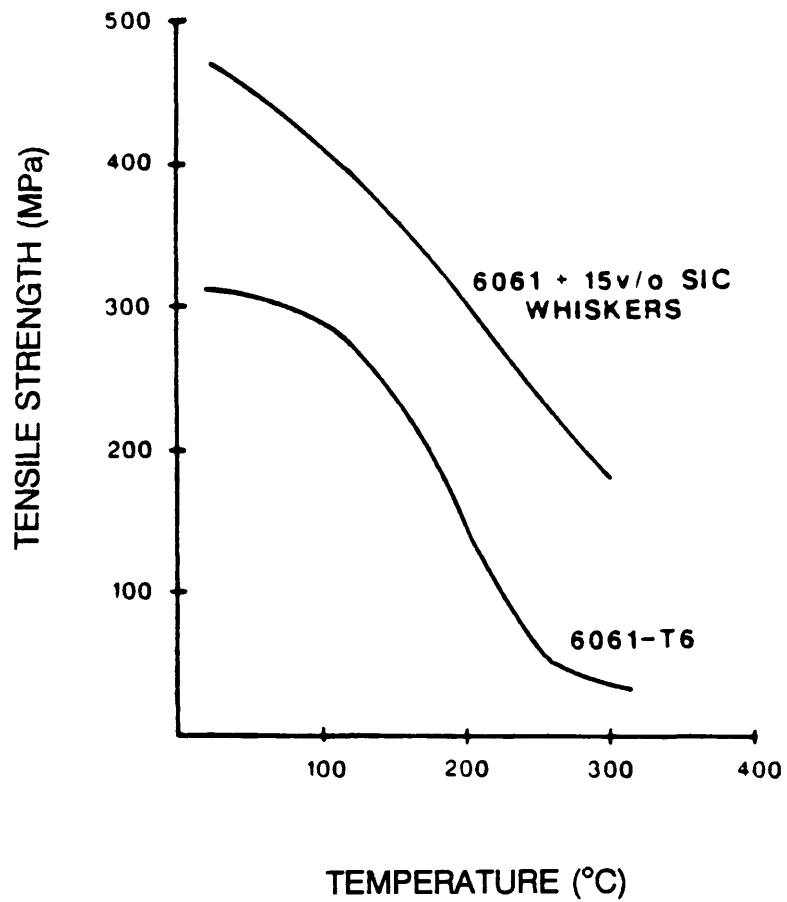


Figure 1.4: Influence of temperature on the strength of 6061 aluminum/15 volume percent silicon carbide whisker reinforced composite and AA6061-T6 unreinforced alloy (4).

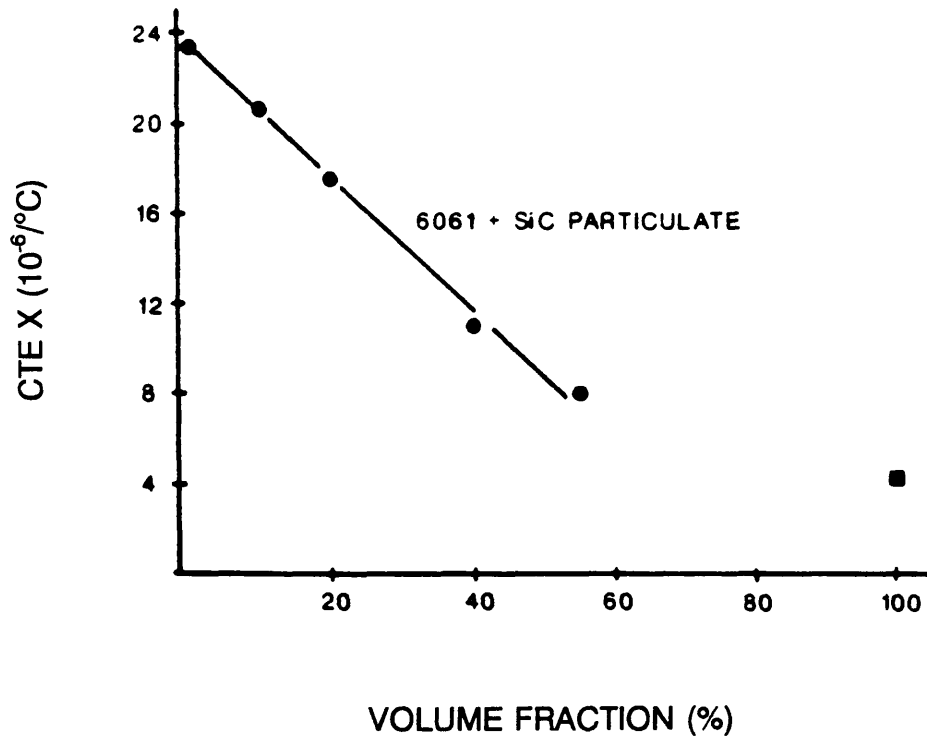


Figure 1.5: Influence of particulate silicon carbide on the coefficient of thermal expansion (CTE) of alloy 6061 (4).

to obtain nearly a zero thermal expansion coefficient in aluminum alloys (1, 4, 5).

The major area of activity for metal matrix composites has been for aerospace applications. One example of their use is the boron-aluminum structural members utilized in the U.S. Space Shuttle Orbiter vehicles. Extensive flight-service evaluations have been done on aluminum composite materials. Also, gas turbine engine airfoils made of these materials have been appraised in ground and flight-service tests. Even though metal matrix composites have been successful in a number of applications, their success has been measured by some failures. One example is the failure of these composites in their proposed use as fan blade materials. The severe impact strength requirements for fan blades have not been satisfied by metal matrix composites.

Even though metal matrix composite materials have been able to meet many structural requirements, their use has been limited due to the fact that the projected cost for components made of these materials is higher than that for alternate materials and designs. Polymer matrix composites are gaining in recognition because they have a lower or similar cost compared to the conventional components that they have replaced. Metal matrix composites have shown superior properties, but are more costly and less well

proven. While metal matrix composites suffer from competition from other composites at lower temperatures, their use in higher temperature applications is another story. Metal matrix composites compete more effectively with polymer matrix composites at a temperature range of 150 to 300°C, and they are prime candidates for the temperature range of 300 to 700°C. Above 700°C, pyroceramic, intermetallic, and ceramic composites will be other choices in the future (8). A comparative overview of the performance of metal matrix composites respect to other materials can be seen in Figure 1.6 (9).

1.2 Scope of Research

There are many ways to fabricate composites. In this section some of the manufacturing techniques will be reviewed briefly. After the summary of the other production methods, a discussion on infiltration, the process under study in this work, will ensue.

The methods employed to make composites differ in detail. They vary from using standard metallurgical processes, such as powder metallurgy and casting, to newer metallurgical techniques, like diffusion bonding and plasma spraying, and finally, to the specially adapted methods of hot roll bonding and liquid metal infiltration. The

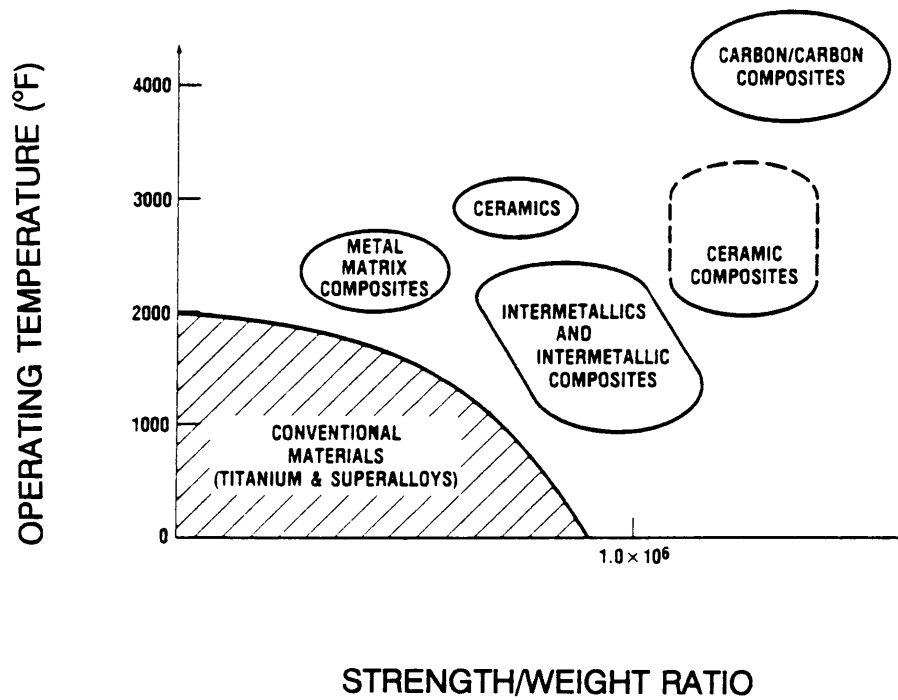


Figure 1.6: Performance map of various high temperature engine materials in terms of operating temperature and strength/weight ratio (5).

majority of emphasis has been put on diffusion bonding, and more recently, spray bonding as the favored technique.

As the market for composites grows, more emphasis will be put on developing continuous processes and more economical processes. Substantial progress has to be made in establishing more economical production methods before composites will become competitive with the other materials that they might replace.

There are some general objectives that each process must meet. These requirements are (10):

- Incorporate the reinforcement without breakage.
- Consolidate the composite with minimal degradation of the reinforcement.
- Establish and maintain filament alignment, or in the case of particles, a uniform dispersion.
- Offer a variety in amount of reinforcement allowed.
- Establish a fiber/matrix interfacial bond that is sufficient enough to transfer the load from the matrix to the fiber.
- Allow for an assortment of matrix selection and alloying.
- Give flexibility for reinforcement spacing.
- Supply the capability for cross and angle ply lay-ups.

- Offer consistency in the end product.
- Achieve a high density matrix with no voids.

A more detailed description on the importance of compatibility between matrix and reinforcement is given in reference (11).

Composites manufactured by powder metallurgy techniques have been made by cold pressing and sintering, or by hot pressing. Aluminum strengthened by boron reinforcements is an example of this group of composites. The dual process of cold pressing followed by sintering is more difficult in that the high pressure needed to consolidate the metal powders to the required density can break the reinforcement or result in degradation of the filament during sintering. Some composites have been made by hot pressing pure aluminum powder and boron fiber mats. In this case the aluminum powder is vibrated into stacked boron mats, and after induction heating, the pressure is applied gradually until the final temperature is reached. Stresses that are caused by deformation during this process can be relieved by annealing (12). For details on the resistance sintering of aluminum/silicon carbide compacts, the reader is referred to reference (14).

There are a variety of ways to cast metal matrix composites. Some of the more representative methods will be

discussed here.

Squeeze casting is the process which refers to the solidification of liquid metal under pressure. The general idea is to "forge" a liquid metal into a closed die. The liquid metal then solidifies rapidly under high pressure (70 to 100 MPa). A schematic diagram of the process is given in Figure 1.7. In this process the casting quality is augmented by the collapse of gas and shrinkage porosity under the influence of the high hydrostatic pressure (14, 15, 16).

Another casting process used is slurry casting, where the reinforcements (e.g. fibers or loose particles) are put into an agitated melt to form a semi-solid slurry. When chopped particles or filaments are added to a two-phase melt (liquid and solid), the process is termed compocasting (15). In compocasting the reinforcements, which are not necessarily wetted by molten metal, can be dispersed in the semi-solid slurry by the stirring action. The main benefit of the process is that the resulting composites can be formed into some shape either by casting processes in the semi-solid state or by some of the techniques used for materials in the solid state. An example of this sequence is the production of the composites of aluminum-7 weight percent silicon alloys reinforced by Nicalon silicon carbide

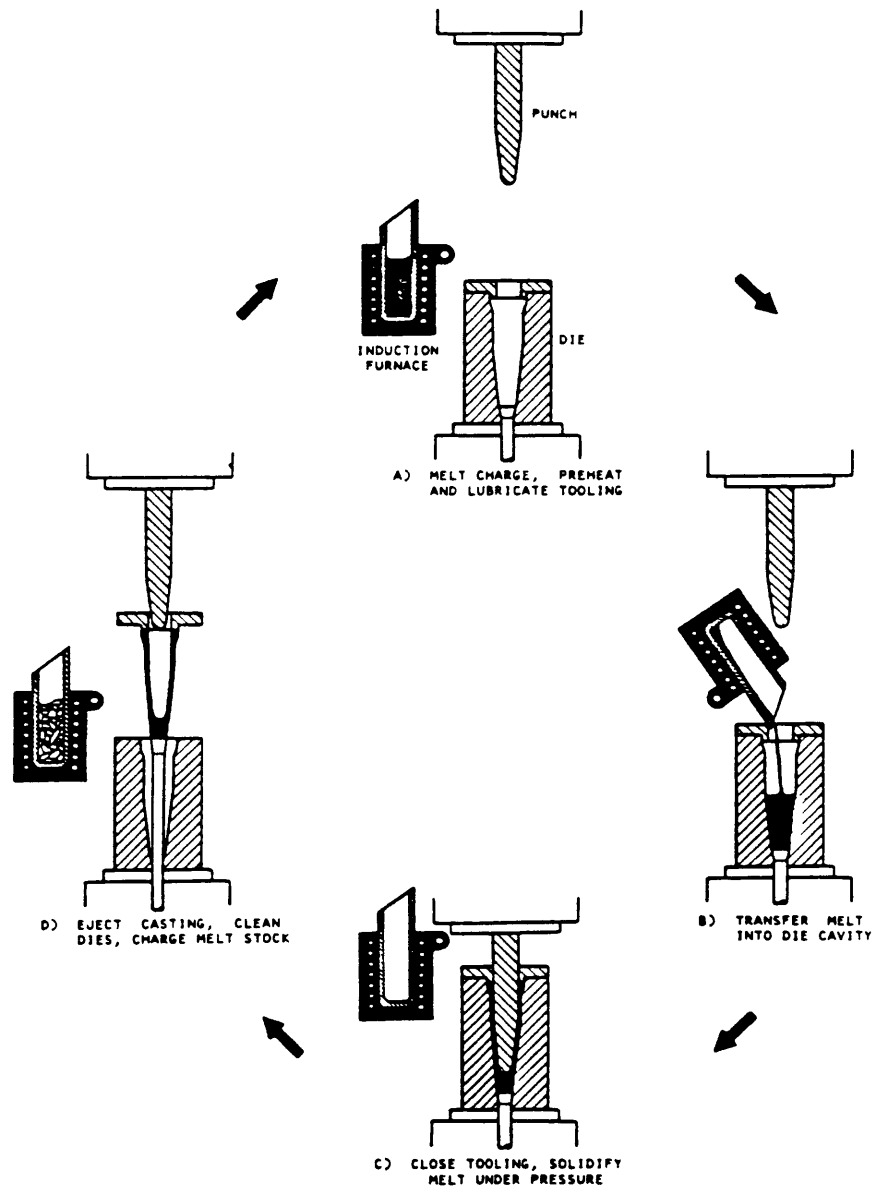


Figure 1.7: A schematic of the squeeze casting processing cycle (14).

filaments. In this case these materials are prepared by compocasting, followed by squeeze casting. This method results in a macroscopically homogeneous material, with some segregation of fibers in the eutectic phase (17).

In systems where the molten metal wets the fibers, the conventional methods of gravity or vacuum casting have been used (15).

The most common way of making metal matrix composites with fibers of diameters of 100 micrometers or larger is the diffusion bonding process. Figure 1.8 shows a schematic diagram of the process. In this technique a monolayer tape, comprised of an array of fibers, is readied by winding the fibers on a drum with controlled spacing. A co-deposited polymer holds the fiber in place. After the mat of filaments is taken off the drum, it is vacuum hot-pressed between the layers of matrix alloy to form a composite monotape. Alternately, the matrix alloy can be plasma sprayed onto the filament wound on the binder. The composite monotape is then cut into suitable laminate shapes and angles, stacked in an appropriate arrangement in a die, and diffusion bonded to form the net shape.

In foil filament array diffusion bonding, unconsolidated fiber array plies and matrix alloy foil or plasma sprayed matrix/fiber laminates are cut and stacked in

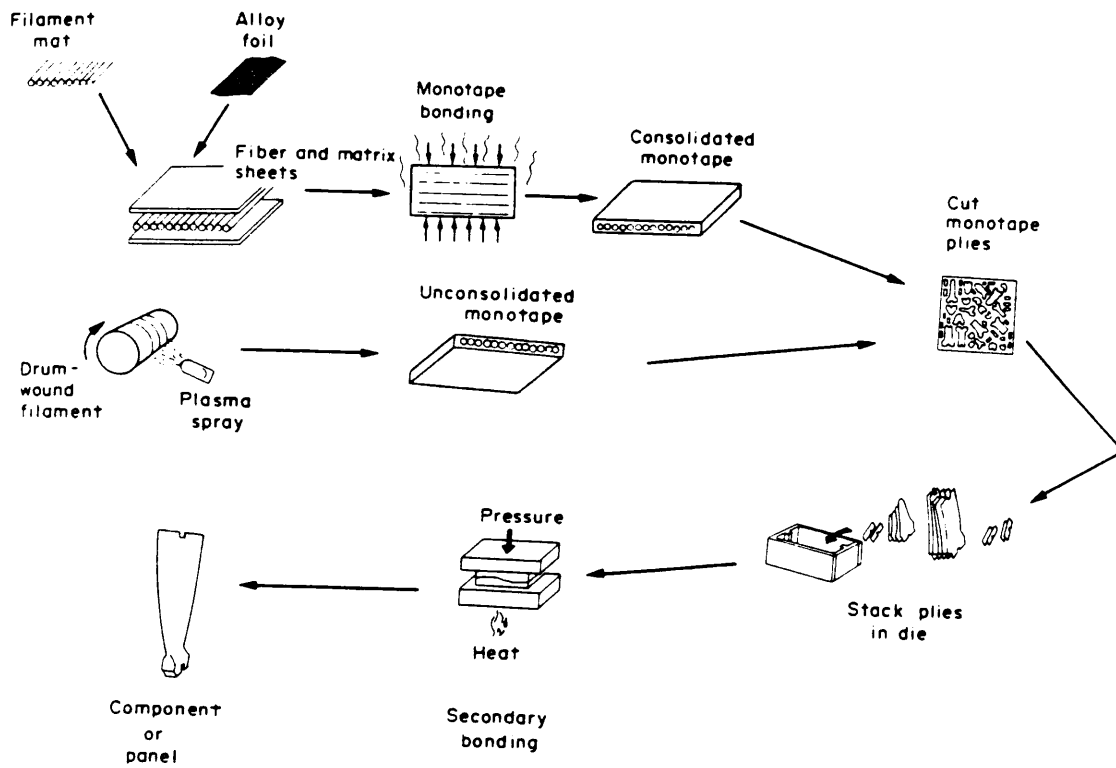


Figure 1.8: A schematic diagram of the diffusion bonding process (8).

a die where they are hot-pressed in one single step. Diffusion bonding is good for making composites to conform to specific properties, but it is energy intensive and limited to relatively small sizes (8, 10).

The plasma spraying process involves the spraying of the matrix metal onto the reinforcement. Electroplating and chemical vapor deposition are also used, but these two processes are limited in terms of matrix composition and rate of deposition. In plasma spraying, matrix foil or plasma sprayed matrix material is wrapped around a cylindrical mandrel with an aligned layer of reinforcing fibers of controlled spacing. The mandrel is then rotated in front of a plasma arc which deposits tiny droplets of matrix material that solidify rapidly upon impact with the mandrel material (10, 18).

Properties of composites can vary with the fabrication process used. A comparison of the resulting aluminum matrix composites produced by diffusion bonding, casting, and plasma spraying is given in reference (18).

The hot roll bonding process involves the simultaneous application of heat and pressure for a reaction time shorter than that of diffusion bonding. The shorter reaction time is useful in composites where there is a compatibility problem between fiber and matrix (e.g. boron/titanium). The

process is practically limited to tapes of up to a few layers thick, which can be diffusion bonded later on (10).

Since it is one of the most economical production methods for composites, liquid metal infiltration has been used to consolidate metal matrix composites wherever it has been possible to do so. The technique is limited because of the relatively few amount of reinforcements that are stable in molten metal, and proper wetting of the metals on the reinforcement is also a problem. The wetting is controlled by various coatings, matrix alloying, and control of the infiltration atmosphere.

The process of infiltration involves the driving of liquid metal into the spaces left by the reinforcements. This can be done with the application of pressure by a gas or ram or under a vacuum. An example of one infiltration apparatus is given in Figure 1.9. When forcing the liquid metal into the spaces surrounding the reinforcement, an important factor is the pressure differential resulting from capillary forces at the liquid metal front during infiltration of the reinforcement. It is the pressure differential that determines whether or not the infiltration will be spontaneous (wetting systems) or will require an applied pressure (non-wetting systems). There are many models for the required pressure differential in the

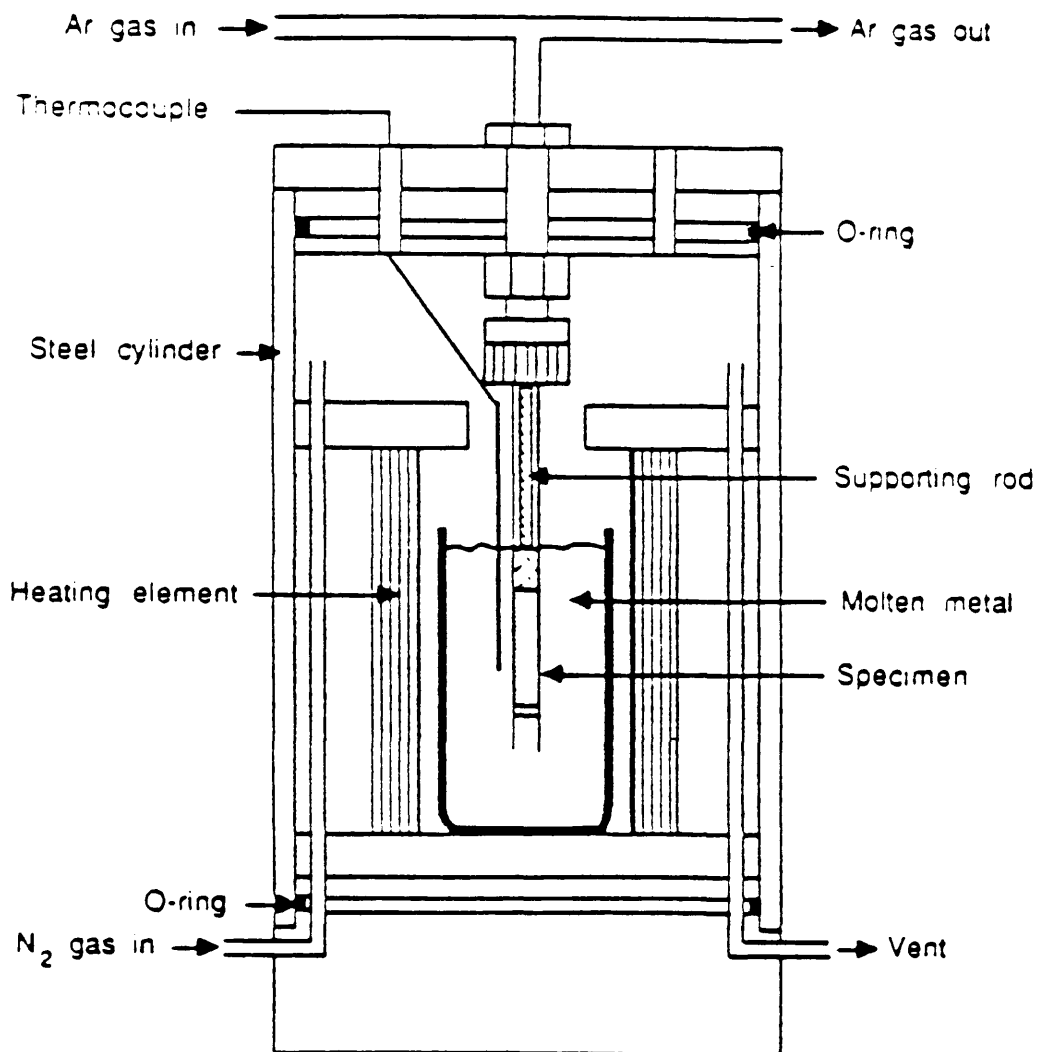


Figure 1.9: Sketch of a pressure chamber used for infiltration (20).

literature, but the most common base is the Young-Kelvin equation:

$$P = \gamma_{LA}\kappa\cos\theta \quad (1.5)$$

where P is the pressure, γ_{LA} is the liquid metal/atmosphere interfacial surface energy, κ is the curvature of the interface, and θ is the wetting contact angle (19, 20). The model for the system in this work is given in the section on kinetics of infiltration.

There have been some interesting developments in infiltration. Aghajanian et al. (21, 22) have been able to spontaneously infiltrate an aluminum-magnesium alloy into a porous bed of ceramic reinforcements, which is permeated by nitrogen gas. The process is suitable for reinforcements such as oxides (alumina), carbides (silicon carbide) borides, and nitrides (aluminum nitride). The nitrogen gas phase is used during the entire infiltration stage to prevent melt oxidation and loss of surface wetting.

Yang et al. (23) have developed a method of making composites that incorporates elements of vacuum infiltration, infiltration under an inert gas pressure, and squeeze casting. In this process the reinforcement preform and the matrix are heated up to the liquidus temperature under a vacuum and the matrix is infiltrated into the

preform under pressure from an inert gas. The relatively low temperature lessens the reaction between the matrix and fiber while the low pressure (as compared to squeeze casting) eliminates preform compression. This technique has been successful for aluminum matrix composites reinforced by materials such as silicon carbide, alumina, and graphite.

Another infiltration process has been developed by Stinton et al. (24) in which silicon carbide reinforced composites are made by chemical vapor infiltration of the matrix material. In this method the bottom part of the silicon carbide preform is water cooled while the upper part is exposed to a hot zone, creating a large temperature gradient across the preform. The reactant gases pass through the cold part of the preform and do not react because of the low temperature. As these gases reach the hot zone, they deposit on and around the reinforcement to form the matrix. The deposition of the matrix in the hot zone increases the density and thermal conductivity of the preform, causing the hot region to progress from the top of the preform toward the bottom, forming the composite.

1.3 Objective of the Present Research

Although infiltration has some deterring factors, such as possible reaction of the reinforcement with the liquid

metal and lack of proper wetting of the molten metal on the ceramic, it offers an economic advantage over the processes just described. In order to take advantage of the technique, a better understanding of the process variables must be attained.

Previous work by Maxwell (25) resulted in the derivation of a model to describe the infiltration kinetics of infiltrating aluminum into porous silicon carbide compacts. Maxwell studied process parameters such as void characteristics, pressure, temperature, and alloying of the matrix. His work also led to the discovery of an incubation time for the process. Seitz (26) then proceeded to analyze the incubation period and discovered an activation energy for the incubation time.

In this work efforts are made to characterize the variables that affect infiltration time. The effect of particle size on infiltration time is studied as well as the effects of adding aluminum powder to the silicon carbide compact before infiltration. An activation energy of viscosity of the process is analyzed, and a method for packing the preform is also developed.

2.0 LITERATURE REVIEW

In order to have a better comprehension of the factors affecting the infiltration process, published literature was reviewed. The points of interest were the physical properties of aluminum (especially liquid aluminum), the compatibility between silicon carbide and liquid aluminum, the wettability of molten aluminum on silicon carbide, packing of the preform, and the thermodynamics and kinetics of liquid metal infiltration.

2.1 Physical Properties of Aluminum

This section studies some of the physical properties of aluminum, especially some of the properties of liquid aluminum that affect the infiltration kinetics. Aluminum crystallizes in the face-centered cubic structure that is stable from 4°K to the melting point. The coefficients of thermal expansion of aluminum are given in Figure 2.1 (27), and the density of aluminum is 2698.72 kg/m³. Some of the mechanical properties of aluminum are given in Table 2.1.

2.1.1 Density of Liquid Aluminum.

According to the Handbook of Chemistry and Physics (29) density is the concentration of matter, measured by the mass

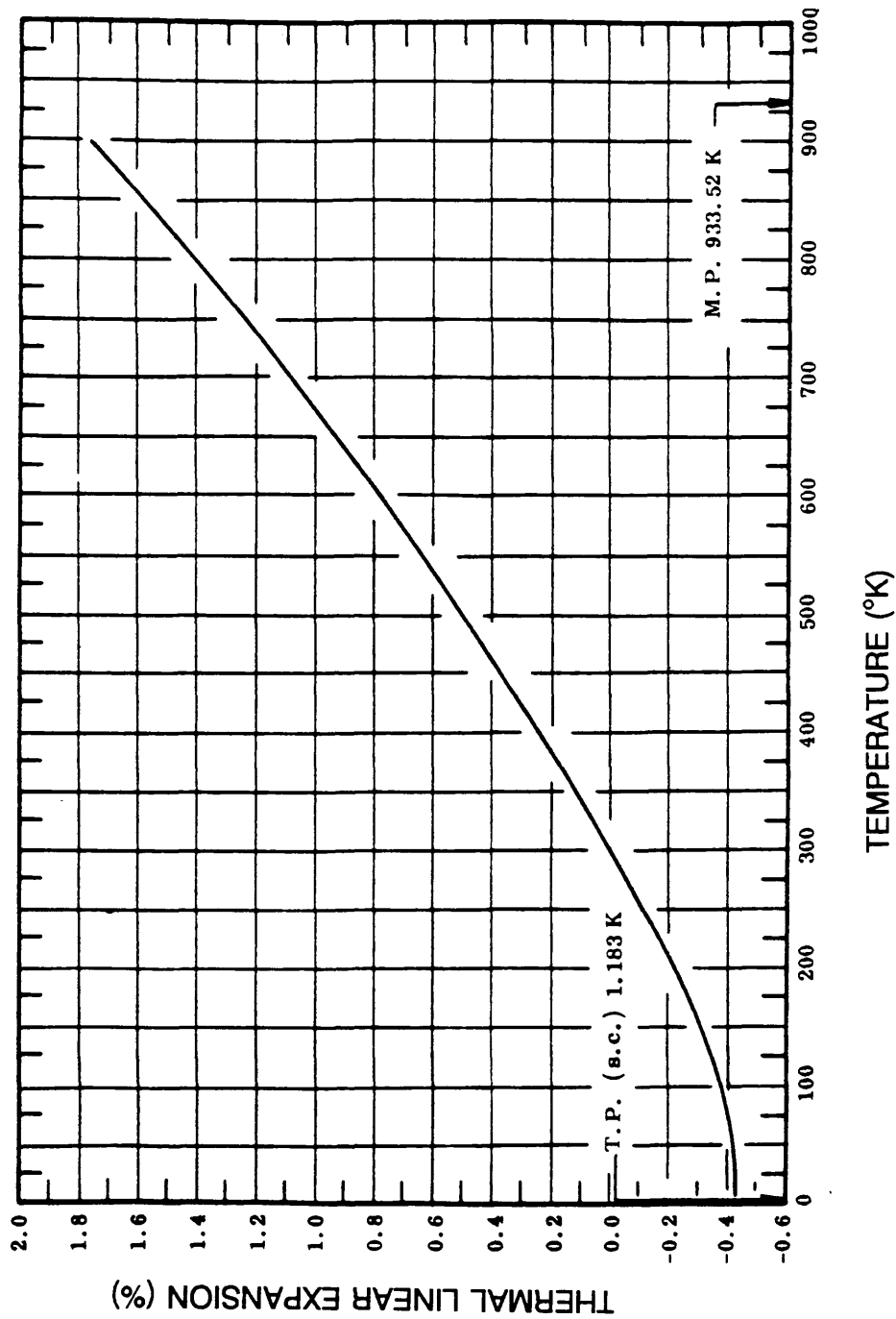


Figure 2.1: The recommended values for the thermal linear expansion of aluminum (27).

Table 2.1

Mechanical Properties of Pure Aluminum at Room Temperature

| Purity | Ultimate | | Elongation in 50 mm |
|--------|---------------------|---------------------|------------------------|
| | Tensile Strength | Tensile Strength | |
| % | MPa | MPa | % |
| 99.99 | 10 | 45 | 50 |
| 99.8 | 20 | 60 | 45 |
| 99.6 | 30 | 70 | 43 |

Source: Hatch, J.E., Aluminum: Properties and Physical Metallurgy; American Society for Metals, Metals Park, Ohio pp.1-24 (1984).

per unit volume. When the aluminum melts to form a liquid, it loses its periodicity of structure, causing the density to decrease. Even though the liquid does not have the long range order of the solid, it does have short range order and a coordination number close to that of the solid. Long range order is not present in liquid metals because of the presence of structural defects, the exact nature of which is not known. These structural defects can also help account for the decrease in density (30). There is a little discrepancy in the literature on the exact change of the density of liquid aluminum with temperature (31, 32, 33, 34, 35), but the general trend of density decreasing linearly with increasing temperature is valid. Figure 2.2 shows the density dependence on temperature (31).

2.1.2 Surface Tension of Liquid Aluminum.

According to the Handbook of Chemistry and Physics (29), surface tension is when fluids in contact exhibit a phenomenon due to molecular attraction which appears to arise from a tension in the surface of separation.

The variation of the free energy, F , of a bulk

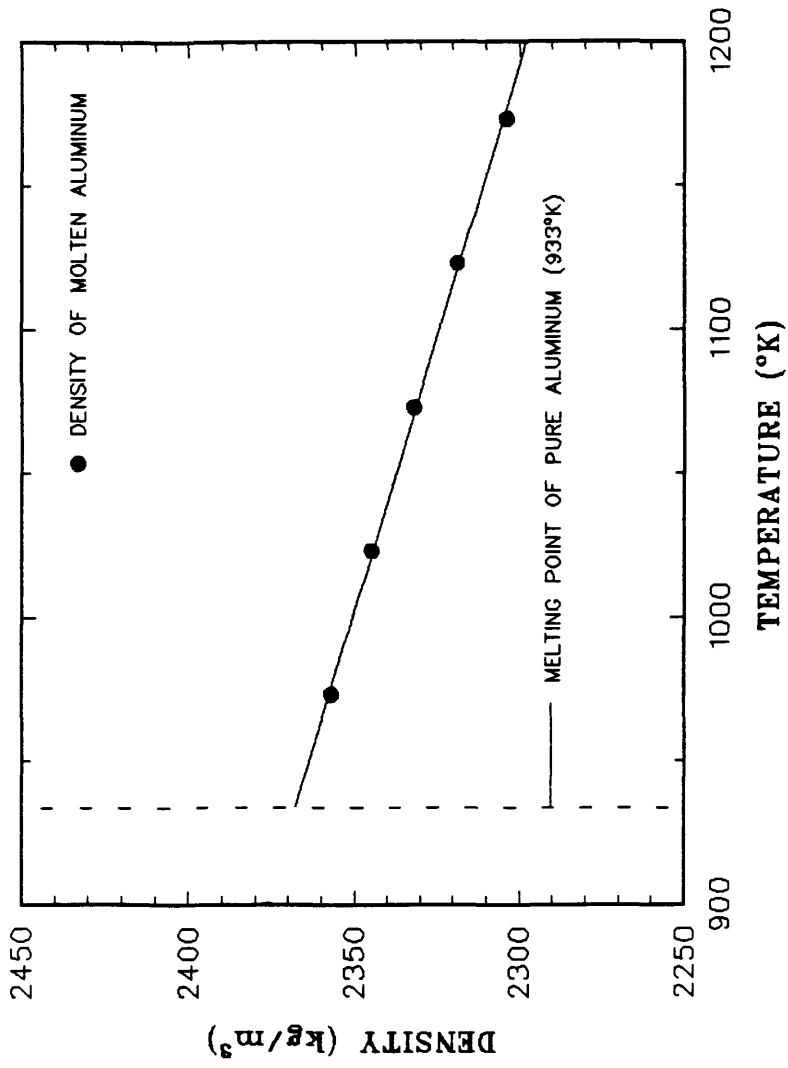


Figure 2.2: The density of liquid aluminum as a function of temperature (31).

homogeneous phase can be written as (34):

$$dF = -S dT + V dP + \sum \mu_i dn_i \quad (2.1)$$

where: S is the entropy, T is the temperature, V is the volume, P is the pressure, μ_i is the chemical potential of component "i", and n_i is the number of moles of component "i".

In a heterogeneous system of one or more components and two phases, a surface of separation will exist between the phases. The thickness of the transition region from one phase to another across the boundary surface is inconsequential, provided that it contains all parts of the system that are within the influence of the surface forces. If the additional free energy accompanying a change in surface area is accounted for, equation (2.1) can be modified. The work required to increase the area of the surface by an infinitesimal amount dA , is equal to γdA (the term γ denotes surface tension), at constant temperature, pressure, and composition. Using this additional information, equation (2.1) can be recast as:

$$dF^s = -S^s dT + V^s dP + \gamma dA + \sum \mu_i dn_i^s \quad (2.2)$$

where the superscript "s" signifies the surface phase. At constant temperature, pressure, and composition, the surface

tension can be written as:

$$\left(\frac{\partial F}{\partial A}\right)_{T,P,\mu_i} = \gamma \quad (2.3)$$

This means that the surface energy, F , per unit area, A , and the surface tension, γ , are identical for a liquid under these conditions. Figure 2.3 exhibits some values of surface tension for liquid aluminum as a function of temperature.

Mondolfo (35) reviews measurements and calculations for the interfacial energies of molten aluminum. Trace levels of impurities and the atmosphere above the liquid can change the surface tension of molten aluminum. Even models for calculating surface tension yield different results. Reviews of earlier work have led to the development of equations for surface tension of aluminum and aluminum with small amounts of alloying elements (28).

2.1.3 Viscosity of Liquid Aluminum.

The Handbook of Chemistry and Physics (29) defines viscosity as the resistance of a fluid to change in form. The viscosity of a liquid decreases with an increase in temperature. The Spanish physical chemist J. de Guzman (37) discovered that the viscosity of a liquid follows an

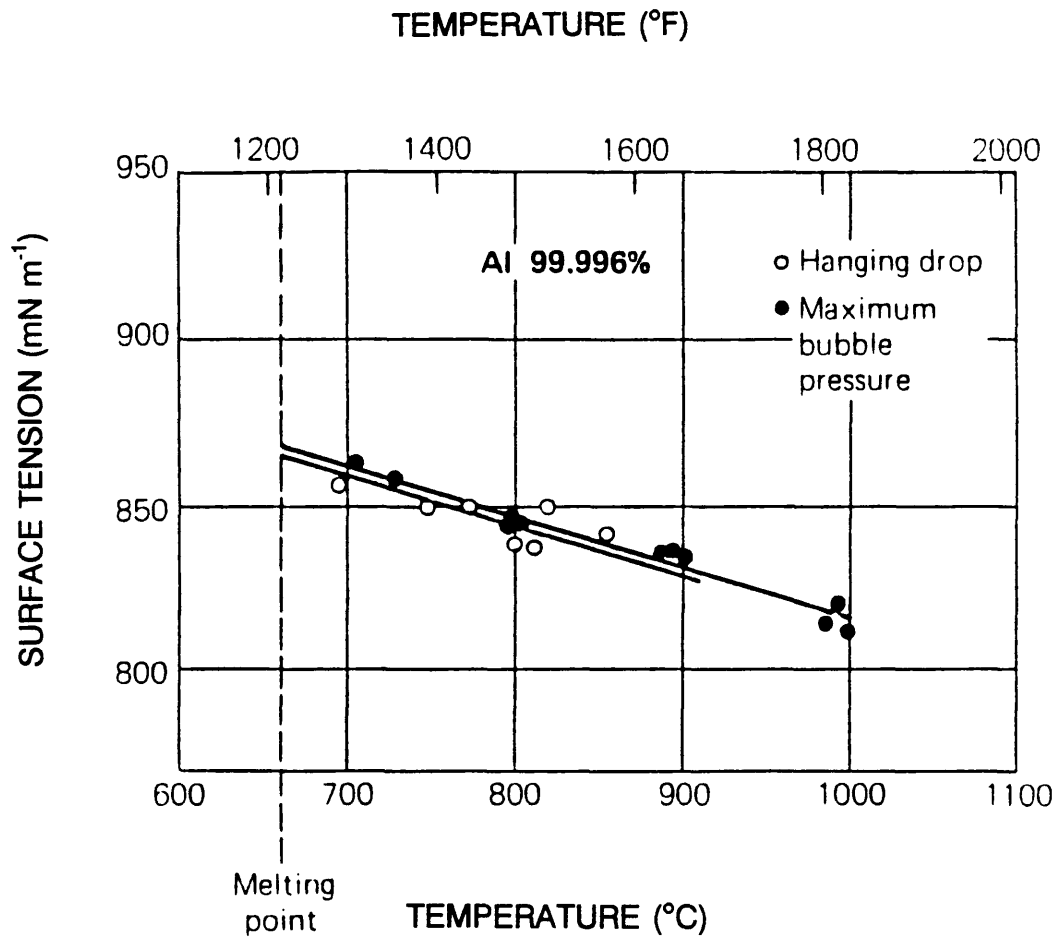


Figure 2.3: Surface tension of liquid aluminum as a function of temperature (28).

Arrhenius type of law:

$$\eta = A \exp\left(\frac{E_{vis}}{RT}\right) \quad (2.4)$$

where: A is the pre-exponential factor, E_{vis} is the activation energy for the viscous flow of the liquid, R is the gas constant, and T is the absolute temperature. This form was later verified by Andrade (38, 39).

The detailed theory on the viscosity of liquids is complex so only the general ideas are presented here. Consider two layers of liquids, one moving in the same direction faster than the other. There are additional layers above and below the two layers, and in order for motion to occur, the molecules will have to push the neighboring molecules aside. Consequently, there is an energy barrier for the process, yielding the activation energy for the viscous flow of the liquid (37). Metals are not molecular in nature, but they still portray an activated behavior. Figure 2.4 shows a plot of the logarithm of the viscosity of liquid metals versus the inverse of the absolute temperature (40). Aluminum exhibits a linear behavior on this plot, and hence, it will be assumed in later analyses that equation (2.4) is valid for the system being studied. Arsent'ev et al. (41) found a range of activation energies of viscosity for pure aluminum on the

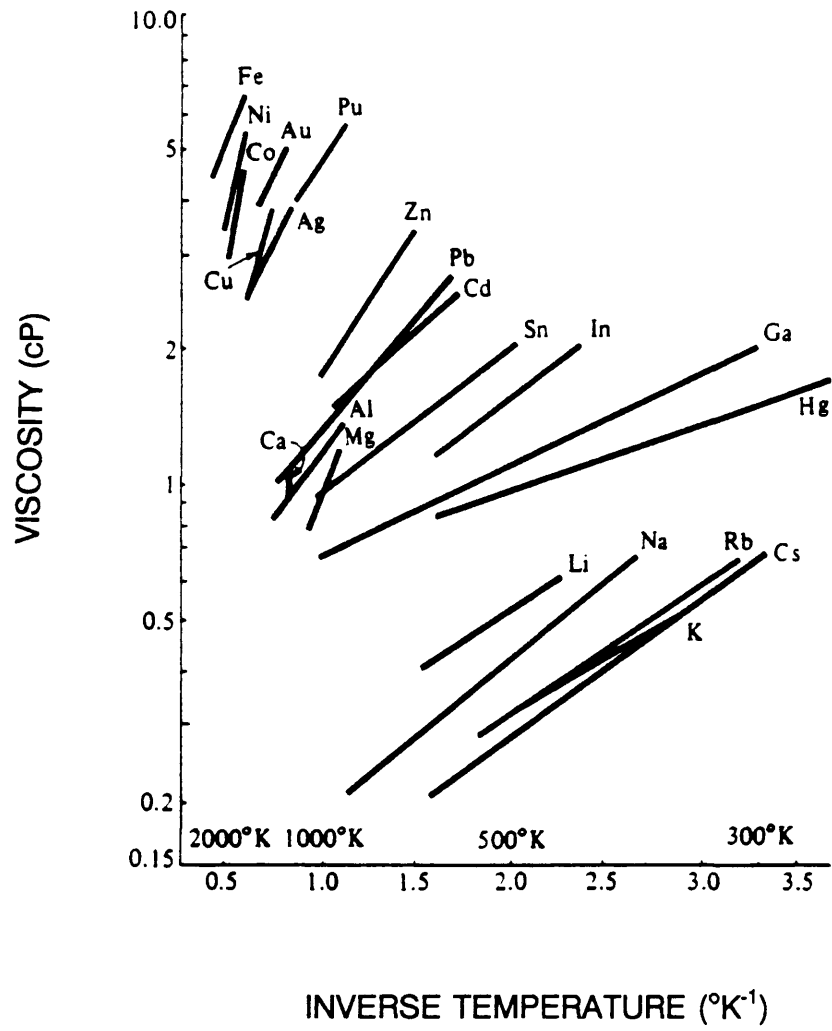


Figure 2.4: The viscosity of liquid metals and their dependence on temperature (40).

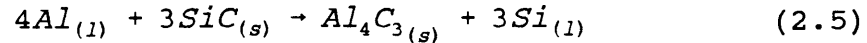
order of 13.8 to 21.0 kJ/mole, the variation resulting from impurities. Gebhardt et al. (42) reported a value of 11.6 kJ/mole for the activation energy of viscosity.

2.2 Silicon Carbide/Aluminum Interface

The reinforcement/metal interface is important in determining the end properties of the composite. Reinforcement reactivity can result in degradation of the reinforcement, which will result in the diminishing of properties. The reinforcement and matrix constituents must come into molecular contact to form an interface which is capable of transferring the load in the case of fiber reinforcements. The load transfer indicates that interfacial bonding must occur with minimum reactivity. Thus, an efficient interface must be formed with minimum degradation of the fiber (11).

Two mechanisms have been proposed to describe the aluminum/silicon carbide interface: 1) there is an SiO_2 film or layer between the silicon carbide and aluminum and 2) there is an Al_4C_3 film between the silicon carbide and the aluminum matrix (43). The second mechanism has been put forward on a thermodynamic basis and will be considered here. As mentioned earlier, the reaction between aluminum

and silicon carbide is:



The free energy change for the reaction is (44):

$$\begin{aligned} \Delta G(J/mole) = & 113,900 - 12.06T \ln T \\ & + 8.92 \times 10^{-3}T^2 \\ & + 7.53 \times 10^{-4}T^{-1} \\ & + 21.5T + 3RT \ln a_{[Si]} \end{aligned} \quad (2.6)$$

where ΔG is the free energy change, T is the absolute temperature, and $a_{[Si]}$ is the activity of the silicon in liquid aluminum. Although the free energy change of the reaction is positive for the temperature range under consideration in this work (943 to 1023°K), the phase diagram for the aluminum/silicon system indicates that silicon does dissolve in liquid aluminum. The amount of silicon in the liquid aluminum increases as the reaction progresses until a saturation value is reached. The concentration of silicon in liquid aluminum, N_{Si} , can be written as (44):

$$N_{Si} = \frac{3\alpha}{4(1 - \alpha) + 3\alpha} \quad (2.7)$$

where the saturated value for the extent of the reaction, α ,

is:

$$\alpha = \frac{4N_{Si}}{3 + N_{Si}} \quad (2.8)$$

When α reaches approximately 0.22 at 1273°K, it is estimated that the reaction will saturate. If 10 weight percent of silicon is added to the aluminum and then heat treated to 1273°K, the reaction will saturate at about α equal to 0.95. Thus, the addition of silicon to liquid aluminum can reduce the amount of reaction.

Chernyshova et al. (45) have reported that Al_4C_3 was found to grow when the metal crystallized from the supersaturated solution in the shape of rectilinearly faceted crystals. They found that the silicon carbide mass changes continuously. They determined parameters for the dissolution of carbon into liquid aluminum with a modification of the Nernst-Schukarev equation:

$$\frac{\Delta m}{m_i} = 1 - \exp(-\alpha_i \frac{S}{V} \tau^n) \quad (2.9)$$

where Δm is the loss of mass over the time τ , m_i is the loss of mass corresponding to the saturation of the solution, α_i is the dissolution rate constant, S is the surface area of contact, V is the melt volume, and "n" is the order of the dissolution reaction. They reported the

order of reaction, "n", to be 0.3 and the dissolution constant, α_i , to be 1×10^{-14} m/sec.

Arsenault et al. (43) studied aluminum penetration into silicon carbide and found the penetration to be significantly larger than an average diffusion distance calculation of $(Dt)^{1/2}$, where D is the diffusivity and "t" is the time. They report that there is solubility of Al_4C_3 in silicon carbide according to the Al_4C_3 -SiC phase diagram. The solubility does not, however, explain the relatively large penetration values they observed. They state that the second law of thermodynamics explains the presence of aluminum in silicon carbide since the entropy of mixing reduces the free energy of reaction. They conclude that the depth of aluminum penetration in silicon carbide must be due to a short circuit path.

From the above discussions it can be seen that the growth of the Al_4C_3 film is an important consideration. This growth should be controlled (e.g. as by the addition of silicon to the melt as explained above) so that a composite of good quality will result. Also, the processing can be controlled so that the time in which the components can react is minimal.

2.3 Wetting of Silicon Carbide by Liquid Aluminum

Successful infiltration of the molten metal into the reinforcement preform requires that the melt should wet the ceramic phase. The wetting behavior is usually determined by sessile drop experiments, as depicted in Figure 2.5. This method ascertains the value of the product of the liquid-vapor surface tension and cosine of the contact angle. A force balance, according to Figure 2.5, results in the Young-Dupre equation:

$$\gamma_{SV} = \gamma_{SL} + \gamma_{LV}\cos\theta \quad (2.10)$$

The contact angle, θ , must be less than 90 degrees for wetting to occur. According to equation (2.10), the contact angle between a liquid and a solid can be decreased by either one or all of the following factors: 1) increasing the surface energy of the solid, γ_{SV} , 2) decreasing the interfacial energy between the solid and liquid, γ_{SL} , and 3) decreasing the surface tension of the molten metal (46, 47).

These principles have been used to develop techniques for improving wettability. Some of these techniques will now be discussed briefly. The use of metallic coatings (e.g. copper and nickel) on ceramic particles increases the overall surface energy of the solid and improves wetting by

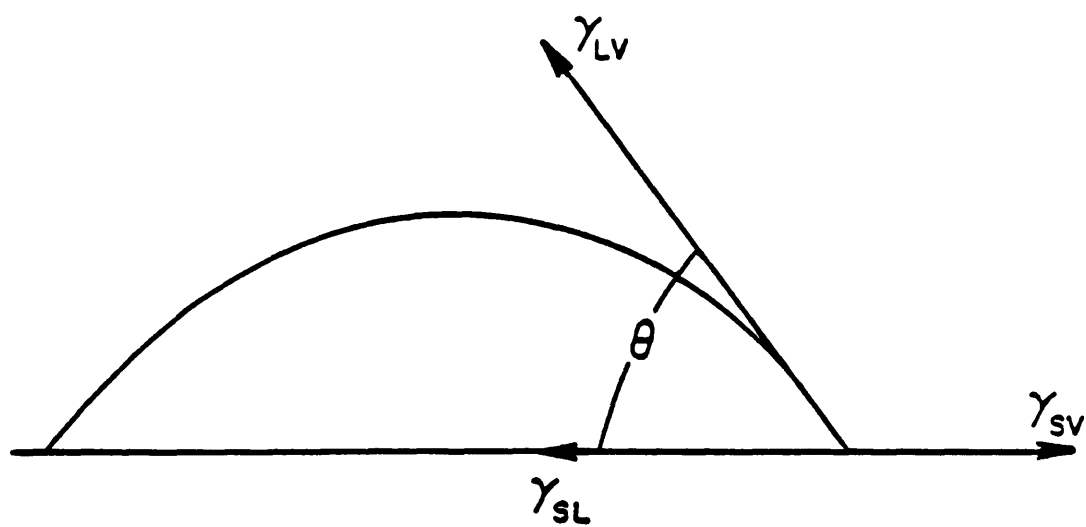


Figure 2.5: Schematic diagram of a sessile drop used to measure wettability.

changing the contacting interfaces to metal/metal instead of metal/ceramic (which are often non-wetting). The use of reactive elements may enhance wetting by reducing the surface tension of the melt, decreasing the solid/liquid interfacial energy of the melt, or inducing wettability by chemical reaction. Very small quantities of reactive elements may be quite effective in improving wetting since they segregate either to the melt surfaces or at the melt/ceramic interface.

Heat treatment of particles before their dispersion in a melt (as in casting) aids in their transfer by causing desorption of adsorbed gases from the ceramic surfaces. Ultrasonic vibrations promote the wetting of ceramic particles by metallic melts as a result of partial desorption of adsorbed gases from the surface of the particles, and in addition, they supply the excess energy for melt cavitation which facilitates particle dispersion in the melt (48).

The bonding force between the liquid and solid, or work of adhesion, W_a , is defined as:

$$W_a = \gamma_{LV} + \gamma_{SV} - \gamma_{SL} \quad (2.11)$$

Combination of equations (2.10) and (2.11) yields:

$$W_a = \gamma_{LV}(1 + \cos\theta) \quad (2.12)$$

Thus, the bonding force between the liquid and solid phases can be expressed in terms of the contact angle and the surface tension of the liquid. These variables can be measured experimentally using the sessile drop experiment (47).

There are many references in the literature that discuss the wettability of aluminum on silicon carbide (49-53). Figure 2.6 shows some data for the variation of the contact angle of liquid aluminum on silicon carbide with temperature, and Figure 2.7 shows the variation of $\gamma_{LV}\cos\theta$ for liquid aluminum on silicon carbide with temperature.

2.4 Vibratory Packing of Particulate Beds

The objective of packing particles by vibration is to increase the density and uniformity of packing. The main factors that affect packing particles using this method are the characteristics of the powder (size distribution, shape, and surface condition) and the vibration variables (frequency, amplitude, and time). Other factors include segregation by size and shape as well as particle density (for multi-component systems). The wall effect can also

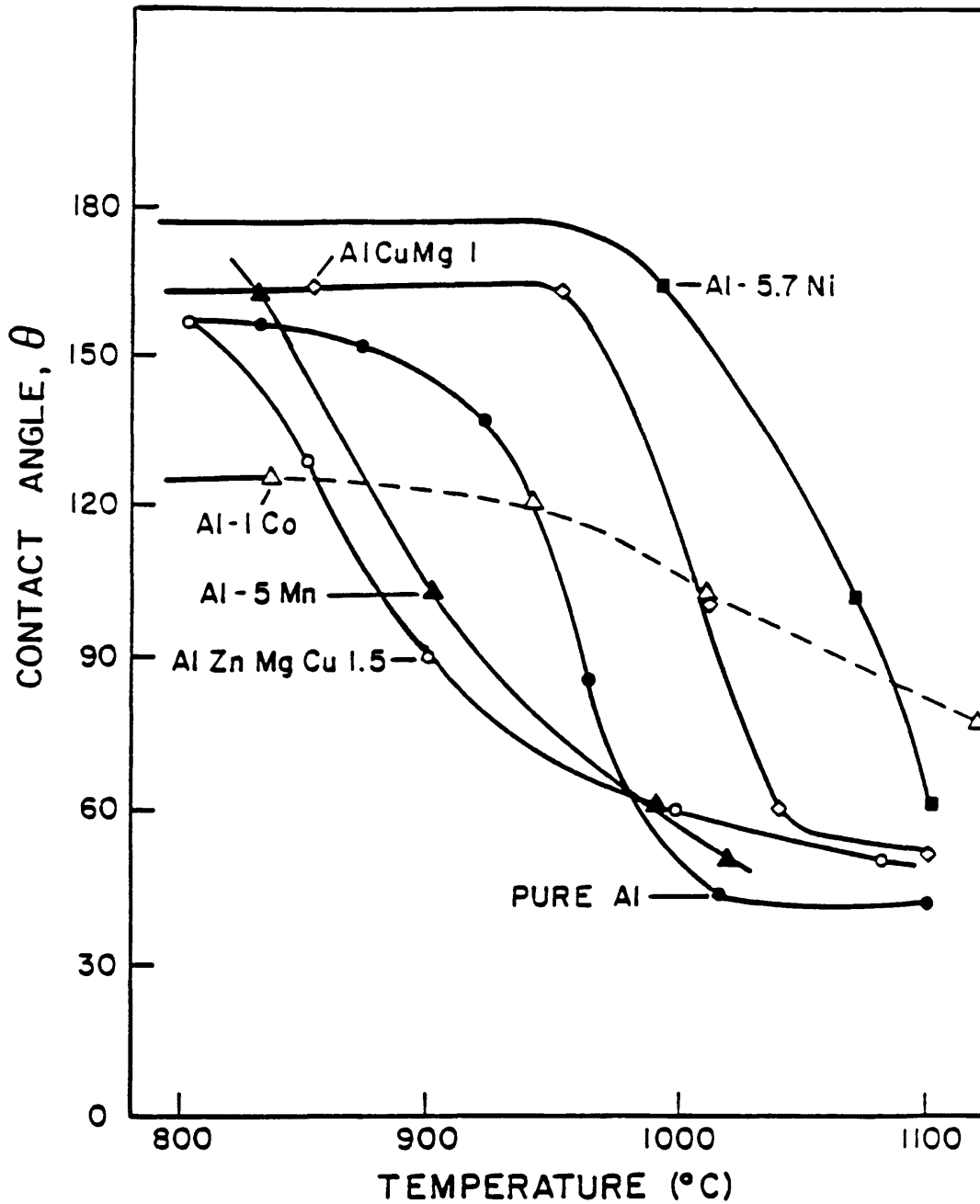


Figure 2.6: The contact angle for liquid aluminum on silicon carbide as a function of temperature and alloy composition. AlCuMg1 = 3.5-4.5% Cu 0.4-1% Mg, 0.3-1% Mn; AlZnMgCu1.5 = 5.1-6.1% Zn 2.1-2.9% Mg, 1.2-2% Cu, 0.18-0.3% Cr, 0.3% Mn (52).

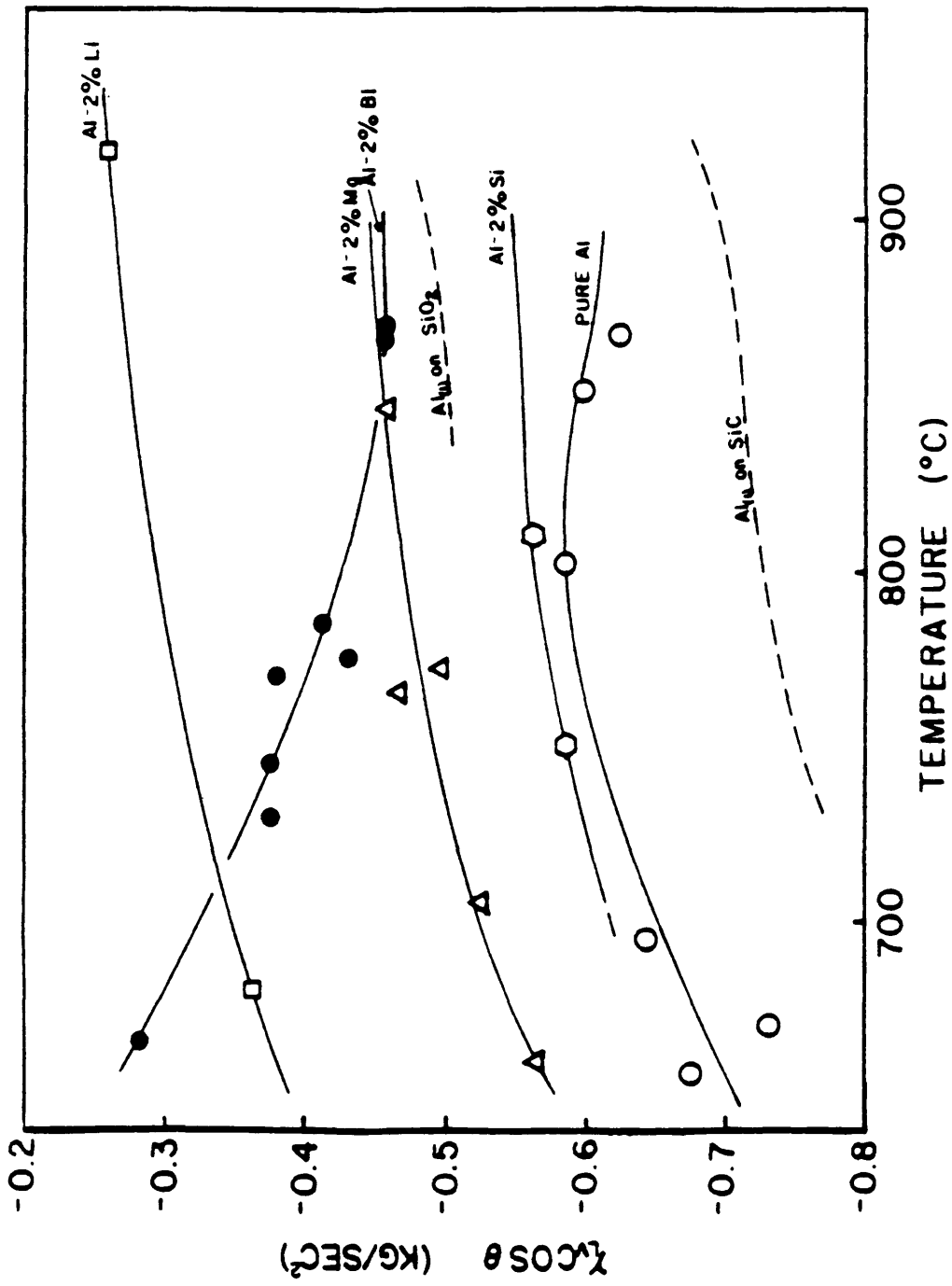


Figure 2.7: The wettability of aluminum on silicon carbide as a function of temperature and composition (53).

have an influence on the packing of particles in the surrounding region.

Review of the literature leads to the following factors as being important in the vibratory packing of powders (54 and 55):

- 1.) For particles of a certain shape, the limiting factor for high density packing is the size distribution.
- 2.) Blends that give high densities with one type of powder do not necessarily do the same for another type.
- 3.) Spherical particles pack with higher densities than irregular ones, but there is a greater effect in increasing the density of irregular powders with vibratory packing.
- 4.) Vibration gives the greatest increase in density around certain fixed frequencies assumed to be the resonant frequencies of the system and will depend upon the apparatus itself and the powder used.
- 5.) For a system with a large size distribution of particles, a change of frequencies of vibration which affect all the different sizes can be effective.

- 6.) Packing is improved by low rates of deposition and by simultaneous vibration and packing.

2.5 Infiltration

In order to exploit infiltration as a production method for making composites, a better understanding of the process variables has to be attained. This section reviews the literature discussing the thermodynamics and kinetics of infiltration. Specifically, the model developed for Maxwell (25) will be discussed in the kinetics as it applies to the system under study.

2.5.1 Thermodynamics of Infiltration.

In order for infiltration to occur successfully, the laws of thermodynamics require that the end phase of infiltration has a lower free energy than the beginning stage. If all of the surface free energies from before and after infiltration are summed, the result is the infiltration index, I , described by Shaler et al. (56) as the indication of the inclination for infiltration to occur. The work of Shaler will be discussed at this point. In the model put forth by Shaler, it can be said that for an ideal system (simple geometry), the index of infiltration must be positive for infiltration to occur.

The geometric configuration of the model involves the infiltration of a semi-infinite plate with a distribution of straight cylindrical pores as shown in Figure 2.8. The pores are perpendicular to the face of the plate and have uniform radii. The porosity of the system, ϕ , is described as the ratio of the volume of the pores to the volume of the plate that has a height, "h":

$$\phi = \frac{a}{(A + a)} \quad (2.13)$$

where the variables are as described in Figure 2.8. The volume of liquid is the same as that of the pores of each cell so that:

$$(A + a)l = ah \text{ or } l = \phi h \quad (2.14)$$

Thus the geometry of the system can be characterized by "r", "h", and ϕ . An energy balance of the system (calculation of I), relies on the specific surface free energies, the shape of the meniscus, and the external pressures exerted upon the liquid. The surface free energies can be found from equation (2.10). When the capillary radius is small, the shape of the meniscus is estimated to be a spherical cap with an area of $2\pi r^2/(1 + \sin\theta)$. The work done by the outside pressure exerted on the porous body is $(P_1 - P_2)\pi r^2$, where P_1 is the pressure upon the liquid layer, and P_2 is

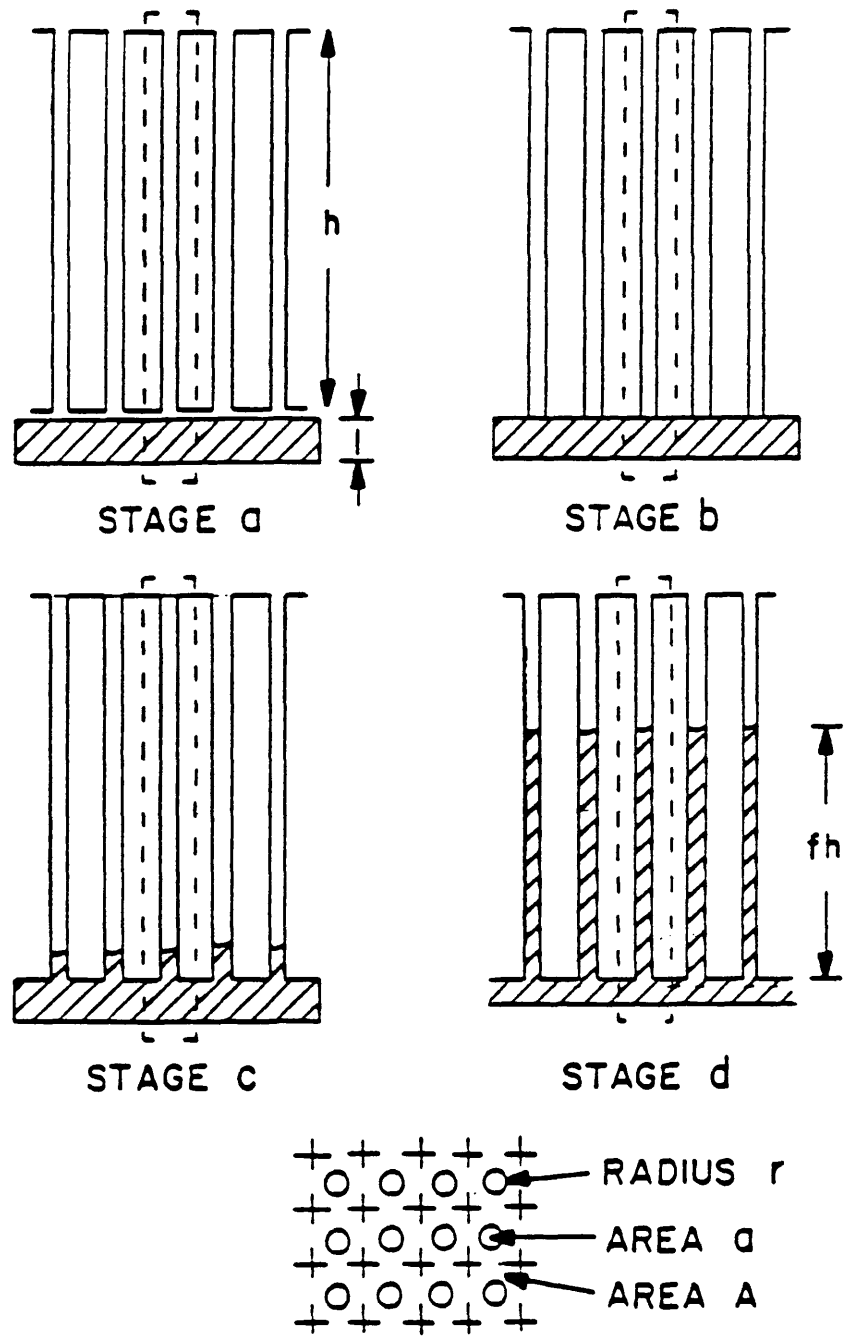


Figure 2.8: The possible stages of infiltration of a porous plate (56).

the pressure in the pore.

Using the definition for the infiltration index given above (i.e. sum of the free energies), the tendency for one of the states in Figure 2.8 to go to another can be found. If the change in free energy from going to one state to another is negative (i.e. the infiltration index is positive), then the infiltration is spontaneous, provided that there are no metastable states between them. If the infiltration index is negative, it means that some work must be done by external pressure to make the infiltration go from one stage to another.

Shaler et al. calculated the infiltration index for going from one state "a" to another state "b" as shown in Figure 2.8 to be:

$$I_{ab} = \pi r^2 \gamma_{LV} \left[\left(\frac{1}{\phi} - 1 \right) (\cos \theta + 1) \right] \quad (2.15)$$

Since I_{ab} is positive for all values of ϕ , θ , "r", and γ the transition from state "a" to state "b" occurs spontaneously in all systems without the application of an outside pressure.

The next stage of the process is state "c", and the only difference between this and state "b" is the formation of a meniscus spanning each pore opening. The index of

infiltration for "b" going to "c" is:

$$I_{bc} = 2\pi r^2 \left[\left(\frac{1}{2} - \frac{1}{1 + \sin\theta} \right) \gamma_{LV} + yr(P_1 - P_2) \right] \quad (2.16)$$

where "yr" is the volume along the pore axis related to the average distance that the liquid travels upon entering the pore to establish a meniscus. I_{bc} is generally negative so that a meniscus usually does not form immediately.

Following the same line of reasoning I_{bd} for going from state "b" to state "d" is:

$$I_{bd} = 2\pi r^2 \left[\left(\frac{1}{2} - \frac{1}{1 + \sin\theta} + \frac{fh}{r} \cos\theta \right) + \frac{fh}{2} (P_1 - P_2) \right] \quad (2.17)$$

where "f" is the fraction of the total height which is infiltrated. When "f" is small, I_{bd} is always negative. I_{bd} becomes positive for values of fh/r of about 0.5. The significance of this is that the infiltration is spontaneous when an external perturbation forces the liquid into the pores to a depth of half a pore radius. When the infiltration has proceeded fairly far (i.e. at larger values of fh/r) and if the porous body is thick relative to the

pore radius then I_{bd} is governed by:

$$I_{bd} = 2\pi r f h \gamma_{LV} \cos\theta \quad (2.18)$$

It should be noted that this analysis was for an ideal system. Although it can't be used for exact calculations for some real systems, it can be used as a first approximation for determining the proper conditions for infiltration to occur.

2.5.2 Kinetics of Infiltration.

Although the thermodynamics provide for an assessment of conditions under which infiltration may occur, it cannot predict the rate of the process. Hence, the kinetics of the infiltration process will now be discussed.

The kinetics of infiltration can be described by equating the rate of momentum of the liquid within the capillary network, to the forces which act on the liquid. This approach was first developed by Brittin (57, 58) for the rate of rise of a liquid in a capillary. Figure 2.9 shows a schematic of the forces acting on the system. In a wetting system, the surface tension tends to move the liquid up the capillary while it is opposed by the gravitational, viscous, and end drag forces. The resulting change in

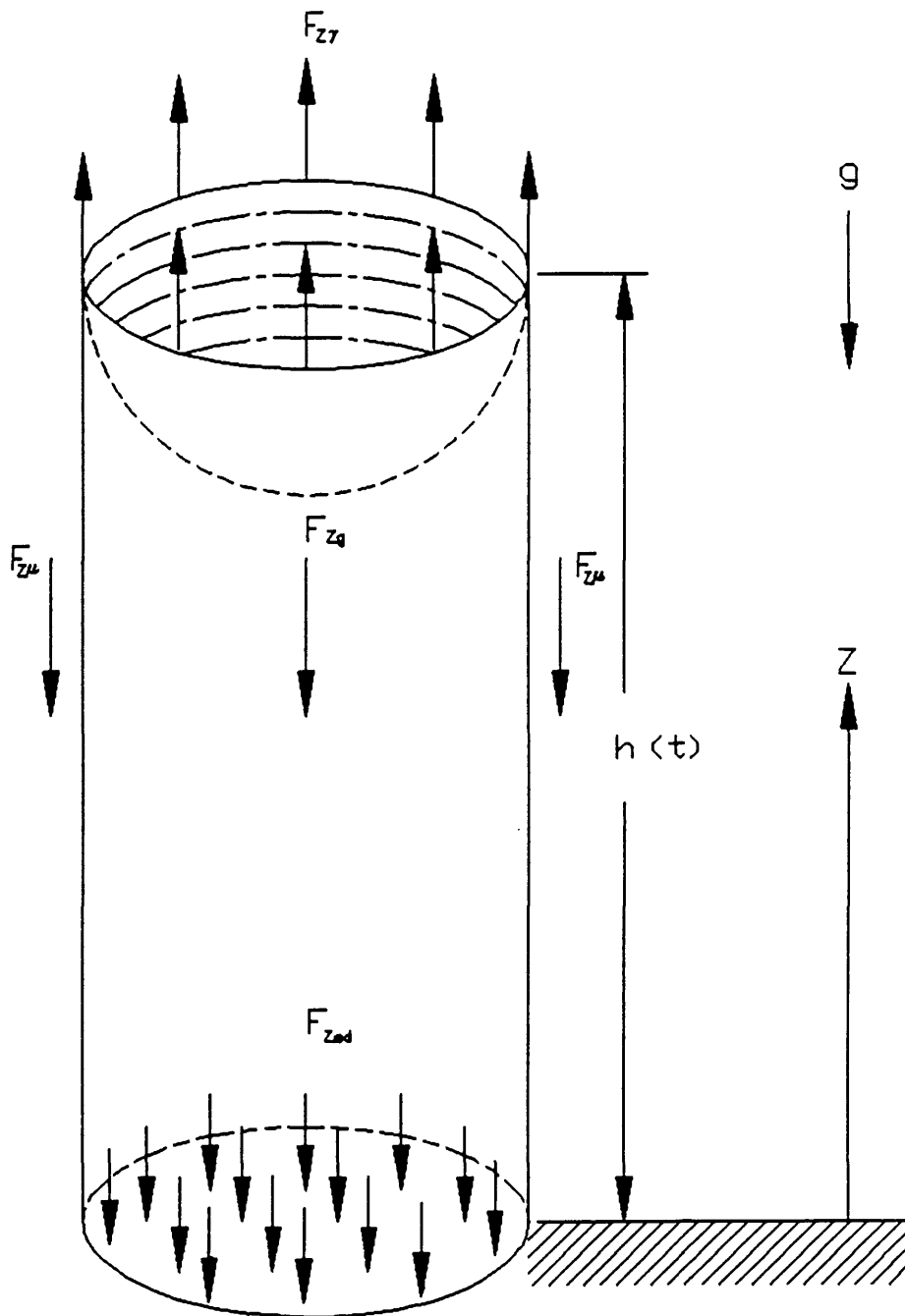


Figure 2.9: Schematic diagram showing the forces acting within a capillary.

momentum due to these forces is:

$$\frac{d}{dt} (m(t) \frac{dh}{dt}) = F_{\gamma} + F_g + F_{\eta} + F_{ed} \quad (2.19)$$

where $m(t)$ is the mass of the liquid in the capillary at time "t", F_{γ} is the force due to surface tension, F_g is the force due to gravity, F_{η} is the force due to viscous resistance, F_{ed} is the force due to end-drag, and "h" is the height of infiltration at time "t". Expansion of this equation results in:

$$\begin{aligned} \pi r^2 \rho \frac{d}{dt} (h \frac{dh}{dt}) &= 2\pi r \gamma_{LV} \cos \theta \\ &\quad - \pi r^2 \rho g h \\ &\quad - 8\pi \eta h \frac{dh}{dt} \\ &\quad - \frac{1}{4} \pi r^2 \rho (\frac{dh}{dt})^2 \end{aligned} \quad (2.20)$$

where "r" is the capillary radius, ρ is the density of the liquid, γ_{LV} is the liquid/vapor surface tension, θ is the liquid/solid contact angle, η is the viscosity of the liquid, and "g" is the gravitational constant. Semlak and Rhines (59) later applied this equation to the infiltration of porous metal bodies, which can be considered as a tangled bundle of tubes with irregular radii. The effective radius can then be determined experimentally.

The system used in the present work introduces aluminum downwards through a porous silicon carbide compact. A

schematic diagram describing the model for this system is shown in Figure 2.10. The parameters necessary to describe the geometry of this system are:

- h_{R0} = initial height of the liquid in the reservoir
- h_c = the distance the liquid has infiltrated at time "t"
- A_c = cross-sectional area of the compact
- r_c = radius of the compact
- r_h = effective pore radius (hydraulic radius)
- d_p = particle diameter
- ϕ = void fraction

The total cross-sectional area of the pores, A_h , is:

$$A_h = \phi A_c \quad (2.21)$$

The equation of continuity can then be employed to equate the height in the fluid in the reservoir, h_R , at time, "t", to the infiltration distance:

$$h_R = \frac{\phi A_c}{\pi r_c^2} h_c - h_{R0} \quad (2.22)$$

The origin is located at the interface between the reservoir and the compact and the positive direction is taken as the direction of flow.

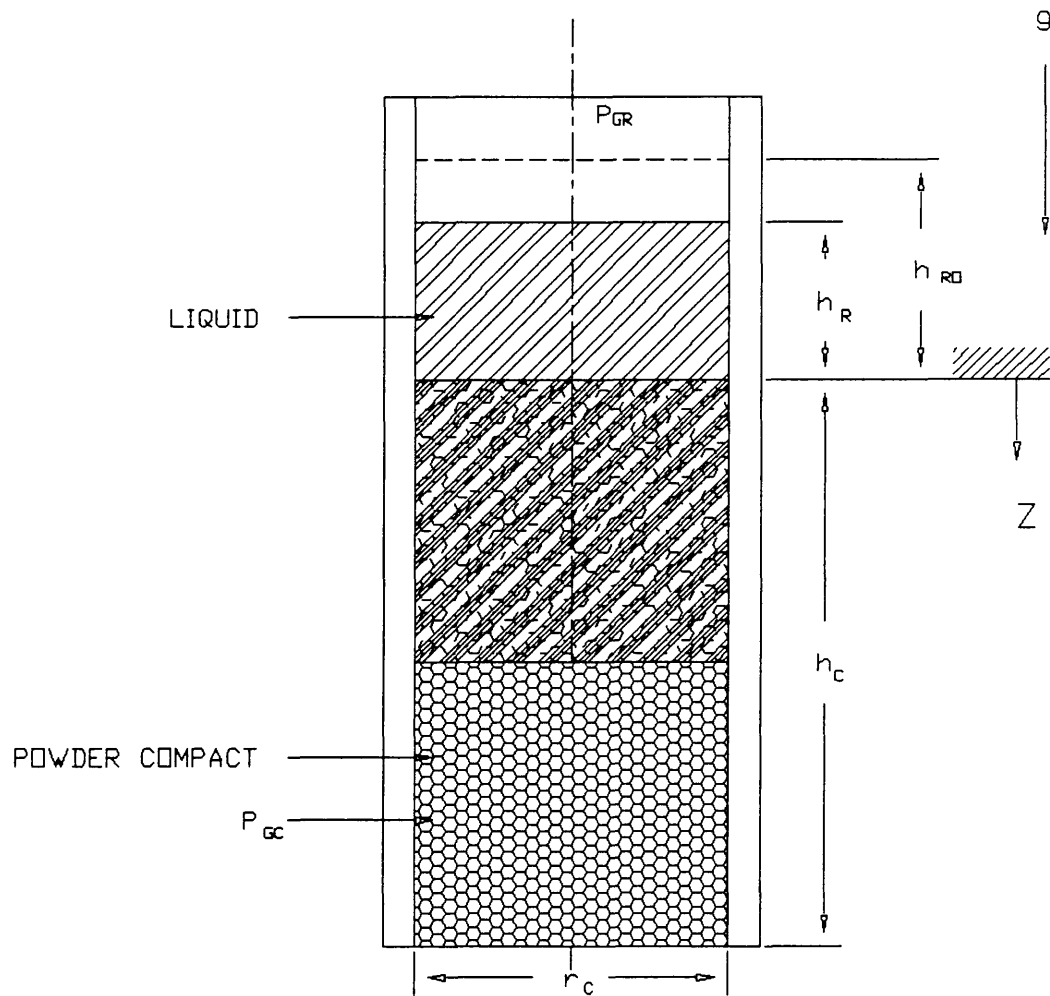


Figure 2.10: Schematic diagram describing the infiltration of a powder compact.

The force balance for Figure 2.10 is:

$$F_p + F_g + F_\eta + = \frac{d}{dt} (m(t) \frac{dh_c}{dt}) \quad (2.23)$$

where F_p is a pressure related force that accounts for the applied pressure, fluid pressure, end-drag, and surface tension instead of being separate as was done by Brittin. This force is related to the pressure drop across the liquid within the compact:

$$F_p = \Delta P \phi A_c \quad (2.24)$$

where:

$$\Delta P = P_{ho} - P_{hc} \quad (2.25)$$

In equation (2.25), P_{ho} is the pressure in the liquid at the reservoir compact interface and P_{hc} is the pressure at the front of the infiltrant. The pressure at the reservoir/compact interface results from the applied pressure in the reservoir, P_{GR} , the fluid pressure, and the end drag. The magnitude of the pressure is then:

$$P_{ho} = P_{GR} + \rho g h_R - \frac{1}{2} \rho \left(\frac{dh_c}{dt} \right)^2 \quad (2.26)$$

The pressure at the front of the infiltrating liquid is a consequence of the gas pressure within the compact, P_{GC} , and the pressure due to surface tension. The value of this

pressure is:

$$P_{hc} = P_{GC} - \frac{2\gamma_{LV}\cos\theta}{r_h} \quad (2.27)$$

The pressure drop across the porous body is then:

$$\Delta P = P_{GR} - P_{GC} + \frac{2\gamma_{LV}\cos\theta}{r_h} + \rho gh_R - \frac{1}{2}\rho \left(\frac{dh_c}{dt}\right)^2 \quad (2.28)$$

The resistance to a fluid flowing through a powder can be modeled using Ergun's equation:

$$F_\eta = -\phi A_c \left[K_1 \eta h_c \frac{dh_c}{dt} + K_2 \rho h_c \left(\frac{dh_c}{dt}\right)^2 \right] \quad (2.29)$$

where:

$$K_1 = 150 \frac{(1 - \phi)^2}{\phi^3 d_p^2} \quad (2.30)$$

and:

$$K_2 = \frac{1.75(1 - \phi)}{\phi^3 d_p} \quad (2.31)$$

The gravitational force acting upon the liquid within the compact is:

$$F_g = \phi A_c \rho gh_c \quad (2.32)$$

The change in momentum can be rewritten:

$$\frac{d}{dt} (m(t) \frac{dh_c}{dt}) = \rho \phi A_c \frac{d}{dt} (h_c \frac{dh_c}{dt})^2 \quad (2.33)$$

Equating the sum of the forces given above to the rate of change in momentum and dividing through by ϕA_c yields:

$$\begin{aligned} \rho \frac{d}{dt} (h_c \frac{dh_c}{dt}) &= P^* + \frac{2\gamma_{LV} \cos \theta}{r_h} + \rho g h_R - \rho \left(\frac{dh_c}{dt} \right)^2 \\ &\quad - [K_1 \eta h_c \frac{dh_c}{dt} + K_2 \rho h_c \left(\frac{dh_c}{dt} \right)^2] \\ &\quad + \rho g h_c \end{aligned} \quad (2.34)$$

where:

$$P^* = P_{GR} - P_{GC} \quad (2.35)$$

Infiltration will only occur if the following condition is met:

$$P^* + \frac{2\gamma_{LV} \cos \theta}{r_h} + \rho g h_{RO} > 0 \quad (2.36)$$

The expression on the left hand side of equation (2.36) defines the effective pressure, P_{eff} . When the effective pressure is zero, then P^* , defines the threshold pressure, P_{th} , which is the applied pressure that must be exceeded in order to initiate infiltration.

The solution of the equation of motion can be

simplified and recast in dimensionless form. Using τ and ξ , to represent the dimensionless values of time and height respectively, the infiltration equation can be written as:

$$\xi^2 \frac{d^2 \xi}{d\tau^2} + B \left(\frac{d\xi}{d\tau} \right)^2 + \lambda_1 \xi \frac{d\xi}{d\tau} - \lambda_2 \xi = 1 \quad (2.37)$$

where:

$$\xi = \frac{h_c}{\langle h \rangle} \quad (2.38)$$

and:

$$\tau = \left(\frac{1}{\langle h \rangle} \left(\frac{P_{eff}}{\rho} \right)^{1/2} \right) t \quad (2.39)$$

and:

$$\lambda_1 = \frac{K_1 \eta \langle h \rangle}{(\rho P_{eff})^{1/2}} \quad (2.40)$$

and:

$$\lambda_2 = (1 - \phi) \frac{\rho g \langle h \rangle}{P_{eff}} \quad (2.41)$$

where: $\langle h \rangle$ is a reference value for height of some arbitrary value. For the system under consideration, λ_1 is large compared to the other terms so that they may be neglected.

Thus, the resulting equation may be solved by integrating, to give the following approximate solution:

$$\frac{1}{2}\xi^2 = \frac{\tau}{\lambda_1} \quad ; \quad 0.1 \leq \xi \leq 1 \quad (2.42)$$

3.0 EXPERIMENTAL PROCEDURE

The objective of the experimental work was to check the validity of the infiltration model discussed earlier. Experiments were run to see how the infiltration time was affected by temperature, pressure, particle size, and additions of aluminum powder to the compact.

3.1 Infiltration Parameters

Permeability tests were run on the various sizes of compacts so that the threshold pressures (minimum pressure required for infiltration) could be determined for various conditions. To assess the threshold pressures, values for the void fraction, effective particle diameter, and effective pore radius had to be acquired. The void fraction could be obtained directly, and the other two factors could be calculated using Ergun's Equation as discussed below.

The void fraction was determined by slowly adding water to the silicon carbide compacts, which were prepared using the same method described in section 3.3. To ensure that the compact was not perturbed by the addition of the water, only one drop of water was added at a time with the aid of a burette. The distance between the tip of the burette and the top of the compact was also minimized to reduce the

amount of disturbance. The specimens were weighed before the addition of the water and after the water appeared right at the top of the compact. The difference in these weights was the weight of the water, which was then equated to the volume using the relation that one gram of water is equal to one cubic centimeter of water at room temperature. Once the volume of water was obtained, it was divided by the total calculated volume of the compact to obtain the void fraction.

In addition to the void fractions, the pressure drops across each type of compact at known flow rates has to be obtained in order to find the corresponding effective particle diameters. The range of flow rates that can be employed are chosen such that they are similar to those that are expected in the infiltration studies. The corresponding flow rates for the permeability tests and the infiltration tests are correlated by first determining the range of Reynold's numbers expected for the infiltration studies and then determining the argon flow rates which will cover this range. The Reynold's number, Re , for this situation is:

$$Re = \frac{\rho V_o}{\eta (1 - \phi) S_o} \quad (3.1)$$

where:

$$S_o = \frac{6}{d_p} \quad (3.2)$$

and:

$$V_o = \frac{Q}{A_c} = \phi \frac{dh}{dt} \quad (3.3)$$

In the above three equations ρ is the density of the fluid, V_o is the superficial velocity, μ is the viscosity of the fluid, ϕ is the void fraction of the compact, S_o is the total surface area of particles per unit volume of particles, d_p is the effective particle diameter, dh/dt is the velocity, Q is the volumetric flow rate, and A_c is the cross-sectional area of the compact.

Before the pressure drops across the compacts can be determined, the pressure drops across the filters have to be determined first. This is because the tests used to find the pressure drops across the compacts include the pressure drop across the compact plus the filter. Once the pressure drop across the filter is obtained, it can be subtracted from the total pressure drop to obtain the pressure drop across the compact. Using Ergun's equation the pressure drop across the filter for viscous controlled flow can be

written as:

$$\frac{dP}{dl} = \frac{150 \eta Q \lambda^2 (1 - \phi)^2}{A_c d_p^2 \phi^3} \quad (3.4)$$

where λ is the shape factor. If compressibility can be disregarded, equation (3.4) can be integrated to yield:

$$\Delta P_F = \frac{150 \eta \lambda^2 (1 - \phi)^2 L Q}{A_c d_p^2 \phi^3} \quad (3.5)$$

where ΔP_F is the pressure drop across the filter and L is the length of the filter. A regression can be employed for the pressure drop and flow rate data for each filter to yield a modification of equation (3.5) in the following form:

$$\Delta P_F = k Q \quad (3.6)$$

where k is the slope of the regression line.

To determine the pressure drop across the compact, compressibility has to be taken into account. This difficulty can be overcome by:

$$\frac{dP}{dl} = \frac{150 \eta \lambda^2 (1 - \phi)^2 Q}{A_c d_p^2 \phi^3} \frac{\rho}{\rho} \quad (3.7)$$

or:

$$\frac{dp}{dl} = \frac{150 \eta \lambda^2 (1 - \phi)^2 G}{A_c d_p^2 \rho \phi^3} \quad (3.8)$$

where G is the mass flow rate. If the gas is considered to be ideal then:

$$\rho = \frac{PM}{RT} \quad (3.9)$$

where: P is the pressure, M is the molecular weight of the gas, R is the gas constant, and T is the absolute temperature. Substituting these values into equation (3.8), integrating, and simplifying yields:

$$(P_2^2 - P_1^2) = K_1 G \quad (3.10)$$

where $(P_2 - P_1)$ is the pressure drop across the compact and K_1 is the slope of line of data regressed in the form of equation (3.10). The constant, K_1 , is also known as the reciprocal of the specific permeability.

The effective particle diameter can then be determined from equation (2.30), and the hydraulic radius, r_H , can be found from the following relationship:

$$r_H = \frac{d_p \phi}{6(1 - \phi)} \quad (3.11)$$

The hydraulic radius can also be written as:

$$r_H = \frac{\text{volume available for flow}}{\text{total wetted surface area}} = \frac{\pi r_h^2 h_c}{2\pi r_h h_c} = \frac{r_h}{2} \quad (3.12)$$

where r_h is the effective pore radius, and h_c is the height of the compact. Thus, the effective pore radius can be found from:

$$r_h = \frac{2d_p \phi}{6(1 - \phi)} \quad (3.13)$$

The threshold pressures can then be determined from the above information as will be discussed in section 4.2.

The permeability tests indicated that a minimum differential pressure of 103 kPa (15 psid) was required. The upper limit of the applied differential pressure of 207 kPa (30 psid) was constrained by the limitations of the differential pressure regulator that was used. A temperature of 670°C was selected so that the tests would be run at least 10°C above the liquidus. The upper limit on temperature was 750°C since infiltration occurred too rapidly to be measured above this temperature. A temperature characterization profile was performed, and it was found that the temperature could be controlled to within plus or minus 2°C within the working zone.

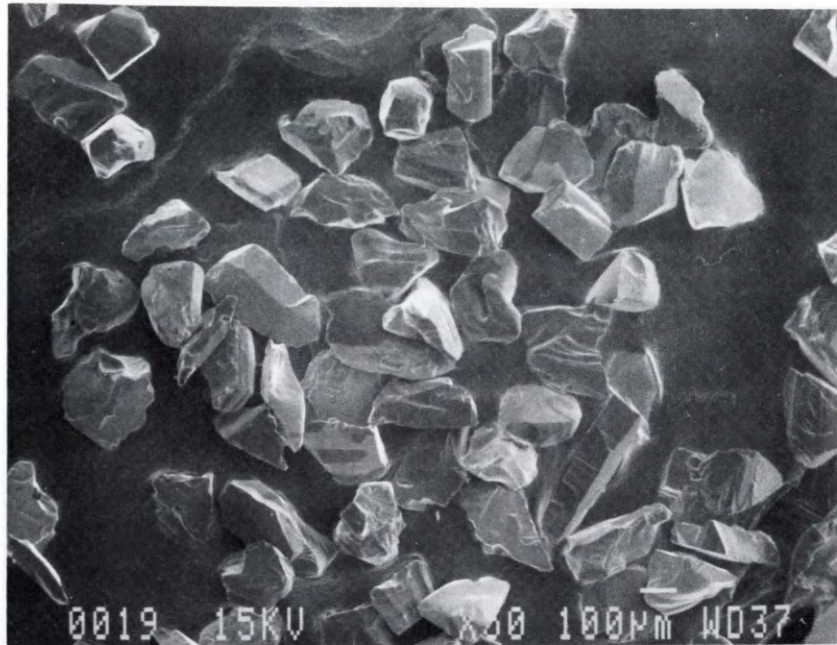
3.2 Materials

The silicon carbide used for infiltration was a high purity α -silicon carbide powder provided by the EXOLON-ESK company. The particles were initially screened on a ro-tap machine, and the particles retained on the 100 and 200 mesh screens were the ones selected for the infiltration tests. The particles were analyzed using a JEOL JXA-840 Scanning Microanalyzer. Figures 3.1, 3.2, and 3.3 show photomicrographs of the 100 mesh, 200 mesh, and the aluminum powder used, respectively. Tables 3.1, 3.2, and 3.3 give the particle size analysis results from the scanning electron microscope. The particles were analyzed using the Particle Recognition and Characterization Program (PRC). The shape factors reported in Tables 3.1, 3.2, and 3.3 are the ratios of the calculated volume for each particle compared to the volume of a sphere equal to that of a reference circle surrounding the particle:

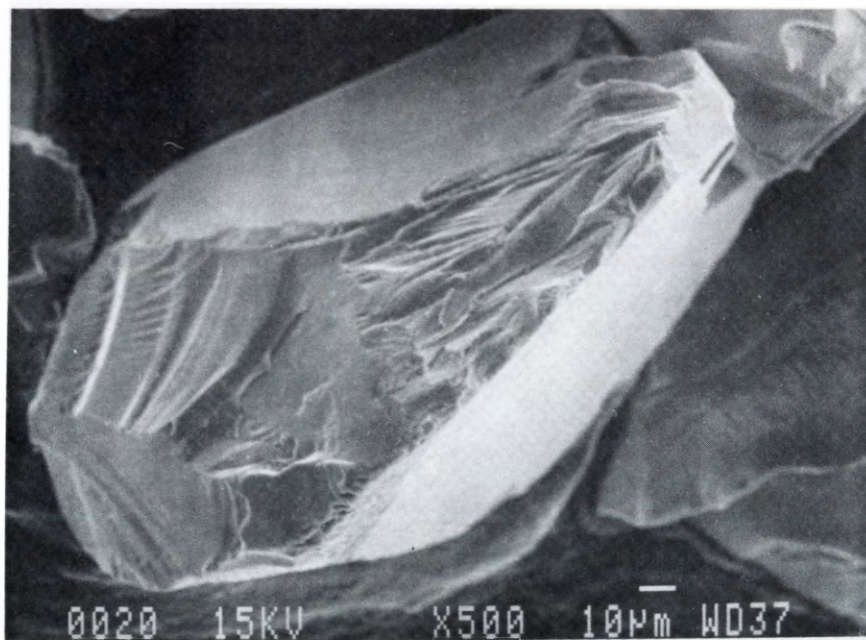
$$shape\ factor = \frac{(perimeter)^2}{(area \times 4\pi)} \quad (3.14)$$

From this point on, the particles retained on the 200 and 100 mesh screens will be denoted by their average particle diameters of 106 and 177 microns, respectively.

The aluminum slugs used for infiltration were produced from materials supplied by Aesar, Johnson Matthey Inc.,

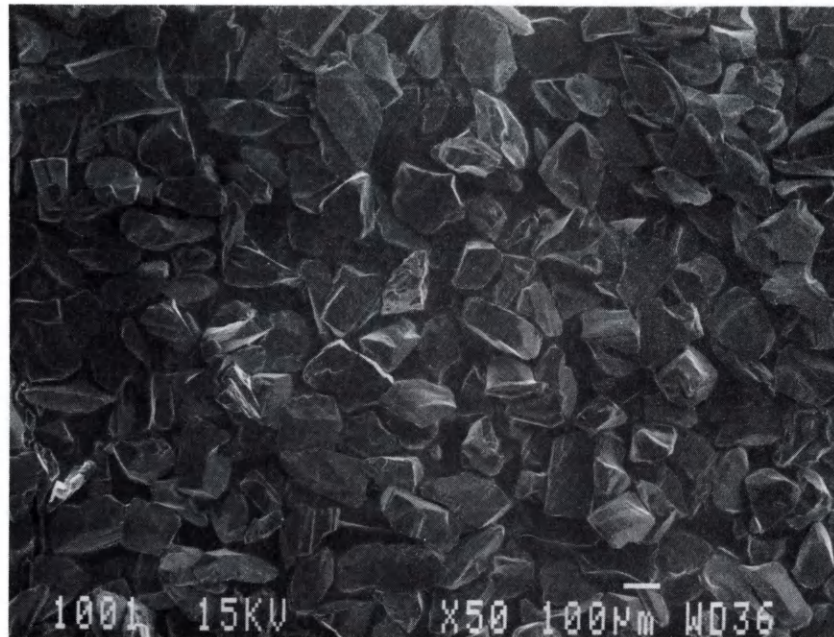


(a)

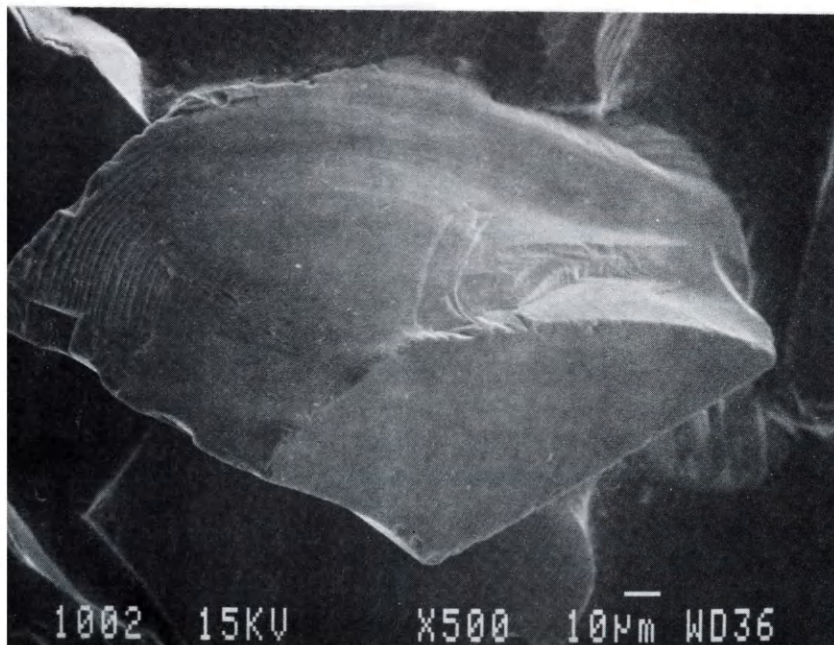


(b)

Figure 3.1 : SEM Photomicrographs of 177 μm silicon carbide particles. (a) 50X (b) 500X

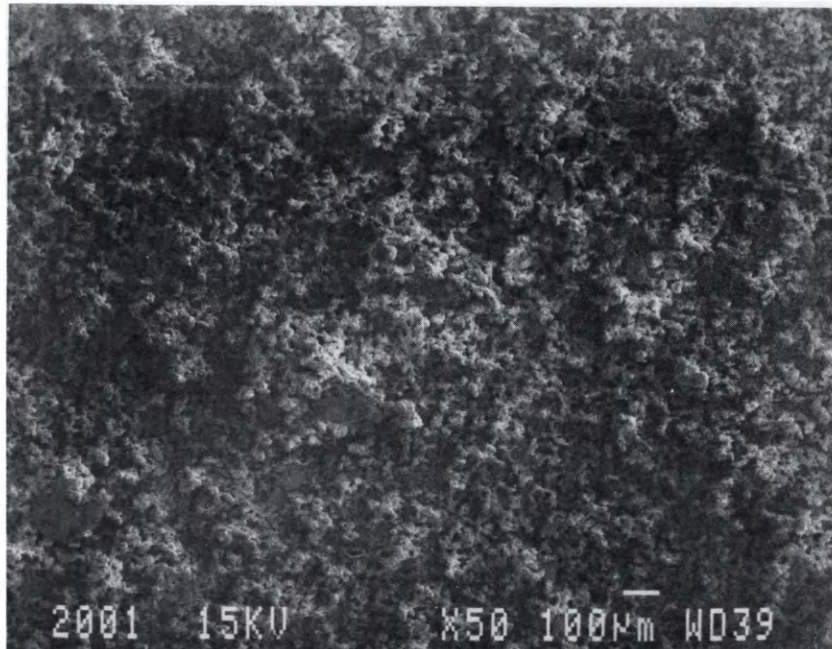


(a)

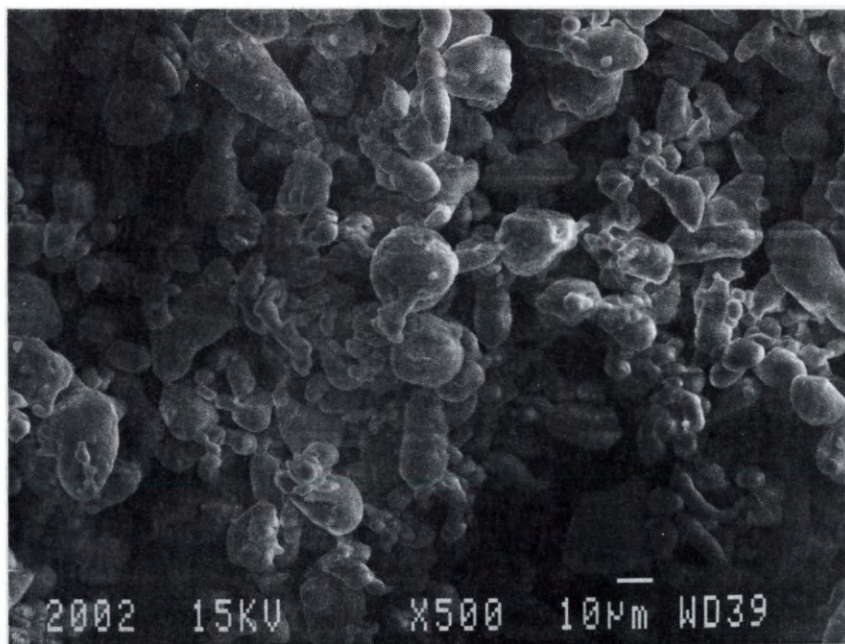


(b)

Figure 3.2: SEM Photomicrographs of 106 μm silicon carbide particles used. (a) 50X (b) 500X



(a)



(b)

Figure 3.3: SEM Photomicrographs of aluminum powder used in tests. (a) 50X (b) 500X

Table 3.1
Characterization of 177 μm Silicon Carbide
Particle Size Analysis*

| | |
|------------------------------------|------|
| Average Diameter (μm) | 177 |
| Maximum Diameter (μm) | 243 |
| Minimum Diameter (μm) | 116 |
| Shape Factor | 1.24 |

* based on 176 particles counted

Table 3.2
Characterization of 106 μm Silicon Carbide

Particle Size Analysis*

| | |
|------------------------------------|------|
| Average Diameter (μm) | 106 |
| Maximum Diameter (μm) | 161 |
| Minimum Diameter (μm) | 1.29 |

* based on 189 particles counted

Table 3.3
Characterization of Aluminum Powder
Particle Size Analysis*

| | |
|------------------------------------|------|
| Average Diameter (μm) | 8.37 |
| Maximum diameter (μm) | 12.5 |
| Minimum Diameter (μm) | 5.0 |
| Shape Factor | 1.02 |

* based on 210 particles counted

which had a purity of 99.95 weight percent aluminum.

3.3 Sample Preparation

A drawing of the infiltration specimen fixture is presented in Figure 3.4. The compact was contained in a 304 stainless steel tube with an inside diameter of 12.7 millimeters (0.5 inch), an outside diameter of 19.1 millimeters (0.75 inch), and a length of 92.0 millimeters (3.625 inches). Sauereisen No. 8 cement was used to coat the inside of the tube walls to prevent reaction with molten aluminum as well as to hold in place a filter at the bottom of the tube.

A vacuum was then pulled through the bottom filter while the silicon carbide was charged slowly with a funnel. While the sample was being charged, the specimen was vibrated to aid in compaction. After all of the silicon carbide had been charged in this manner, a 85 g weight was put on top of the compact while the vacuum was being pulled and the compact was being vibrated simultaneously at varying frequencies.

For tests with just silicon carbide in the compact, 8 grams of silicon carbide would be used, while for tests with the compacts of silicon carbide mixed with aluminum powder 6.325 grams of silicon carbide was used to 2.109 grams of

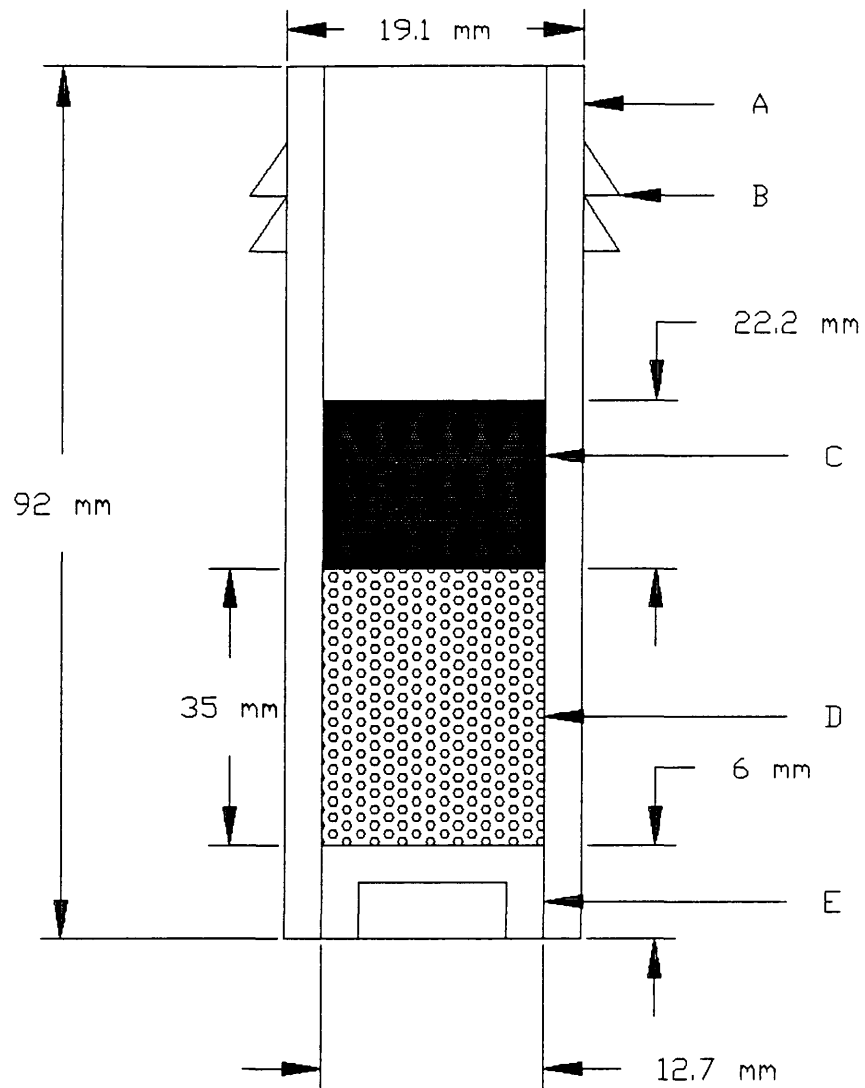


Figure 3.4: Schematic diagram of the infiltration fixture: A) 304 stainless steel seamless tube, B) Brass ferrule compression fitting, C) Aluminum slug D) Silicon carbide compact, E) 15 μm pore diameter stainless steel filter.

aluminum powder. This was equivalent to 25 weight percent of aluminum powder in the compact, and these amounts were used so that the length of the compact would be the same as in the other tests (i.e. 35 millimeters). Finally, a 6,897 kPa (1,000 psi) pressure was applied to the top of the compact and then the 6 g aluminum slug in the same way.

3.4 Reaction Tube Atmosphere

In order to control the environment that the liquid aluminum saw, a re-circulation circuit (see Figure 3.5) was constructed to clean up the argon gas. The first step of the cleaning of the atmosphere was to pull a vacuum of 30 millitorr and backfill with argon three times. The gas was then run through the re-circulation circuit with the aid of a diaphragm pump. The argon would pass through a molecular sieve to eradicate any moisture that might be present, and there was a bubbler for scavenging oxygen that could be put on line if it was deemed necessary. Results showed that the molecular sieve seemed to give satisfactory results, so the bubbler was not used that often for scavenging oxygen.

3.5 Infiltration Tests

A schematic of the infiltration chamber is shown in Figure 3.6. A differential pressure regulator was used to

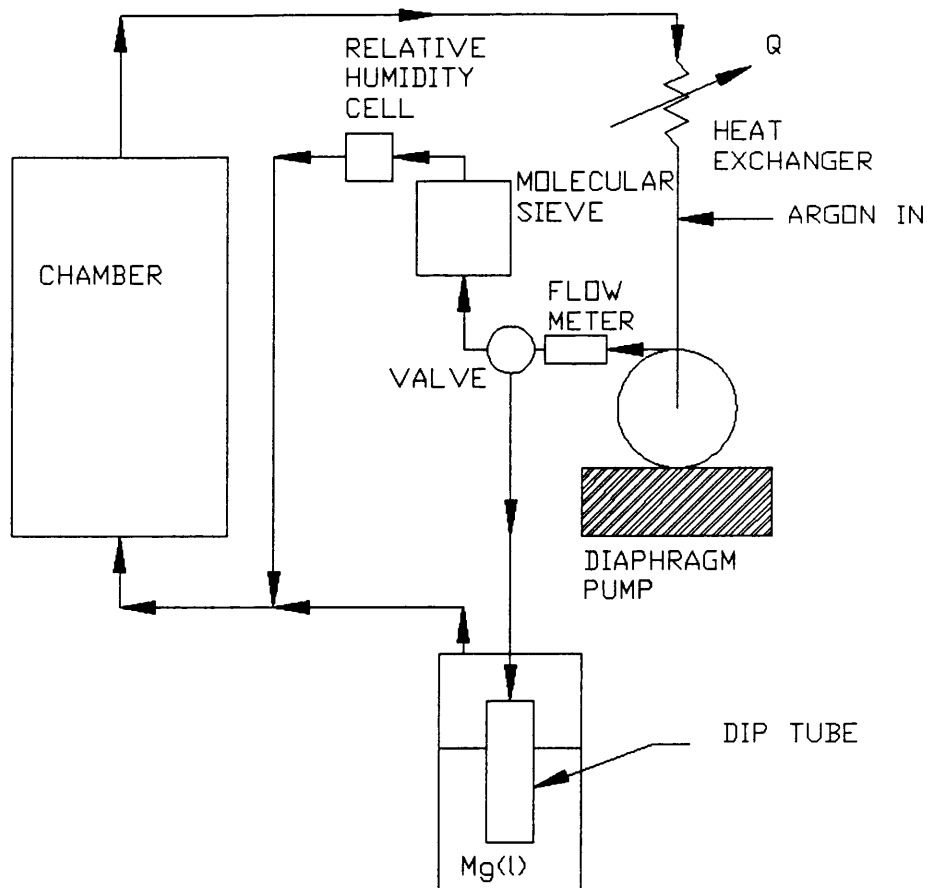


Figure 3.5: Schematic diagram of the re-circulation circuit for cleaning the reaction chamber atmosphere.

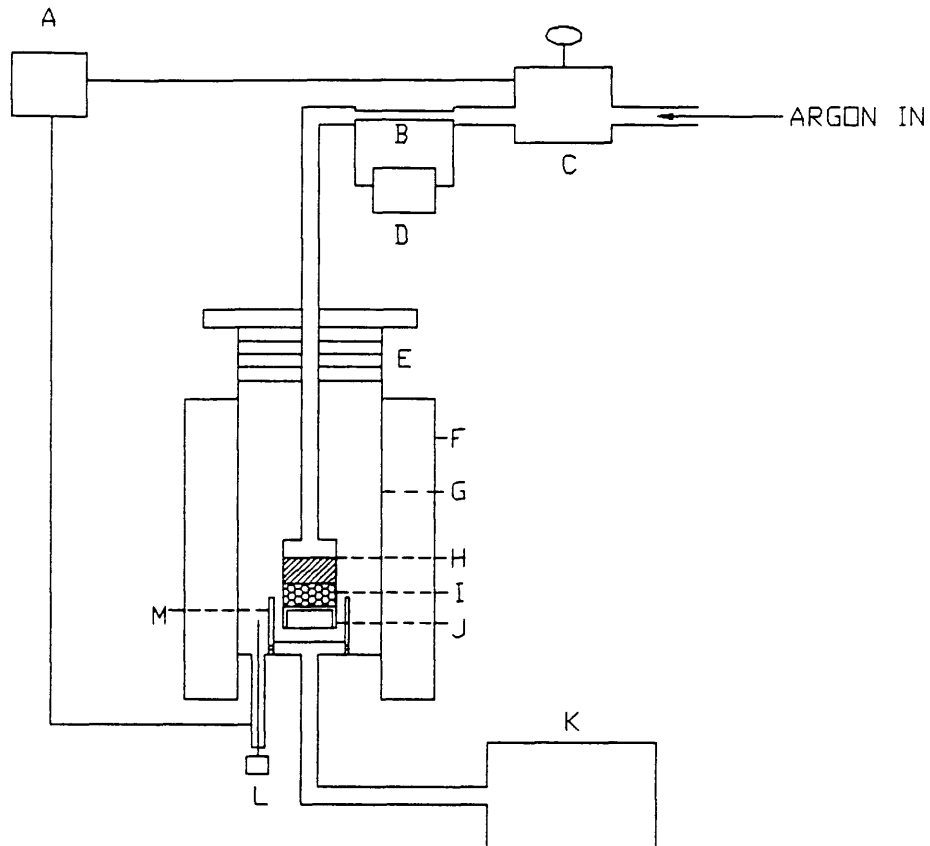


Figure 3.6: Schematic diagram of the infiltration apparatus: A) Differential Pressure Transducer B) Capillary Tube C) Differential Pressure Regulator D) Differential Pressure Transducer E) Cooling Coils F) Furnace G) Reaction Chamber H) Liquid Aluminum I) Silicon Carbide Compact J) Filter K) Vacuum Pump L) Thermocouple M) Collection Crucible

apply the pressure with argon gas, and a differential pressure transducer was hooked up so that it would read the pressure difference between the top of the liquid metal and the chamber that the sample sat in (essentially the pressure that the compact saw since gas could get through the filter at the bottom). This kind of arrangement would allow the total pressure in the chamber to be varied as desired. In these tests a 30 millitorr vacuum was pulled on the chamber during the infiltration.

A small capillary tube was located in the line to the inlet argon supply so that the onset of liquid aluminum flow would be monitored by a differential pressure transducer (DPT) hooked across the capillary tube. The DPT would measure the pressure drop across the capillary tube, and hence, the flow rate (Hagen-Poiseuille relationship). A chart recorder was used to acquire the demodulated output from the DPT, so that in effect, the flow of aluminum through the compact as a function of time could be measured. A typical curve is shown schematically in Figure 3.7, and the beginning and end of infiltration could be read off the plot as indicated. The time for infiltration is the elapsed time between these two events. It should be noted that the infiltration model indicates that the infiltration time varies with the square of the infiltration distance, except

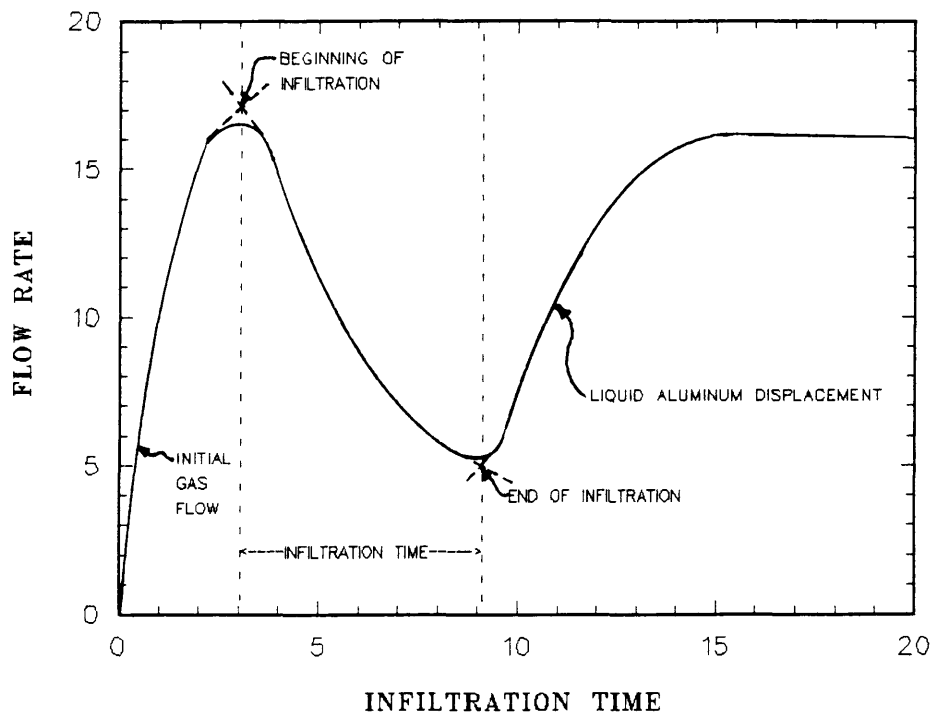


Figure 3.7: Schematic of the flow during infiltration. The transducer hooked across the capillary tube would read the pressure drop, and hence, the flow rate (Hagen-Poiseuille relationship). A chart recorder was also hooked into this transducer so that the change of flow rate as a function of infiltration time could be recorded.

for the beginning of infiltration, and hence, a distance scale might be superimposed on the time scale of Figure 3.7.

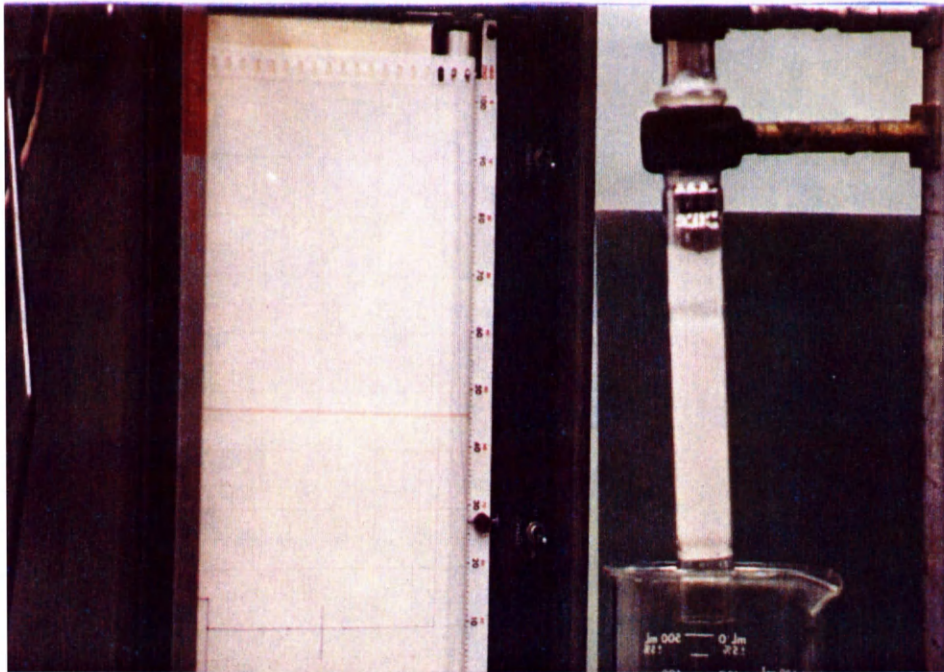
After the reaction tube atmosphere was cleaned as discussed in the previous section, the sample would sit at the desired temperature for one hour to stabilize. Then the desired pressure would be applied, and the infiltration time and flow rate would be recorded on the chart recorder. After the aluminum emerged through the filter and was collected in the collection crucible, the sample would be brought up to the cooling zone and be allowed to solidify. The sample was then cut up for further inspection.

4.0 RESULTS AND DISCUSSION

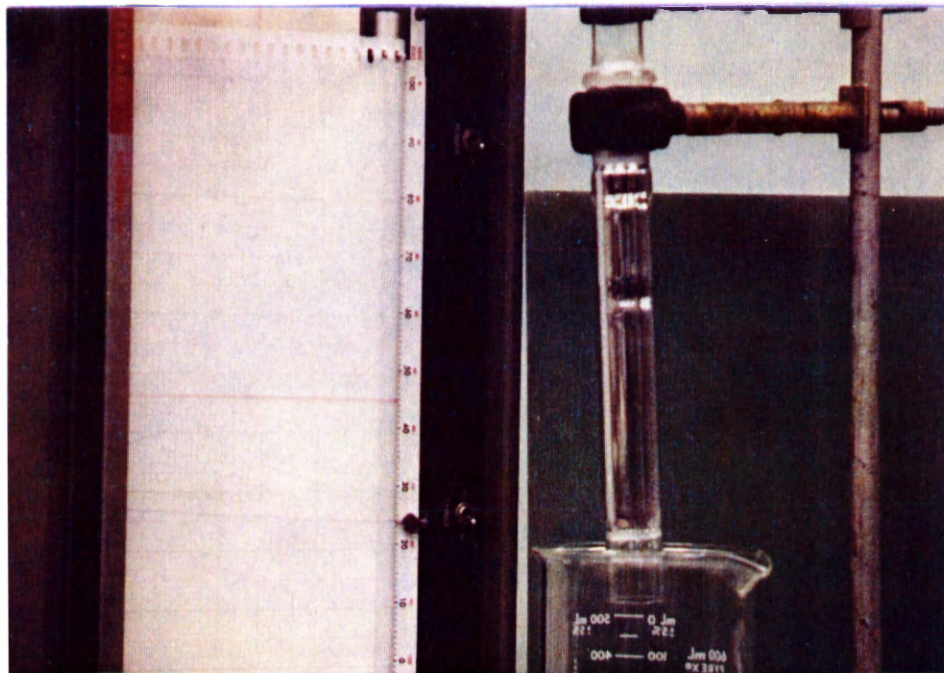
4.1 Infiltration Simulation

To provide for a visualization of the infiltration process, a simulation was conducted using mercury as the infiltrant and glass beads as the particles forming the compact. The purpose of using these materials was to be able to record the process on a video recorder so that the kinetics could be studied. Some still photographs were also taken with a camera, and various stages of the process are shown in Figure 4.1. These photographs confirm that the beginning of infiltration and the end of infiltration correspond to the parts of the curve portrayed in Figure 3.7.

According to the proposed model discussed in section 2.5.2, a linear plot should be obtained ("long time" solution) if the infiltration distance squared is plotted against the infiltration time. The experimental results are shown in Figure 4.2. It can be seen that the plot is linear at large times and is asymptotic to the expected linear behavior at shorter times. Thus, the model appears to characterize the process fairly well in an idealized system.



(a)



(b)

Figure 4.1: Photographs of the various stages of the infiltration of mercury into glass beads.
(a) After infiltration has begun
(b) The end of infiltration

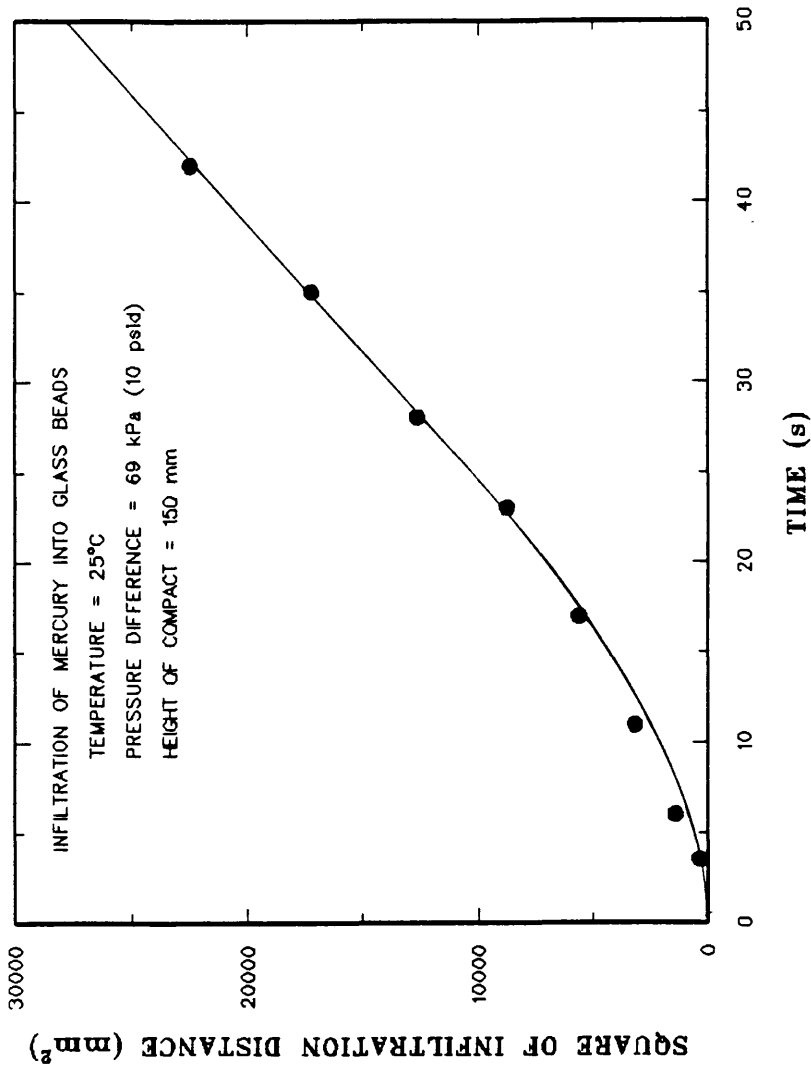


Figure 4.2: Infiltration distance squared as a function of time for the infiltration of mercury into glass beads.

4.2 Body Characterization

To assess the characteristics of the silicon carbide compacts, the pressure drop across each of several silicon carbide compacts and filters was measured over a range of flow rates. The first step of these experiments was to measure pressure drops across filters at known flow rates so that these pressures could be subtracted out in order to obtain the pressure drops across the compacts. The results for two filters are shown in Figure 4.3, and the best fit line of the data from both experiments is:

$$\Delta P(\text{Pa}) = 99,208,894 \text{ Pa m}^{-3} \text{ sec} \times Q(\text{m}^3 \text{ sec}^{-1}) \quad (4.1)$$

where ΔP is the pressure drop and Q is the volume flow rate. The coefficient of correlation for this line is 0.93, which is reasonable; in any case the pressure drop across the filter is small compared to that across the compact, and the small correction is insignificant.

Equation (4.1) can then be used to calculate the pressure drop across the filter for each flow rate used in measuring the pressure drop across the compact and filter.

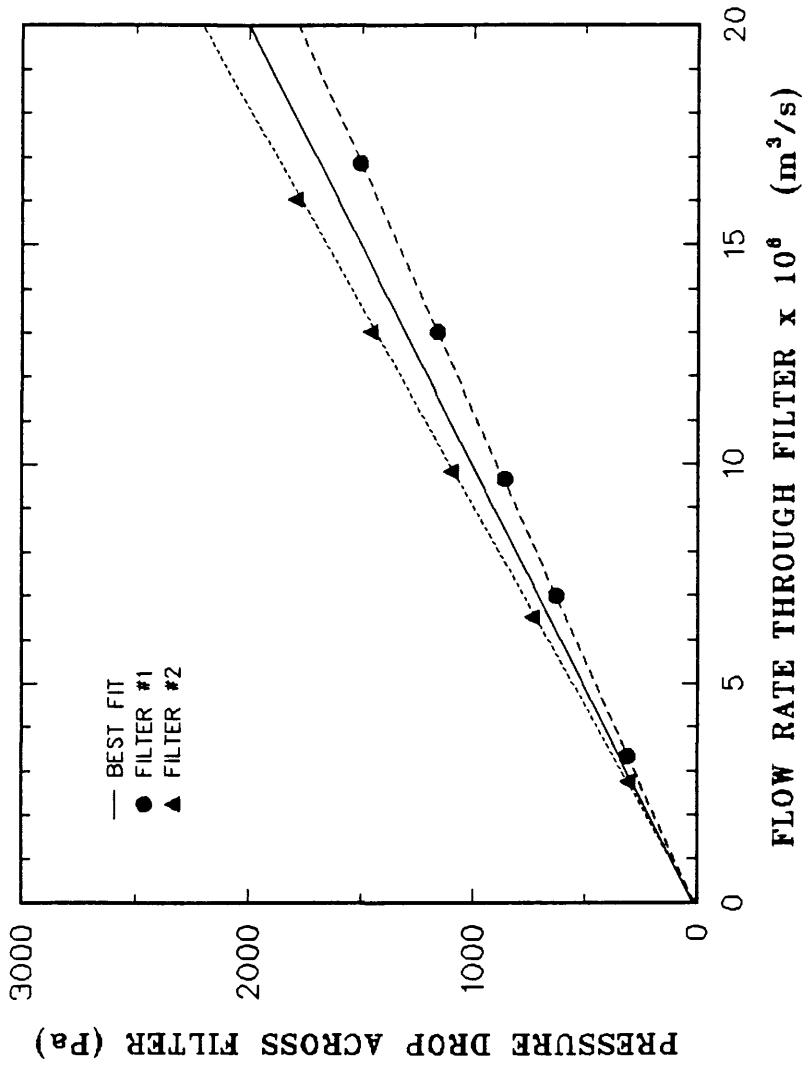


Figure 4.3: Pressure drops across the filters used for the infiltration of aluminum into silicon carbide at known flow rates.

The pressure difference ($P_2 - P_1$), which is the pressure drop across the compact, can then be extracted.

As discussed in section 3.1, a plot of the difference of the square of each of these pressures against the mass flow rate should yield a straight line. The results of these experiments for three different sizes of silicon carbide particulates are shown in Figure 4.4. The linear behavior in Figure 4.4 suggests that there is not much variation in the permeability of compacts of the same type. This consistency is important for the upcoming analysis since variation in permeability in the same type of bed would lead to inconsistent results in the characterization of the infiltration behavior. The effect of just changing the length of the bed can be seen by comparing the compacts for the particulates with an average diameter of 60 microns (particles retained on a 325 mesh screen). The lengths of these compacts are 35 and 72 millimeters, and it can be seen that lengthening the size of the bed increases the pressure drop. Figure 4.4 also shows that reducing the particle size also increases the pressure drop across the compact. The slopes of these lines can then be used to determine the specific permeability of the compacts. Linear regression of these data yields the slopes and coefficients of correlation given in Table 4.1.

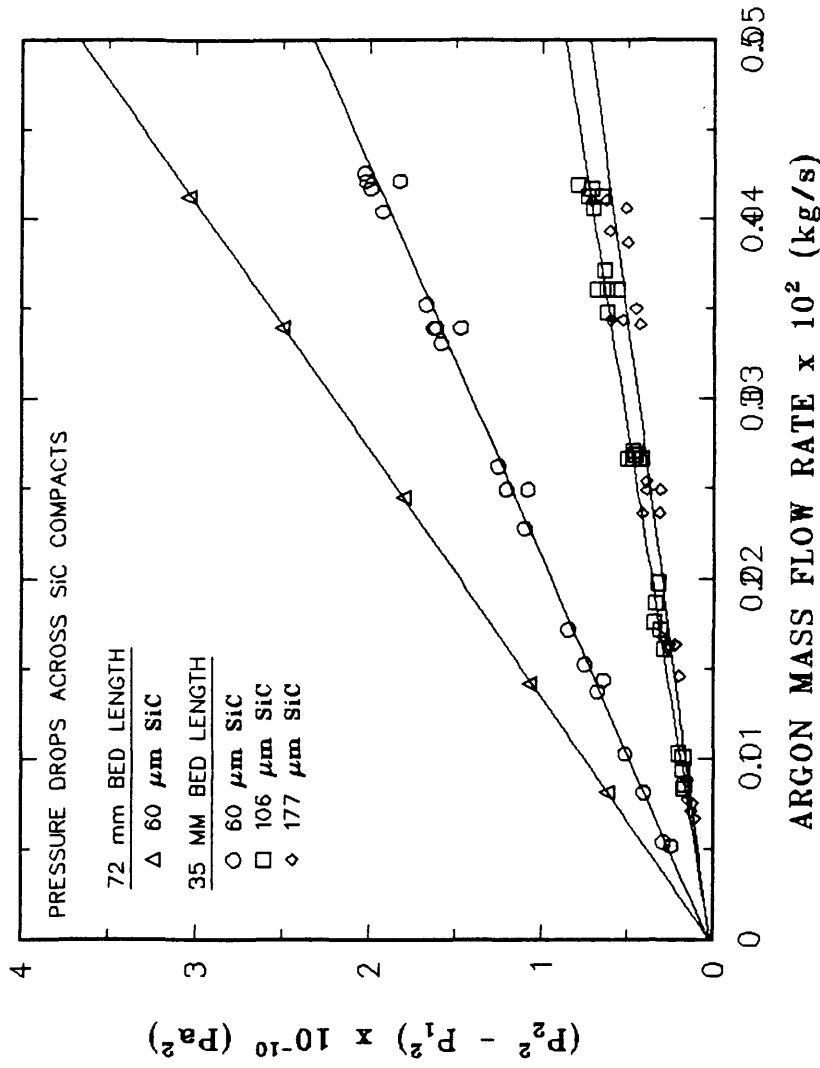


Figure 4.4: Pressure drops across silicon carbide compacts at known flow rates. The slope of this line can be used to calculate the specific permeability.

Table 4.1

Slopes and Correlation Coefficients of Figure 4.4

| Compact Description | Slope (Pa ² kg-1 sec) | Correlation Coefficient |
|---------------------|-------------------------------------|-------------------------|
| 60 μm SiC (72 mm) | 7.3 x 10 ¹¹ | 0.99 |
| 60 μm SiC (35 mm) | 4.6 x 10 ¹¹ | 0.99 |
| 106 μm SiC (35 mm) | 1.7 x 10 ¹¹ | 0.98 |
| 177 μm SiC (35 mm) | 1.4 x 10 ¹¹ | 0.92 |

Since the majority of the data is for 106 μm silicon carbide compacts, the information in Table 4.1 has been used to find the specific permeability as described in section 3.1. The specific permeability of the 106 μm silicon carbide compacts is $4.388 \times 10^{-12} \text{ m}^2$.

The void fractions were found by introducing water in the pores of the compact and measuring the weight of the water needed to fill the pores, as described in section 3.1. The weight of the water could then be equated to the volume, and this could be used to calculate the void fraction. For the 106 μm silicon carbide compacts the void fraction was found to be 0.45, which agrees with the void fraction of 0.43 found by analyzing photomicrographs of the compacts obtained with a scanning electron microscope. Using the specific permeability ($1/K_1$) and the void fraction, equation (2.30) can be used to estimate that the effective particle diameter is about 47 micrometers, which is slightly smaller than the measurements made on the scanning electron microscope. Equation (3.13) can then be used to find the corresponding effective pore radius. The permeability tests give a value of 12.8 micrometers for the effective pore radius, while the scanning electron microscope (SEM) measurements yield a result of 14.5 micrometers.

The above information can then be put into

equation (2.36) as is appropriate, and the threshold pressures (pressure required to overcome the resisting capillarity forces in order to initiate infiltration) can be calculated. The $\gamma_{lv}\cos\theta$ term (surface tension and contact angle) is extrapolated from Figure 2.7, and the density is obtained from Figure 2.2. The initial height of liquid aluminum in the reservoir, h_{R0} , was approximately 22.2 millimeters (7/8 inch). The calculated threshold pressures for pure aluminum at various temperatures are presented in Table 4.2.

An important aspect of preparing the compacts for infiltration was found to be the mechanical packing technique. Uniform particle spacing in the compacts can be difficult to achieve because of the irregular shape of the particles. At first, the compacts were prepared by applying a load to the top of the compacts with a hydraulic press. This technique, however, resulted in non-uniform packing, which led to channeling of the aluminum during infiltration. The most common mode of channeling was down the sides, as shown in Figure 4.5. Further attempts were made to assemble the compacts incrementally in small layers, each layer having a load applied to it with a hydraulic press. Incremental packing resulted in voids delineating the boundaries between each layer, which was also not

Table 4.2

Threshold Pressures for Infiltrating Aluminum through
106 μm Silicon Carbide at Various Temperatures

| Temperature | Threshold Pressure (Permeability Tests) | Threshold Pressure (SEM Analysis) |
|--------------------|--|--------------------------------------|
| $^{\circ}\text{C}$ | kPa | kPa |
| 670 | 106 | 94 |
| 700 | 102 | 90 |
| 730 | 97 | 86 |
| 750 | 95 | 84 |

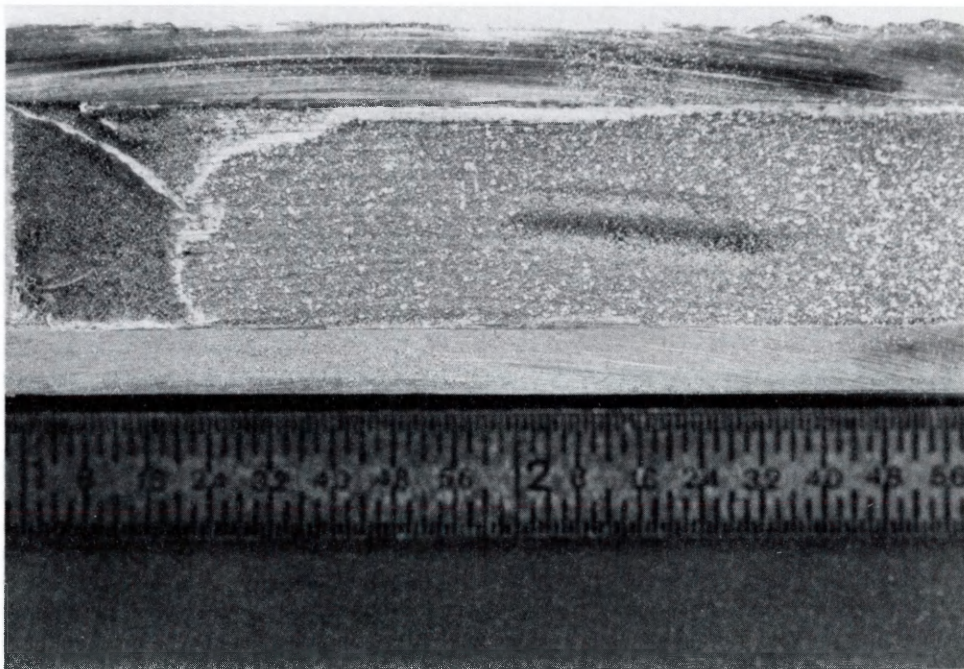


Figure 4.5: Photograph showing the typical channeling pattern of aluminum going down the sides instead of uniformly through the compact.

satisfactory.

Aluminum powder was added to the compact to reduce the reinforcement volume fraction and to investigate this as perhaps being a means for improving the wetting conditions as well as for reducing the amount of channeling. A larger number of successful infiltrations were accomplished with this method, but there was still significant channeling when these compacts were packed with a hydraulic press.

The next stage of experimentation was to investigate the geometry of the compact as related to the channeling phenomenon. These samples were still prepared by packing the compacts with a hydraulic press. The channeling behavior was explained further by investigating the effect of aspect ratio of the compact. Figure 4.6 illustrates the observation that if the length of the cylindrical compact was limited to the same dimension as the diameter, successful infiltrations resulted. This feature was tested further with a compact that had a length just slightly larger than the diameter. Figure 4.7 shows that the infiltration started down the center, but then proceeded uniformly across the compact at approximately the point where the distance to the bottom was about the same as the diameter of the compact. This mechanism was observed several times, suggesting that an aspect ratio of one for

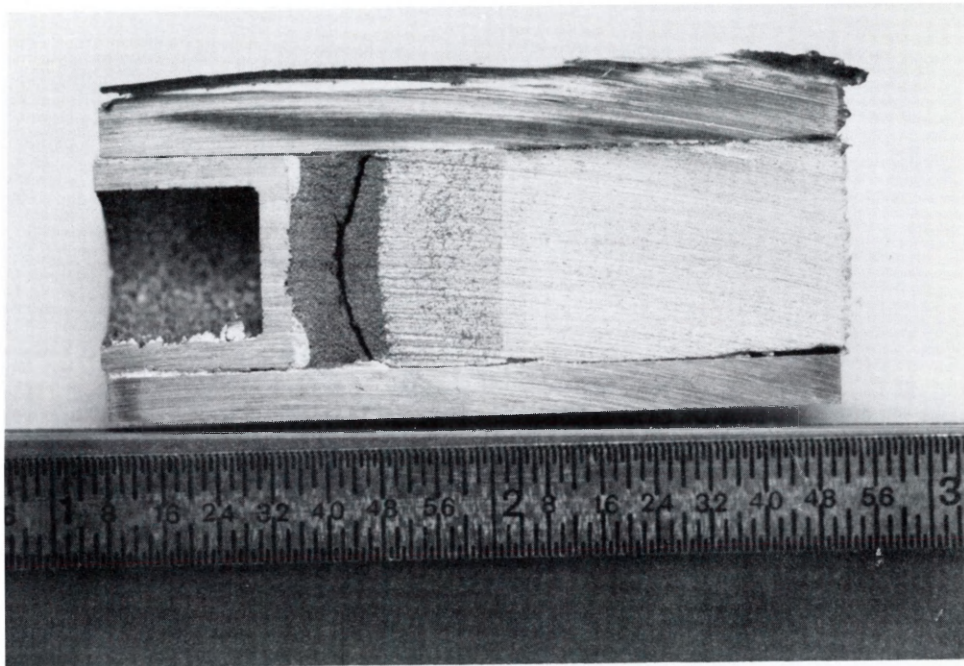


Figure 4.6: Photograph of sample showing successful infiltration of a compact (diameter of 12.7 millimeters or 0.5 inch) when the length of the cylindrical compact is about the same as the diameter.

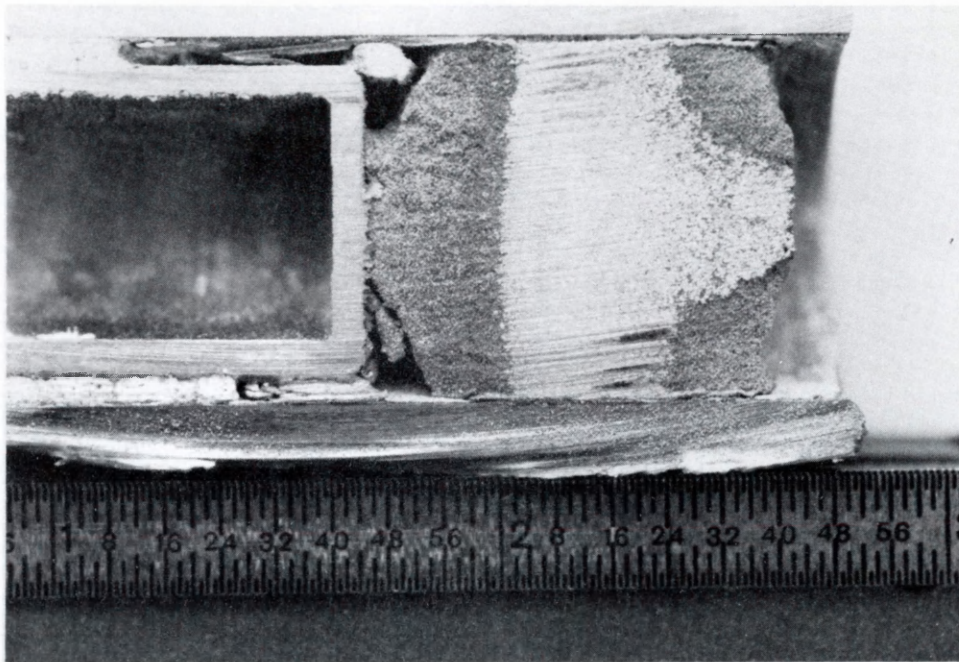


Figure 4.7: Photograph of larger compacts (diameter of 22.2 millimeters or 0.875 inch) illustrating that infiltration becomes uniform at approximately the point where the length left to infiltrate is about the same as the diameter.

the compact provides the uniform internal conditions required for successful infiltration.

Defining an aspect ratio of one for a compact is often impractical, and a more flexible means of obtaining uniform infiltration was sought. Review of the relevant literature (as discussed in section 2.4) indicated that vibrational packing of compacts has been successful in achieving uniform packing, and this proved to be the case for the compacts prepared in this work. Uniform packing of the silicon carbide compacts was ultimately obtained by pulling a vacuum through the bottom filter and vibrating the sample container while charging it with the silicon carbide particles. The sample was then subjected to further by vibration and suction with an 85 g weight located on the free surface. During this step, the frequency of vibration was varied so it would have an influence on the packing behavior of the various sizes of particles, as suggested by the literature reviewed in section 2.4. The final step was to apply a 6,896 kPa (1,000 psi) pressure to the top of the compact followed by pressing the aluminum slug into the infiltration fixture and on top the silicon carbide under the same pressure. Figure 4.8 shows a successful infiltration of a compact prepared by using the method just described.

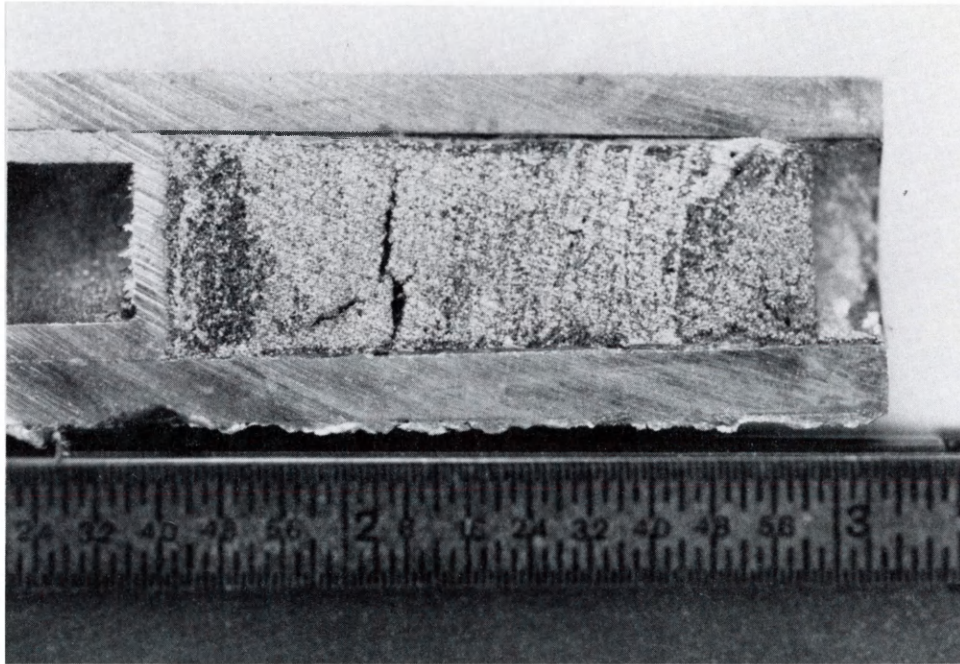


Figure 4.8: Successful infiltration after silicon carbide compact has been packed using the vibration method.

4.3 Infiltration Experiments

The flow of aluminum through the compact as a function of time was determined with the aid of the pressure response trace obtained on a chart recorder as described in section 3.5. This allowed for a precise measurement of infiltration time, in particular when the change in slope (from the aluminum front moving through the compact to the transition of the back end of the slug emerging through the filter) was sharp.

This method of determining the infiltration time proved to be tractable since the infiltration rate was quite rapid under certain conditions. Above 750°C, the infiltration time was so short that this then delineated the maximum temperature that could be tested. The lower limit of temperature was chosen to be 670°C since this was considered to be sufficiently above the melting point of aluminum of 660°C. The upper limit of pressure of 207 kPa (30 psid) was chosen because it is the highest pressure that the differential pressure regulator employed allowed. A lower limit of 103 kPa (15 psid) was utilized since it approaches the threshold pressures. In fact, it was observed that no infiltration occurred at applied pressures of 69 kPa (10 psid) for the trials run with 106 μm silicon carbide. This suggests that the calculated threshold pressures (106 to 95

kPa for 670 to 750°C, respectively, from the permeability test data and 94 to 84 kPa for 670 to 750°C, respectively, from the SEM analysis data) are reasonable, even though successful infiltrations were accomplished at an applied differential pressure of 103 kPa (15 psid). With these limits set, the temperature and pressure dependence of the process was then investigated.

Before the specific dependencies are discussed, the final results of the model will be reviewed. Now that a specific analysis is being performed, the subscript "I" will be used to denote the time required to complete infiltration. If the height of the compact (approximately 35 millimeters for all of the tests) is taken as the reference height, $\langle h \rangle$, then it can be seen from equation (2.38) that the dimensionless height ξ , will be equal to one. If this result is substituted into equation (2.42), then it can be seen that:

$$\tau_I = \frac{\lambda_1}{2} \quad (4.2)$$

where again τ_I is dimensionless time for complete infiltration and the expression for λ_1 will be given on the left hand side in equation (4.4). Reverting to

dimensional quantities as by equation (2.39), the result is:

$$\tau_I = \frac{\lambda_1}{2} = \left[\frac{1}{\langle h \rangle} \left(\frac{P_{eff}}{\rho} \right)^{1/2} \right] t_I \quad (4.3)$$

where P_{eff} is the effective pressure as described by equation (2.36), ρ is the density, and t_I is the time for complete infiltration. Substituting for λ_1 from equation (2.40) then yields:

$$\frac{1}{2} \frac{K_1 \eta \langle h \rangle}{(\rho P_{eff})^{1/2}} = \frac{\lambda_1}{2} = \left[\frac{1}{\langle h \rangle} \left(\frac{P_{eff}}{\rho} \right)^{1/2} \right] t_I \quad (4.4)$$

where K_1 is as described in equation (2.30) and η is the viscosity of aluminum. Simplifying, and solving for t_I :

$$t_I = \frac{K_1 \eta (\langle h \rangle)^2}{2 (P_{eff})} \quad (4.5)$$

This equation is the general result that will be used in the upcoming discussions.

4.3.1 Temperature Dependence.

With the aid of equation (4.5), the temperature dependence of the system will be analyzed. In the temperature analysis, the pressure will be held constant, while the temperature is varied. The terms affected by temperature are the effective pressure, P_{eff} , and the viscosity, η . It can be seen from equation (50) that the

temperature dependent terms affecting the effective pressure are the wettability term, $\gamma_{lv}\cos\theta$, and the density. Furthermore, it can be seen from Figures (2.2), (2.4), and (2.7) that these terms are relatively temperature insensitive in comparison to the viscosity, for the temperature range of interest (670 to 750°C). Thus, the effective pressure will be considered to be invariant relative to changes in temperature. Recasting equation (4.5) with these constraints yields:

$$t_I = c \eta(T) \quad (4.6)$$

where:

$$c = \frac{K_1(\langle h \rangle)^2}{2P_{eff}} \quad (4.7)$$

and, $\eta(T)$ is as described by equation (2.4). The result is then:

$$\eta(T) = A \exp\left(\frac{E_{vis}}{RT}\right) \quad (4.8)$$

where A is a constant, R is the gas constant, E_{vis} is the activation energy of viscosity, and T is the absolute temperature. Substituting this value of the viscosity into equation (4.6) yields:

$$t_I = cA \exp\left(\frac{E_{vis}}{RT}\right) \quad (4.9)$$

From this relationship, it can be seen that a plot of the

logarithm of infiltration time versus the inverse of the absolute temperature should yield a slope which is equivalent to $E_{vis}/(2.303R)$.

The results of the infiltration of aluminum into 106 μm silicon carbide, with the corresponding activation energies of viscosity, are shown in Figure 4.9. These activation energies of viscosity are in agreement with the range of activation energies of viscosity for aluminum (3.3 to 5.0 kcal/mole or 13.8 to 21.0 kJ/mole) reported in the reference reviewed in the literature (41), suggesting that the viscosity is responsible for the dominant temperature behavior displayed by this system. The results of the infiltration of aluminum into 177 μm silicon carbide are presented in Figure 4.10. These activation energies of viscosity, although they are somewhat high also agree reasonably well with the activation energies of viscosity reported in the literature. A comparison of the 106 and 177 μm silicon carbide particle data is illustrated in Figure 4.11. It is seen that the slopes of the lines associated with 177 μm silicon carbide data are slightly higher than those for the 106 μm silicon carbide data. In viscous controlled flow, the viscous effects dampen the turbulent eddies that are present. A change in the turbulent flow

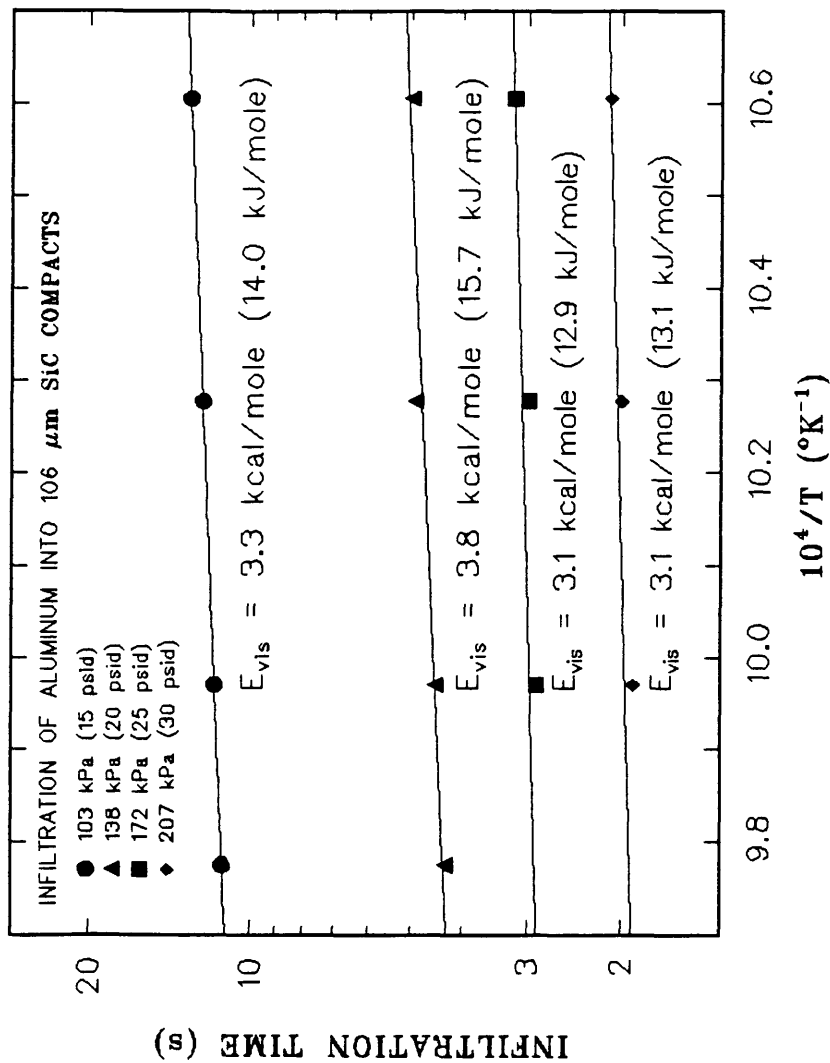


Figure 4.9: The temperature dependence of infiltrating aluminum into 106 μm silicon carbide compacts.

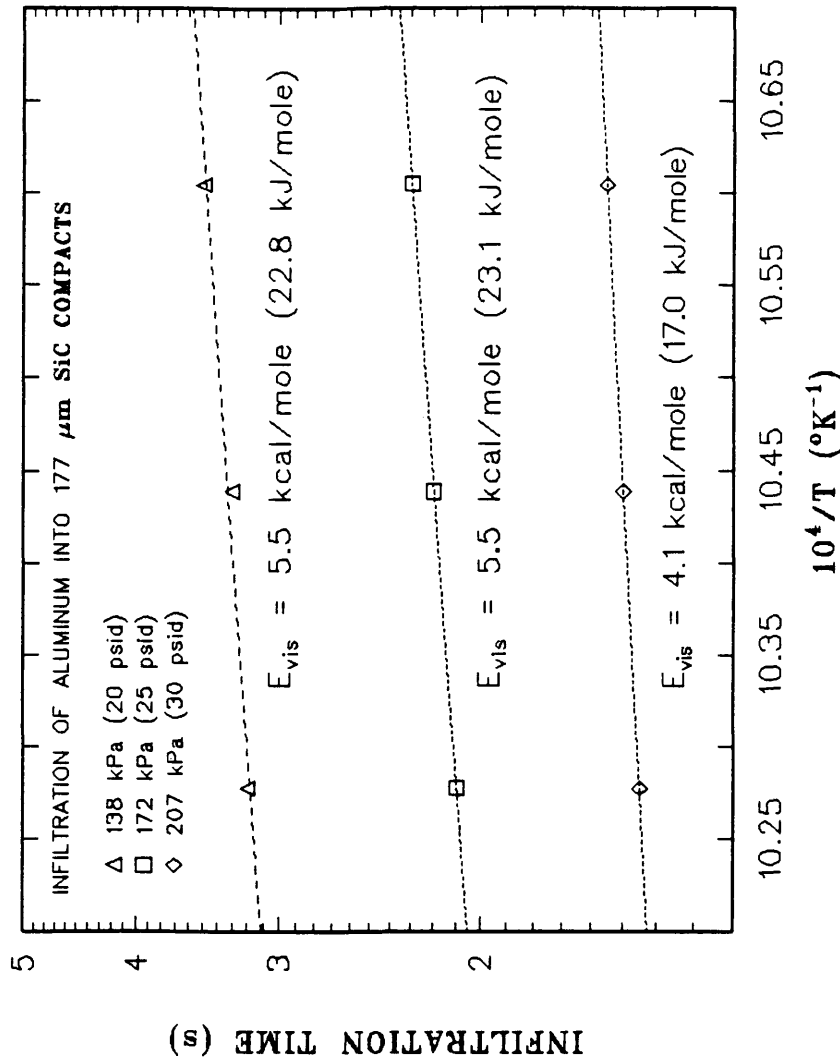


Figure 4.10: The temperature dependence of infiltrating aluminum into 177 μm silicon carbide compacts.

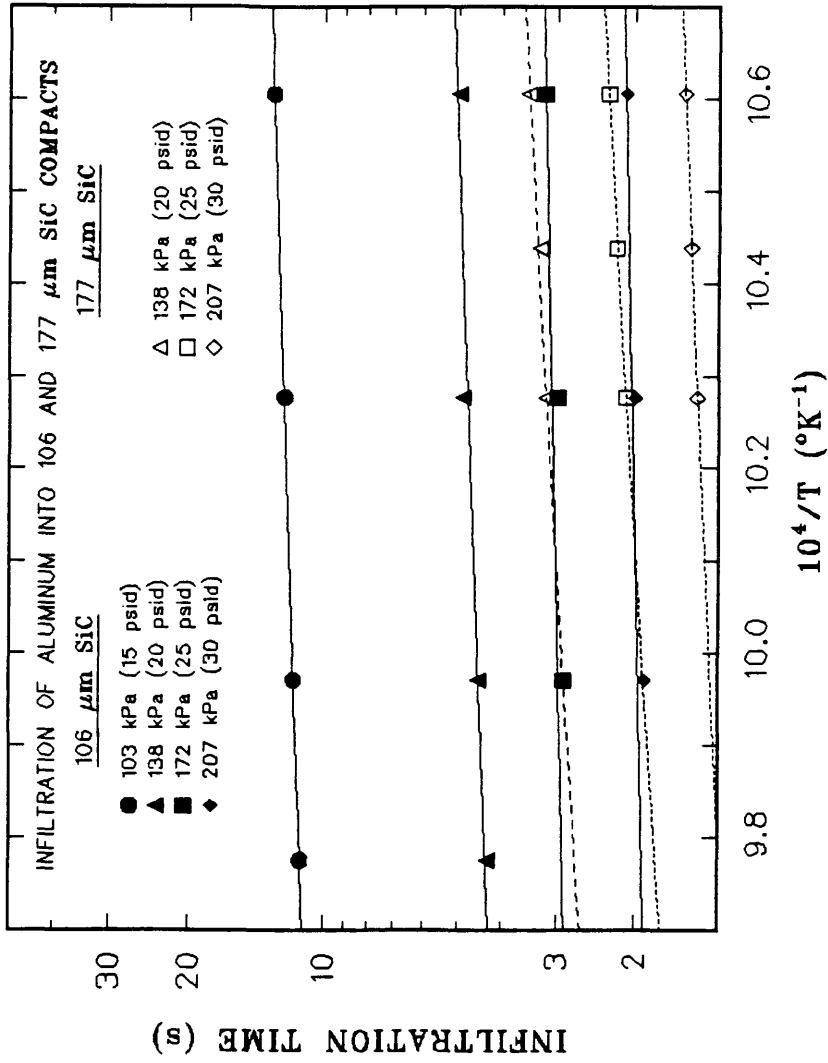


Figure 4.11: Comparison between the temperature dependencies of infiltrating aluminum into 106 and 177 μm silicon carbide compacts.

pattern, as manifested by particles of varying size, could affect the apparent viscosity, possibly explaining the difference in the activation energies of viscosity for the 106 and 177 μm silicon carbide data. The linearity of both plots indicates that the proposed model is a possible mechanism for the process. It should also be noted that the 177 μm silicon carbide compacts were infiltrated in a shorter time than the 106 μm silicon carbide compacts. This is to be expected since the 177 μm silicon carbide compacts have larger voids, and hence a higher permeability, causing them to be infiltrated more rapidly.

Another series of experiments consisted of mixing aluminum powder with the 106 μm silicon carbide particles, producing a compact that was subsequently infiltrated. Examination of Figure 4.12 shows that the compacts with aluminum powder were infiltrated at a higher rate in most cases; however, the data do not exhibit a linear behavior. This lack of linearity is not surprising since the proposed model only accounts for the displacement of a gas from the pores by the liquid aluminum, while in the case of the powder mixed in with the silicon carbide, liquid aluminum in the pores is also partially displaced by the aluminum from the reservoir.

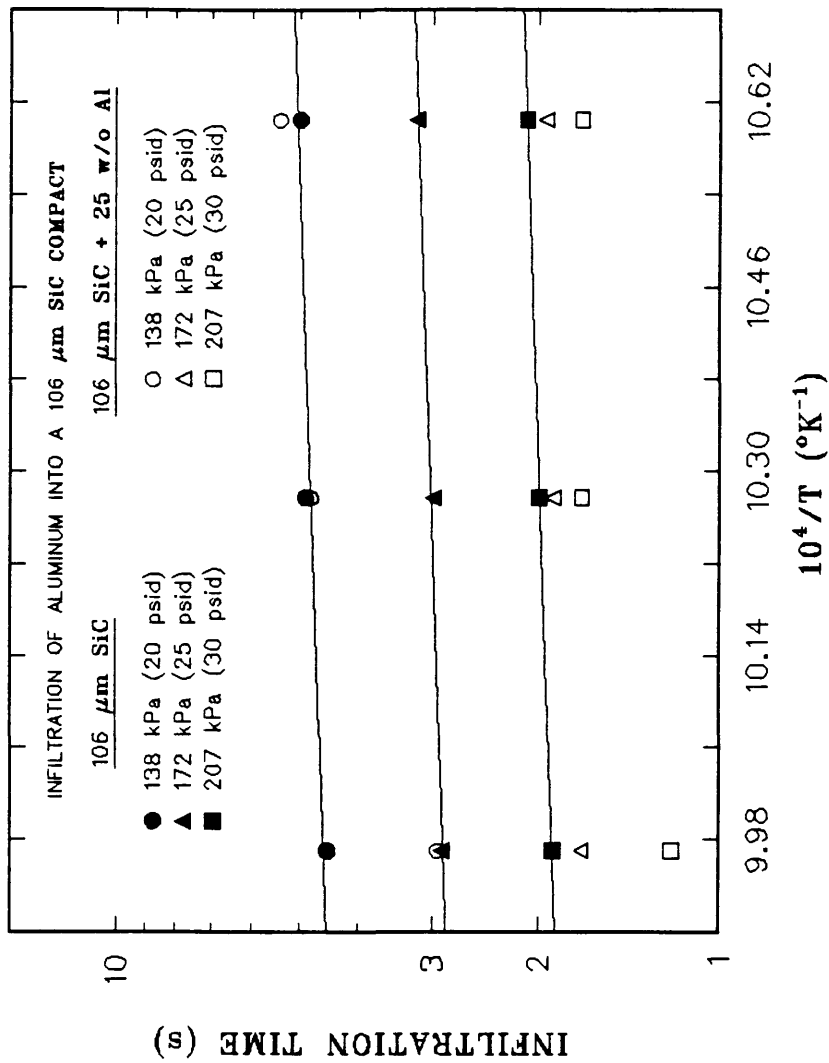


Figure 4.12: A comparison of the temperature dependencies of infiltrating aluminum into 106 μm silicon carbide compacts and 106 μm silicon carbide mixed with aluminum powder.

4.3.2 Pressure Dependence.

The pressure dependence is analyzed by considering isothermal behavior. Since P_{eff} is the term that is responsible for the effect of pressure on the time for complete infiltration, equation (4.5) will be recast to yield a linear equation for this quantity. Thus, insertion of this term into equation (4.5) results in the following equation:

$$\frac{1}{t_I} = \frac{2P_{eff}}{K_1\eta(\langle h \rangle)^2} \quad (4.10)$$

Substituting for P_{eff} from equation (2.36):

$$\frac{1}{t_I} = \frac{2(P^* + \frac{2\gamma_{lv}\cos\theta}{r_h} + \rho gh_{r_0})}{K_1\eta(\langle h \rangle)^2} \quad (4.11)$$

where P^* is the applied differential pressure, ΔP ; γ_{lv} is the liquid-vapor surface tension; θ is the contact angle; r_h is the effective pore radius; and h_{r_0} is the initial height of the liquid aluminum in the reservoir.

Recasting this in a more compact form results in:

$$\frac{1}{t_I} = C_o(\Delta P + C_1) \quad (4.12)$$

where:

$$C_o = \frac{2}{K_1 \eta (\langle h \rangle)^2} \quad (4.13)$$

and:

$$C_1 = \frac{2\gamma_{lv} \cos \theta}{r_h} + \rho g h_{ro} \quad (4.14)$$

Equation (4.12) indicates that a plot of the inverse of the infiltration time versus the applied differential pressure should result in linear behavior. Figure 4.13 shows the results for the 106 and 177 μm silicon carbide data, which confirms this expectation. Equation (4.12) also indicates that as the temperature is increased, the slope, C_o , of each line corresponding to a given temperature should increase; because the viscosity, η , which is in the denominator of this term decreases with increasing temperature. Table 4.3 lists the values for the slopes and intercepts of these lines. The slopes do increase as expected, with the exception of the 750°C, 106 μm silicon carbide data; but this particular set of data is only comprised of two data points which detracts from its reliability. It should be noted that all of the lines had a correlation coefficient of 0.99 or better, indicating a high

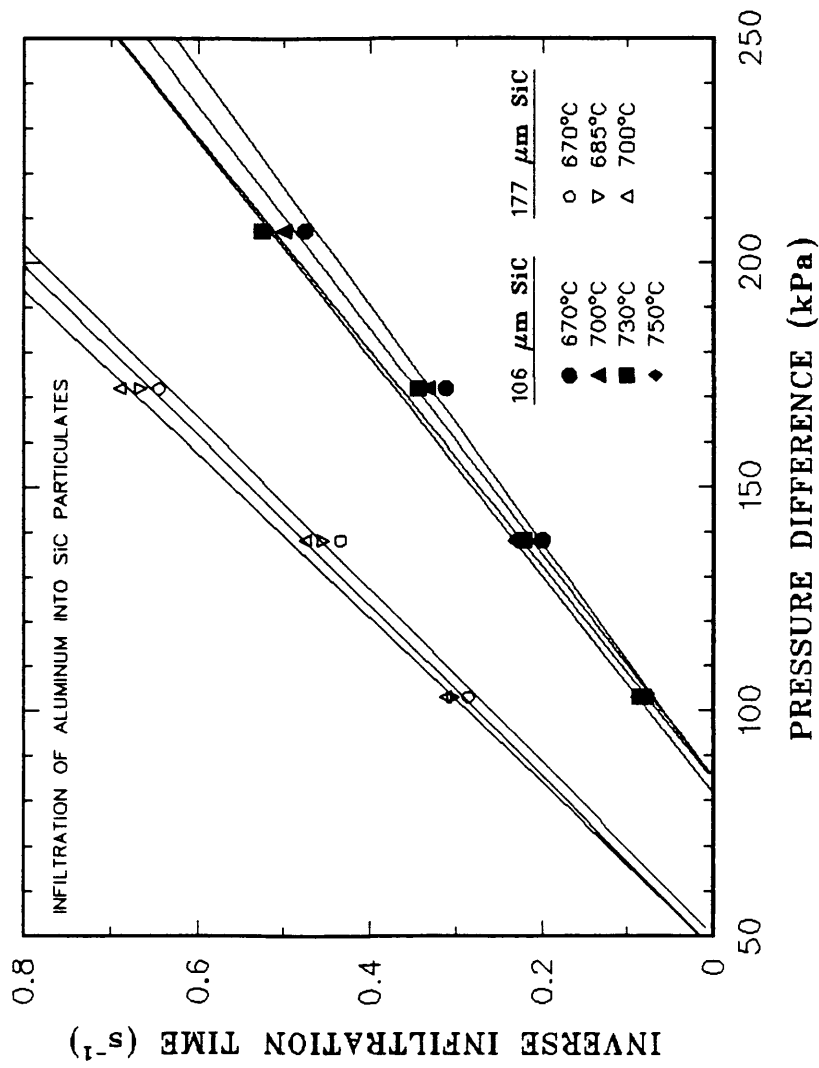


Figure 4.13: A comparison of the pressure dependencies between the infiltration of aluminum into 106 and 177 μm silicon carbide compacts.

Table 4.3

Slopes and Intercepts of the Lines Showing the Pressure Dependencies of Infiltrating Aluminum into 106 and 177 μm Silicon Carbide Compacts

| Line Description | Slope (C_0) ($\text{Pa}^{-1} \text{s}^{-1}$) | Intercept ($C_0 C_1$) (s^{-1}) |
|-------------------------------|---|--|
| 670°C (106 μm SiC) | 3.788×10^{-6} | -0.3207 |
| 700°C (106 μm SiC) | 4.004×10^{-6} | -0.3410 |
| 730°C (106 μm SiC) | 4.178×10^{-6} | -0.3528 |
| 750°C (106 μm SiC) | 4.116×10^{-6} | -0.3355 |
| 670°C (177 μm SiC) | 5.205×10^{-6} | -0.2613 |
| 700°C (177 μm SiC) | 5.266×10^{-6} | -0.2501 |
| 730°C (177 μm SiC) | 5.462×10^{-6} | -0.2592 |

degree of correlation for the linear behavior.

A similar comparison can be made between the data for aluminum infiltrating a pure 106 μm silicon carbide compact and a bed comprised of a mixture of silicon carbide and aluminum powders. Figure 4.14 is the comparison between these two sets of data. Again the bed that has the aluminum powder mixed in with the silicon carbide does not show the linear behavior predicted by the model.

4.3.3 Overall Dependence.

The above results can now be used in combination with equation (4.5) to provide a general equation for the infiltration of aluminum into 106 μm silicon carbide particles. The permeability tests allowed K_1 to be measured and it was found to be equal to $2.279 \times 10^{11} \text{ m}^{-2}$. Also, the reference height, $\langle h \rangle$, has been chosen to be the length of the compact, which is 0.035 m. The viscosity analysis given above yields an average value for the activation energy of viscosity of 13.9 kJ/mole, with a standard deviation of 1.1 kJ/mole, for the infiltration of aluminum into 106 μm silicon carbide. Using this result for the activation energy of viscosity, and the known values for the other terms in equation (54), an average value of $2.551 \times 10^{-4} \text{ kg m}^{-1} \text{ s}^{-1}$, with a standard deviation of $2.69 \times 10^{-5} \text{ kg m}^{-1} \text{ s}^{-1}$,

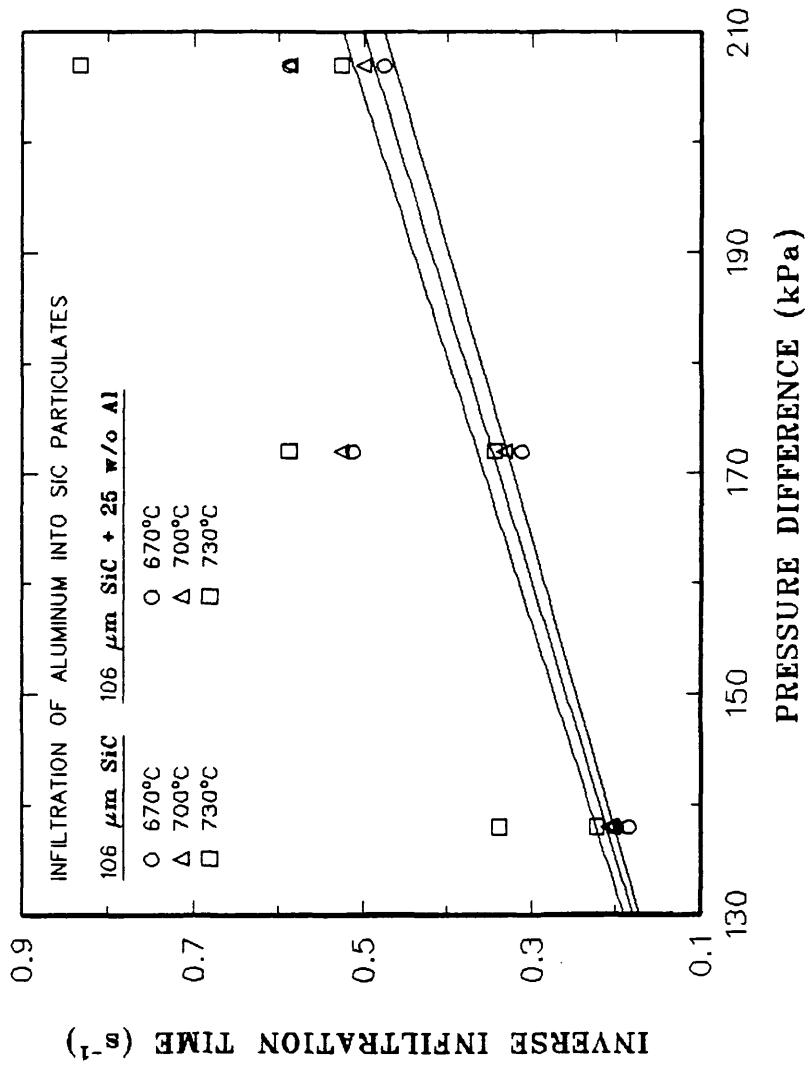


Figure 4.14: A comparison of the pressure dependencies between the infiltration of aluminum into a 106 μm silicon carbide compact and a bed consisting of 106 μm silicon carbide mixed with aluminum powder.

has been found for the pre-exponential factor, A. The effective pressure is the difference between the applied differential pressure minus the appropriate threshold pressure for the temperature being considered. Substituting these values into equation (4.5) and rearranging the equation in the form of an average rate yields:

$$\frac{\langle h \rangle}{t_I} = \frac{3.44 \times 10^{-8} \text{ kg}^{-1} \text{ m}^3 \text{ s} (\Delta P - P_{th})}{\langle h \rangle \times \exp\left(\frac{-13,900 \text{ J/mole}}{RT}\right)} \quad (4.15)$$

where t_I is the time for complete infiltration in seconds; ΔP is the applied differential pressure in pascals; P_{th} is the threshold pressure in pascals, as defined in section 2.5.2 (values for P_{th} are given for some temperatures in Table 4.2; $\langle h \rangle$ is a reference height in meters, which is conveniently designated as the height of the compact; R is the gas constant in $\text{J mole}^{-1} \text{ }^\circ\text{K}^{-1}$; and T is the absolute temperature in $^\circ\text{K}$. This equation was developed for the temperature range of 670 to 750°C.

4.4 Microstructural Examination of Composites

The microstructural evaluation was conducted with the aid of the scanning electron microscope used to evaluate the particles in section 3.2. Examination of Figure 4.15 shows

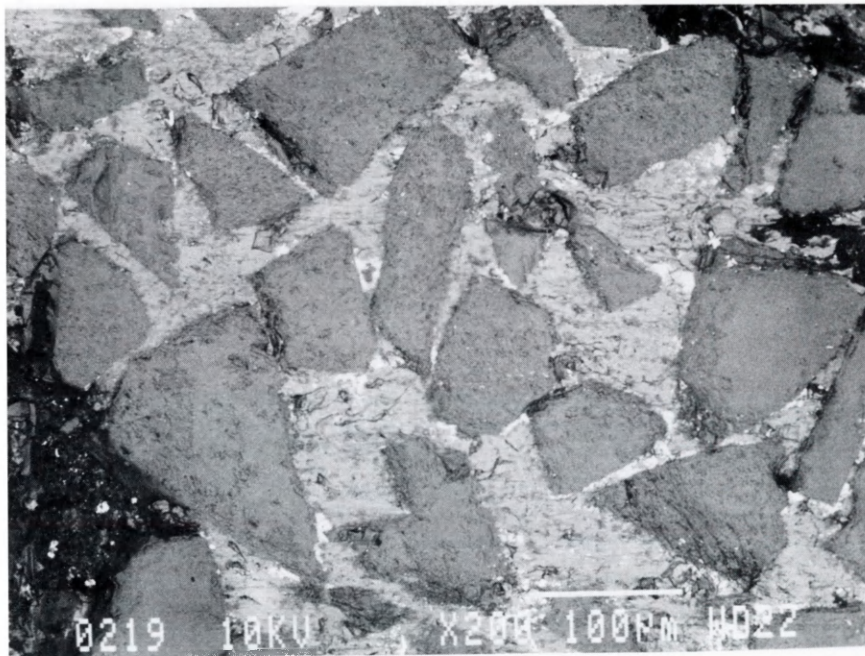


Figure 4.15: SEM photomicrograph showing $106\ \mu\text{m}$ silicon carbide dispersed in an aluminum matrix. The original compact consisted of plain $106\ \mu\text{m}$ silicon carbide particles. (200X)

that the 106 μm silicon carbide particulates are dispersed fairly well in the aluminum, but that there was also porosity present. These particles were present in the composite at a volume fraction of approximately 0.57. Figure 4.16 shows a composite comprised of 177 μm silicon carbide, which also exhibits porosity. The 177 μm silicon carbide composites are present at a volume fraction of about 0.54.

Mixing of aluminum powder with the silicon carbide to form a compact tends to provide for a greater dispersion of the particulates, resulting in a smaller volume fraction of particles of about 0.35 in the compact comprising of 25 weight percent aluminum powder. This is evident from Figure 4.17. An even smaller volume fraction of particles of about 0.31 resulted in the bed consisting of 50 weight percent powder, as can be seen in Figure 4.18. The fact that the aluminum powder enhanced the infiltration and provides for a better microstructure makes this method of fabrication worthwhile for further investigation. The infiltration behavior of this configuration, however, has not been modeled in this work, and further research will be necessary to take into account the displacement of the melted aluminum powder within the pores.

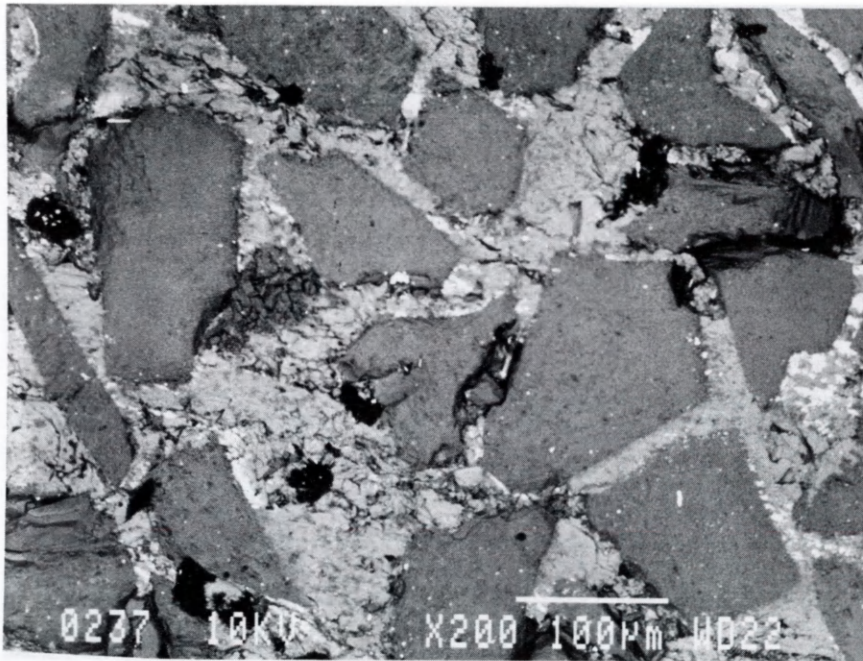


Figure 4.16: SEM photomicrograph showing 177 μm silicon carbide dispersed in an aluminum matrix. The original compact consisted of plain 177 μm silicon carbide particles. (200X)

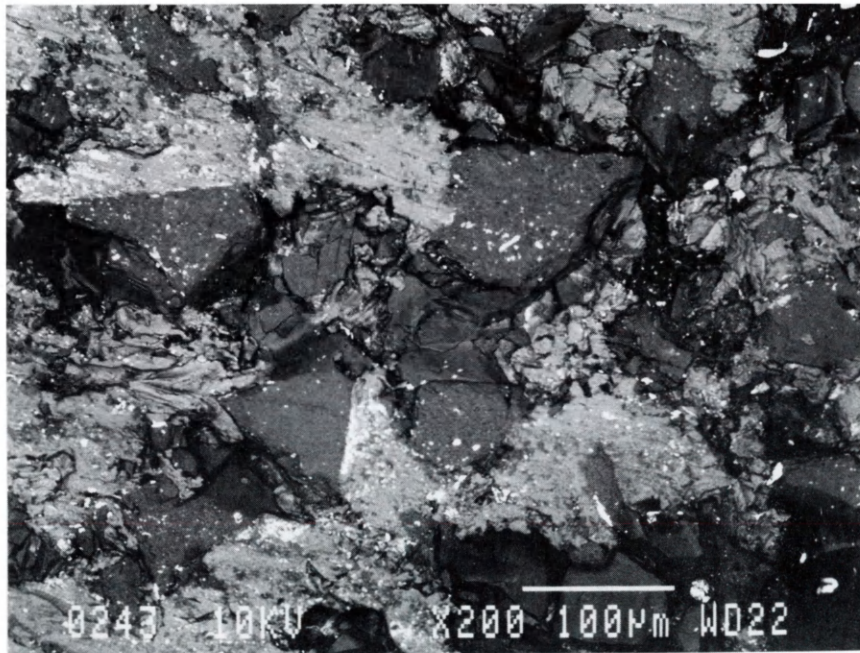


Figure 4.17: SEM photomicrograph showing 106 μm silicon carbide dispersed in an aluminum matrix. The initial compact was comprised of a mixture 106 μm silicon carbide particles and 25 weight percent aluminum powder. (200X)

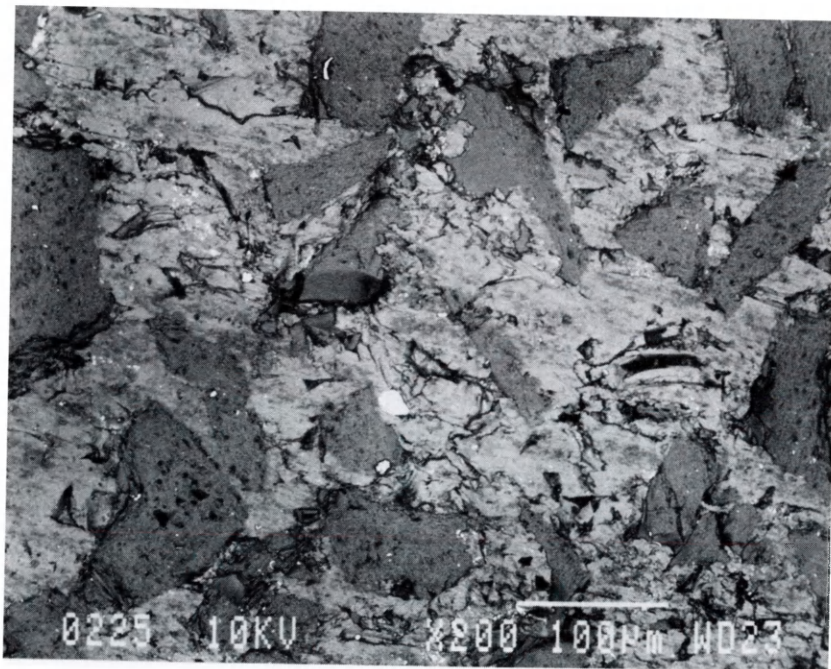


Figure 4.18: SEM photomicrograph showing $106\ \mu\text{m}$ silicon carbide dispersed in an aluminum matrix. The original compact was comprised of $106\ \mu\text{m}$ silicon carbide and 50 weight percent of aluminum powder. (200X)

5.0 CONCLUSIONS

- 1.) Measuring the flow rate of argon, which was used for the infiltration of the aluminum into the compact, as a function of time, can be used to determine the time required for infiltration.
- 2.) The simulation results from infiltrating mercury in a glass column confirm that the square of the infiltration distance varies with the infiltration time linearly, in accordance with the proposed model.
- 3.) Vibration techniques yield the most consistent type of packing. This was confirmed from permeability tests, which showed that the pressure drop/flow rate behavior of compacts of the same type were consistent with each other.
- 4.) The threshold pressure, the minimum pressure required for infiltration, was found to be weakly temperature dependent. The threshold pressures were found to be 106 kPa at 670°C and 95 kPa at 750°C using permeability test results, and they were established to be 94 kPa at 670°C and 84 kPa at 750°C using results from a scanning electron microscope analysis.
- 5.) The temperature dependence of the system correlates with the activation energy of viscosity for aluminum. An

average value of 13.9 kJ/mole was determined for this system.

- 6.) A phenomenological equation can be written for the infiltration of molten aluminum into 106 μm silicon carbide:

$$\frac{\langle h \rangle}{t_I} = \frac{3.44 \times 10^{-8} \text{ kg}^{-1} \text{ m}^3 \text{ s} (\Delta P - P_{th})}{\langle h \rangle} \exp\left(\frac{(-13,900 \text{ J/mole})}{RT}\right)$$

where: t_I is the infiltration time in seconds;

ΔP is the applied pressure in pascals; P_{th}

is the threshold pressure in pascals; and $\langle h \rangle$ is

a reference height, conveniently the height of the compact, in meters.

- 7.) The addition of aluminum powder to the silicon carbide compacts enhances the infiltration, and also provides a method for adjusting the volume fraction of reinforcement.

6.0 FUTURE RECOMMENDATIONS

It was found that measuring the flow of argon used to inject the aluminum into the compact could be used to determine the beginning and end of infiltration. It is recommended that this be studied further to see if it can be applied to more complex geometries.

Addition of aluminum powder to the compact appears to enhance infiltration and provide a way for adjusting the volume fraction of particles. It is suggested that more work be done to characterize the effects of aluminum powder. A model should also be developed that accounts for the displacement of aluminum from the pores located ahead of the infiltration front.

T-3957

REFERENCES

1. Flinn, R.A., Trojan, P.K., Engineering Materials and Their Applications, 2nd. Ed.; Houghton Mifflin Company, Boston, pp.433-481 (1981).
2. Erich, D.L., "Metal-Matrix Composites: Problems, Applications, and Potential in the P/M Industry", The International Journal of Powder Metallurgy; 23 (1), pp.45-54 (1987).
3. Flom, Y. and Arsenault, R.J., "Deformation of SiC/Al Composites", Journal of Metals; July, pp.31-34 (1986).
4. Lloyd, D.J., "Metal Matrix Composites - An Overview", Proceedings of the International Symposium on Advanced Structural Materials, Pergamon Press, New York, August 28-31, pp.1-21 (1988).
5. Taya, M. and Arsenault, R.J., Metal Matrix Composites: Thermomechanical Behavior; Pergamon Press, New York, pp.1-8 (1989).
6. Nardone, V.C. and Prewo, K.M., "On the Strength of Discontinuous Silicon Carbide Reinforced Aluminum Composites", Scripta Metallurgica; 20 (1), pp.43-48 (1986).
7. Arsenault, R.J. and Taya, M., "Thermal Residual Stress in Metal Matrix Composite", Acta Metallurgica; 35 (3), pp.651-659 (1987).
8. Signorelli, R.A., "Metal Matrix Composites", Encyclopedia of Materials Science and Engineering; The MIT Press, Cambridge, 4 (J-N), pp.2949-2953 (1986).
9. Aeropropulsion '87, Session 1 - Aeropropulsion Materials Research, NASA Conf. Publ. 10003; November, p.77 (1987).
10. Lynch, C.T. and Kershaw, J.P., Metal Matrix Composites; CRC Press and the Chemical Rubber Co., Cleveland, Ohio, pp.1-53 (1972).

T-3957

11. Thornton, R.H., "Fabrication of Metal Matrix Composite Materials", Journal of Composite Materials; 2 (1), pp.32-42 (1968).
12. Alexander, J.A., "Five Ways to Fabricate Metal Matrix Composite Parts", Materials Engineering; July; pp.58-62 (1968).
13. Hong, S.J. and Kao, P.W., "Aluminum Composite Made by Resistance Sintering of Mechanically Alloyed Powders", Materials Science and Engineering; A119, pp.153-159 (1989).
14. Verma, S.K. and Dorcic, J.L., "Squeeze Casting for Metal-Ceramic Composites", SAE Technical Paper Series, International Congress and Exposition; Detroit, Michigan, February 23-27, pp. 1-12 (1987).
15. Cornie, J.A., Chiang, Y., Uhlmann, D.R., Mortensen, A., and Collins, J.M., "Processing of Metal and Ceramic Matrix Composites", Ceramic Bulletin; 65 (2), pp.293-304.
16. Otori, K., Watanabe, H., and Takeuchi, Y., "Silicon Carbide Whisker Reinforced composites - Fabrication and Properties", Materials Science and Technology; 3, January, pp. 57-60 (1987).
17. Milliere, C. and Suery, M., "Fabrication and Properties of Metal Matrix Composites Based on SiC Fibre Reinforced Aluminium Alloys", Materials Science and Technology; 4, January, pp.41-51 (1988).
18. Toth, I.J., Brentnall, W.D., and Menke, G.D., "Fabricating Aluminum Matrix Composites", Journal of Metals; September, pp.19-25 (1972).
19. Mortensen, A. and Cornie, J.A., "On the Infiltration of Metal Matrix Composites", Metallurgical Transactions A; 18A, June, pp.1160-1163 (1987).
20. Oh, S.-Y., Cornie, J.A., and Russell, K.C., "Wetting of Particulates with Liquid Aluminum Alloys: Part I. Experimental Techniques", Metallurgical Transactions A; 20A, March, pp.527-532 (1989).

T-3957

21. Aghajanian, M.K. and Claar, T.D., "Infiltration by Aluminum Alloy Melt for Manufacture of Metal Matrix Composites with the Use of a Barrier", European Patent Application; Application No.89630001.9, pp.1-12 (1989).
22. Aghajanian, M.K., Burke, J.T., White, D.R., and Nagelberg, A.S., "A New Infiltration Process for the Fabrication of Metal Matrix Composites", SAMPE Quarterly; July, pp.43-46 (1989).
23. Yang, J. and Chung, D.D. "Casting Particulate and Fibrous Metal Matrix Composites by Vacuum Infiltration of a Liquid Metal Under Inert Gas Pressure", Journal of Materials Science; 24, pp.3605-3612 (1989).
24. Stinton, D.P., Caputo, A.J., and Lowden, R.A., "Synthesis of Fiber-Reinforced SiC Composites by Chemical Vapor Infiltration", American Ceramic Society Bulletin; 65, (2), pp.347-350 (1986).
25. Maxwell, P.B., "The Infiltration Behavior of Aluminum into Silicon Carbide Compacts", MS Thesis, Colorado School of Mines, Thesis No.T-3396, April, 1987.
26. Seitz, J.D., "The Infiltration Kinetics of Silicon Carbide Reinforced Aluminum Matrix Composites", MS Thesis, Colorado School of Mines, Thesis No.T-3613, December, 1988.
27. Touloukian, Y.S., Kirby, R.K., Taylor, R.E., and Desai, P.D., Thermal Expansion - Metallic Elements and Alloys. Thermophysical Properties of Matter; 12, Plenum Publishing Corporation, New York, p.2 (1975).
28. Hatch, J.E., Aluminum: Properties and Physical Metallurgy; American Society for Metals, Metals Park, Ohio, pp.1-24 (1984).
29. Weast, R.C. CRC Handbook of Chemistry and Physics, CRC Press, 57th Edition, Cleveland, Ohio pp.F91-F131 (1976).
30. Reed-Hill, R.E., Physical Metallurgy Principles; second edition, D. Van Nostrand Co., New York, pp.569-570 (1973).

T-3957

31. Gebhardt, E., Becker, M. and Dorner, S., "The Properties of Metallic Melts: VIII The Density of Molten Aluminum and some Aluminum Alloys", *Zeitschrift fur Metallkunde*; 44, pp.573-575 (1953).
32. Coy, W.J. and Mateer, R.S., "Density of Molten Aluminum by Maximum Bubble Pressure Method", *ASM Transactions*; 58, pp.99-102 (1965).
33. Edwards, J.D. and Moormann, T.A., "Density of Aluminum from 20 to 1000°C", *Chemical and Metallurgical Engineering*; 24 (2), pp.61-64 (1921).
34. White, W.G., "Theory and Experiment in Methods for the Precision Measurement of Surface Tension", *Transactions of American Society for Metals*; 55, pp.757-777 (1962).
35. Mondolfo, L.F., Aluminum Alloys: Structure and Properties; Butterworths, Boston, (1976).
36. Pelzel, E., "Density Measurements for Elevated Temperatures - XI. The Specific Volume and the Expansion of Aluminum-Magnesium Alloys in Solid and Liquid States", *Zeitschrift fur Metallkunde*; 32, pp.7-9 (1940).
37. Laidler, K.J. and Meiser, J.H., Physical Chemistry; The Benjamin/Cummings Publishing Company, Inc., Menlo Park, California, pp.816-818 (1982).
38. Andrade, E.N.C., "A Theory of the Viscosity of Liquids - Part I", *Philosophical Magazine*; 17, pp.497-511 (1934).
39. Andrade, E.N.C., "A Theory of the Viscosity of Liquids - Part II", *Philosophical Magazine*; 17, pp.698-733 (1934).
40. Geiger, G.H. and Poirier, D.R., Transport Phenomena in Metallurgy; Addison-Wesley Publishing Company, Reading, Massachusetts, pp.13-22 (1980).
41. Arsent'ev, P.P. and Polyakova, K.I., "Viscosity of Molten Aluminum", *Izvestiia Akademii nauk SSSR; Met.*, (2), pp.65-70 (1977).

T-3957

42. Gebhardt, E. and Detering, K. "Über die Eigenschaften metallischer Schmelzen: XVI. Die innere Reibung eutektischer Aluminiumlegierungen", Zeitschrift für Metallkunde; 50, pp.379-385 (1959).
43. Arsenault, R.J. and Pande, C.S., "Interfaces in Metal Matrix Composites", Scripta Metallurgica; 18, pp.1131-1134 (1984).
44. Iseki, T., Kameda, T. and Maruyama, T., "Interfacial Reactions between SiC and Aluminium During Joining", Journal of Materials Science; 19, pp.1692-1698 (1984).
45. Chernyshova and Rebrov, A.V., "Interaction Kinetics of Boron Carbide and Silicon carbide with Liquid Aluminum", Journal of the Less Common Metals; 117, pp.203-207 (1986).
46. Banerji, A., Rohatgi, P.K., and Reif, W., "Role of Wettability in the Preparation of Metal Matrix Composites (a Review)", Metallwissenschaft Technik; 7, (38), pp.656-661 (1984).
47. Russell, K.C., Cornie, J.A., and Oh, S.-Y., "Particulate Wetting and Particle/Solid Interface Phenomena in Casting Metal Matrix Composites", Interfaces in Metal matrix Composites (Conference Proceedings); New Orleans, Louisiana, March 2-6, pp.61-91 (1986).
48. Rohatgi, P.K., Asthana, R., and Das, S., "Solidification, Structures, and Properties of Cast Metal-Ceramic Particle Composites", International Metals Reviews; 31 (3), p.115 (1986).
49. Delannay, F., Froyen, L., and Deruyttere, A. "The Wetting of Solids by Molten Metals and its Relation to the Preparation of Metal-Matrix Composites", Journal of Materials Science; 22, pp.1-16 (1987).
50. Laurent, V., Chatain, D., and Eustathopoulos, N., "Wettability of SiC by Aluminum and Al-Si Alloys", Journal of Materials Science; 22, (1), pp.244-250 (1986).

T-3957

51. Choh, T. and Oki, T., "Wettability of SiC to Aluminium and Aluminium Alloys", *Material Science and Technology*; 3 (5), pp.378-385 (1987).
52. Kohler, W., "Examination of the Bonding of Al₂O₃ - and SiC - Crystals with Aluminum and Aluminum Alloys", *Aluminium*; 51, pp.443-447 (1975).
53. Lanning, B.R. "A Method for Predicting the Wettability and Interfacial Bond Strengths at Metal/Ceramic Interfaces", PhD Thesis, Colorado School of Mines, Thesis No.T-3875, February, 1990.
54. Hausner, H.H., Kempton, H.R., and Johnson, P.K., Perspectives in Powder Metallurgy. Vibratory Compacting: Principles and Methods; Plenum Press, New York, 2, pp.1-298 (1967).
55. Beddow, J.K., Particulate Science and Technology; Chemical Publishing Co., New York, (1980).
56. Shaler, A.J., "Theoretical Aspects of the Infiltration of Powder Metallurgy Products", *International Journal of Powder Metallurgy*; 1, pp.3-14 (1965).
57. Brittin, W.E., "Liquid Rise in a Capillary Tube", *Journal of Applied Physics*; 17, pp.37-44 (1946).
58. Ligenza, J.R. and Bernstein, R.B., "The Rate of Rise of Liquids in Fine Capillaries", *Journal of the American Chemical Society*; 73, pp.4636-4638 (1951).
59. Semlak, K.A. and Rhines, F.N., "The Rate of Infiltration of Metals", *AIME Transactions*; 212, pp.325-331 (1958).